TÉCNICO LISBOA

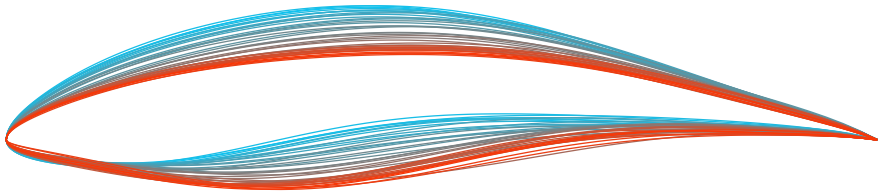

Design and Optimization of Hydrofoils Tailored for Marine Current Turbines

Francisco Mira Piteira Espenica

Thesis to obtain the Master of Science Degree in

Mechanical Engineering

Supervisors: Prof. Ricardo Balbino dos Santos Pereira
Dr. João Manuel Ribeiro Costa Baltazar

Examination Committee

Chairperson: Prof. Carlos Frederico Neves Bettencourt da Silva
Supervisor: Prof. Ricardo Balbino dos Santos Pereira
Member of the Committee: Prof. Luís Rego da Cunha Eça

November 2018

Dedicated to my parents
I owe everything to them, and a world more

Aos meus pais
Devo-lhes tudo o que sou

Acknowledgments

This work marks the end of my journey at Instituto Superior Técnico. These past five years have been challenging, as I knew they would be, and today I look back with pride and the knowledge that I have grown greatly as a person thanks to my time and experiences here. IST taught me more than Engineering.

I would like to thank my parents, first and foremost, as I owe everything I am to them and cannot express how much I love and value them. None of this would be possible without their encouragement and support. This work is dedicated to them as I close this chapter of my life and open another, with them by my side. Also, to my sister, for being the kind and loving person she is and always supporting me every step of the way.

To my supervisor, Ricardo Pereira, for being an example of not only what a great teacher but also a person is, and for the invaluable support and incredible availability given throughout the completion of this work. I wish him the best in all his endeavours, both musical and academic.

To João Baltazar, for his support with various aspects of this work and for his ingenious insight and input in this field.

To Professor José Falcão de Campos, for being the teacher who introduced me to the field of Fluid Mechanics, which came to be one of my favourite subjects along my degree and him one of the teachers I hold in my memory with the highest regard. I would like to thank him also for his input and the knowledge he shared for this work.

To my friends, Pedro Teixeira, Duarte Carrasquinho, Francisco Godinho and Gonçalo Saúde, for their advice, for accompanying me along this path, keeping me company, working alongside me and holding my spirits high, all the way to the end.

To my friend Gonçalo Sousa, who was a true companion throughout almost all challenges in our course, and for teaching me, by example, how to push myself harder and strive for excellency.

Lastly, and in all seriousness, I would like to thank musical artists from past and present, throughout all genres, from classical to hip-hop, from trip-hop to rock&roll, from Beethoven to Kendrick Lamar, from Pavarotti to Robert Plant, as they too accompanied me in this endeavour and inspired, and will continue to inspire me, in all objectives I pursue and challenges I face in the future.

The show must go on

Resumo

Este trabalho incide sobre o projecto e optimização de perfis para pás de turbinas marítimas.

Uma turbina de referência, com um rotor de 20 metros de diâmetro e integrando perfis da série NACA 63-8XX nas suas pás, é projectada para definição das condições de operação com recurso a uma rotina baseada na teoria da linha sustentadora. Um coeficiente de potência teórico de 0.483 é obtido, representando uma melhoria de 10% em comparação com cálculos de linha sustentadora de trabalhos anteriores.

A influência do factor N_{crit} no desempenho dos perfis é estudada, tendo-se considerado o valor 4 para simulação das condições de operação da turbina. Um método analítico é empregue para calcular a influência de escoamento não uniforme, variação de profundidade, desalinhamento com a corrente e ângulo cónico das pás.

Para o projecto dos perfis uma rotina de optimização por algoritmo genético já existente é utilizada. São criadas funções de custo com os objectivos de maximizar a razão de sustentação para resistência e o coeficiente de sustentação para os regimes de transição natural e forçada e maximizar a margem de cavitação para cada perfil e secção da pá.

Os perfis optimizados IST-MT1-XX demonstram melhorias até 73.21% e 99.82% em sustentação/resistência e coeficiente de sustentação, respectivamente, em relação aos perfis de referência com a mesma margem de cavitação. São obtidas também margens de cavitação até 3 relativamente ao número de cavitação local.

No final, a turbina de referência é redesenhada com os perfis IST-MT1-XX nas suas pás e testada com a mesma rotina de linha sustentadora. A nova turbina melhora o coeficiente de potência da turbina de referência em 0.33%, reduzindo a corda até 41%.

Palavras-chave: Perfil hidrodinâmico, turbina, multi-objectivo, cavitação, desempenho, optimização

Abstract

The design and optimization of hydrofoils tailored for marine current turbines is considered.

A reference turbine, with a rotor of 20 metres in diameter and blades integrating sections of series NACA 63-8XX, is designed for the definition of the operating conditions using a lifting line theory based routine. A theoretical power coefficient of 0.483 is achieved, yielding an improvement of 10% when compared to previous works in turbine lifting line predictions.

The influence of N_{crit} factor on hydrofoil performance and angle of attack is studied, resulting in the use of value 4 to mimic operating conditions of a marine turbine. An analytical methodology to calculate the influence of shear flow, change in depth, yaw misalignment and rotor pre-bend on angle of attack and effective velocity is implemented.

For the hydrofoil design, an already existing multi-objective optimization through genetic algorithm framework is used. Cost functions are developed with the objectives of maximizing lift to drag ratio and lift coefficient for natural and forced transition and maximizing cavitation margin for each hydrofoil and blade section.

Optimized hydrofoils IST-MT1-XX are obtained, yielding improvements in lift to drag ratio and lift coefficient for both regimes up to 73.21% and 99.82% respectively, for the same cavitation performance as reference hydrofoils, while also yielding cavitation margins of up to 3, relative to the local cavitation number.

Finally, the reference turbine is redesigned to incorporate the optimized hydrofoils and tested with the same lifting line routine, yielding an improvement of 0.33% in power coefficient for the same design conditions and reducing blade chord up to 41%.

Keywords: Hydrofoil, turbine, multi-objective, cavitation, performance, optimization

Contents

Acknowledgments v
Resumo vii
Abstract ix
List of Tables xv
List of Figures xvii
Nomenclature xxi
Glossary xxv

1 Introduction **1**
1.1 Renewable energy overview and motivation 1
1.2 Horizontal-axis current turbines 2
1.2.1 Operation in marine environment 3
1.2.2 High loading on structure 4
1.2.3 Extreme weather conditions, waves and fatigue 4
1.2.4 Seabed scour 4
1.2.5 Maintenance 5
1.2.6 Summary 5
1.3 Cavitation 6
1.4 HACT blade profiles - Hydrofoils 8
1.5 Thesis objectives 9
1.6 Thesis Outline 9

2 Background - Hydrofoil Design **11**
2.1 Two-dimensional blade section design 11
2.2 Blade Design 15

3 Reference Turbine **17**
3.1 Sections considered 17
3.2 $\mathbf{N_{crit}}$ factor influence on foil performance 18
3.3 Designed reference turbine 21
3.3.1 Design method - lifting line theory based routine 21
3.3.2 Reference turbine characteristics and performance 21

3.3.3 Reference turbine blades . . . 24
3.4 Operating curves . . . 24
3.4.1 Effective flow speed $\mathbf{V_{eff}}$ calculation . . . 24
3.4.2 Local inflow angle ϕ calculation . . . 27

4 Optimization Setup **29**
4.1 Optimization tool - *OptiFlow* . . . 29
4.1.1 Optimization framework . . . 29
4.1.2 Geometry parametrization . . . 30
4.1.3 Hydrodynamic performance analysis tool - RFOIL . . . 31
4.2 Experimental measurements and X/RFOIL calculations data comparison . . . 31
4.3 Simulation - Initial considerations . . . 33
4.4 Cavitation margin cost function - CF2 . . . 34
4.5 Cost function 1 - Hydrodynamic performance . . . 36
4.5.1 Version ZERO . . . 36
4.5.2 Version ONE . . . 37
4.5.3 Version TWO . . . 37
4.5.4 Version THREE . . . 39
4.5.5 Version FOUR . . . 41
4.5.6 Version FIVE . . . 43
4.6 Other simulations - Increased angle of attack variation . . . 45

5 Hydrofoil optimization results **49**
5.1 Section $\mathbf{r/R}$ = 20% , thickness $\mathbf{t/c}$ = 24% . . . 49
5.2 Section $\mathbf{r/R}$ = 30% , thickness $\mathbf{t/c}$ = 21% . . . 51
5.3 Section $\mathbf{r/R}$ = 45% , thickness $\mathbf{t/c}$ = 18% . . . 53
5.4 Section $\mathbf{r/R}$ = 75% , thickness $\mathbf{t/c}$ = 15% . . . 55
5.5 Section $\mathbf{r/R} \approx$ 100% , thickness $\mathbf{t/c}$ = 12% . . . 56
5.5.1 Optimization SEVEN C for section $\mathbf{r/R} \approx$ 100% , thickness $\mathbf{t/c}$ = 12% . . . 58
5.5.2 Optimization EIGHT C for section $\mathbf{r/R} \approx$ 100% , thickness $\mathbf{t/c}$ = 12% . . . 60

6 Selected hydrofoils, IST-MT1-XX **65**
6.1 IST-MT1-24 . . . 66
6.2 IST-MT1-21 . . . 66
6.3 IST-MT1-18 . . . 67
6.4 IST-MT1-15 . . . 68
6.5 IST-MT1-12 . . . 69
6.6 Redesigned turbine layout . . . 70

7 Redesign of horizontal axis turbine **73**
7.1 Redesigned turbine section data 73
7.2 Redesigned turbine characteristics and performance 73

8 Conclusions **77**
8.1 Reference turbine 77
8.2 Hydrofoil design 78
8.3 Redesigned turbine with selected IST-MT1-XX foils 79
8.4 Future Work 80

Bibliography **81**

A Reference Turbine **87**
A.1 NACA 63-8XX XFOIL data 87
A.2 Reference turbine geometry 89
A.3 Reference turbine operation characteristics 90
A.4 Reference turbine performance 91

B Redesigned turbine **93**
B.1 Optimized hydrofoils IST-MT1-XX XFOIL data 93
B.2 Bernstein coefficients of hydrofoils IST-MT1-XX 95
B.3 Redesigned turbine geometry 96
B.4 Redesigned turbine operation characteristics 97
B.5 Redesigned turbine performance 98

List of Tables

1.1 Brief data on largest HAMCTs currently industrialized, adapted fom: [4][7][8][9] 2
1.2 Brief summary on remedial actions to take on MCTs, adapted from [15] 5

2.1 The percentage of performance improvement. Source: [28] 13

3.1 N_{crit} values in real-life situations for reference. Source [38] 18
3.2 Turbine physical dimensions and flow characteristics 22
3.3 Reference turbine data 22
3.4 Blade section information 24
3.5 Comparison between analytical and computational values for V_{eff} 27

4.1 Comparison between experimental maximum C_L and minimum C_D measurements and X/RFOIL calculations at the same AOA 32
4.2 Cost function 1 history 36

6.1 Blade section information 70

7.1 Redesigned turbine data 75
7.2 Blade section information 76

B.1 Berstein coefficients for hydrofoil IST-MT1-12 95
B.2 Berstein coefficients for hydrofoil IST-MT1-15 95
B.3 Berstein coefficients for hydrofoil IST-MT1-18 95
B.4 Berstein coefficients for hydrofoil IST-MT1-21 95
B.5 Berstein coefficients for hydrofoil IST-MT1-24 95

List of Figures

1.1 Large industrialized HAMCTs mentioned in table 1.1. Sources, from left to right: first row, [10][8][11]; second row, [12][13][14] . . . 3
1.2 Support Structures for MCTs, adapted from [16] . . . 5
1.3 Cavitation observation on a model turbine in a cavitation tunnel, by Bahaj *et.al*. Source [19] 6
1.4 HAMCT scheme - Left-hand side, front view ; right-hand side, side view with shear (non-uniform) flow representation . . . 7
1.5 Two airfoil sections and respective boundary layer at angle of attack of 0° , Reynolds of $1{\cdot}10^7$ - XFOIL preview of C_p distribution along chord . . . 8
1.6 NACA 63-815 hydrofoil with respective boundary layer . . . 8

2.1 Profiles S1210 and HF-Sx shape comparison. Source: [25] . . . 12
2.2 Graphs comparing the performance of various tested hydrofoils for Re = $2.1{\cdot}10^6$. Source: [25] . . . 12
2.3 Parametric model of a hydrofoil and its defining parameters. Source: [29] . . . 13
2.4 Pareto front for the inverse of the average lift coefficient and the area-deviation criteria. Source: [29] . . . 14
2.5 Instances of the hydrofoil parametric model on the Pareto front depicted in figure 2.4 Decreasing lift coefficient in a left-to-right, top-to-bottom fashion. Source [29] . . . 14
2.6 Flexible hydrofoil composed of 6 elastic elements. Source [30] . . . 15
2.7 Corrected chord for non-cavitating conditions. Source: [34] . . . 15

3.1 NACA 63-815 foil, performance and cavitation bucket . . . 17
3.2 N_{crit} influence on L/D vs AOA for various Reynolds numbers . . . 19
3.3 N_{crit} influence on the transition location on the upper and lower foil surfaces for various Reynolds numbers . . . 20
3.4 Reference turbine blades' chord and pitch distribution . . . 23
3.5 Reference turbine blades' chord and pitch distribution . . . 23
3.6 Reference full scale turbine lifting line data, Bahaj curve fit to experimental data of model turbine [19] and lifting line predictions of Bahaj model turbine [45]. . . . 23
3.7 Blade section layout . . . 24
3.8 Operating curves of blade sections along the span - cavitation number vs AOA at section 25

3.9 Overview and blade section view 25
3.10 Comparison between analytical and computational values 26

4.1 Data comparison of lift and drag coefficient between XFOIL, RFOIL and experimental values from reference [53] - measurements for foil NACA 63-815 32
4.2 Pareto efficient points in last generation of simulation THREE C 34
4.3 Comparison of $-C_p$ distributions for various foils in the same Pareto front $-C_p$ distribution calculated for clean and rough regimes at the same AOA 35
4.4 Cavitation margin comparison between clean and rough regimes 35
4.5 Foils, Pareto front and L/D obtained with CF1 ONE C 37
4.6 Foils, Pareto front and L/D obtained with CF1 TWO and free (natural) transition 38
4.7 Foils, Pareto front and L/D obtained with CF1 TWO and forced transition 39
4.8 Foils, Pareto front and L/D obtained with CF1 THREE C 40
4.9 Version THREE C of CF1 - Comparison of free and forced transition regimes with various distributions 41
4.10 Foils, Pareto front and L/D obtained with CF1 FOUR C 42
4.11 Version FOUR C of CF1 - Comparison of free (natural) and forced transition regimes with various distributions 43
4.12 Foils, Pareto front and L/D obtained with CF1 FIVE C 44
4.13 Version FIVE C of CF1 - Comparison of free (natural) and forced transition regimes with various distributions 45
4.14 Foils, Pareto front and L/D obtained with CF1 SIX C 46
4.15 Version SIX C of CF1 - Comparison of free (natural) and forced transition regimes with various distributions 47

5.1 Foils, Pareto front and L/D obtained with CF1 FIVE C for hydrofoils of thickness t/c = 24% 50
5.2 Thickness of 24% - Comparison of free and forced transition regimes with various distributions 50
5.3 Thickness of 24% - Comparison with reference hydrofoils, thickness of 24% 51
5.4 Foils, Pareto front and L/D obtained with CF1 FIVE C for hydrofoils of thickness t/c = 21% 52
5.5 Thickness of 21% - Comparison of free and forced transition regimes with various distributions 52
5.6 Thickness of 21% - Comparison with reference hydrofoils 53
5.7 Foils, Pareto front and L/D obtained with CF1 FIVE C for hydrofoils of thickness t/c = 18% 53
5.8 Thickness of 18% - Comparison of free and forced transition regimes with various distributions 54
5.9 Thickness of 18% - Comparison with reference hydrofoils 54
5.10 Foils, Pareto front and L/D obtained with CF1 FIVE C for hydrofoils of thickness t/c = 15% 55
5.11 Thickness of 15% - Comparison of free and forced transition regimes with various distributions 56

5.12 Thickness of 15% - Comparison with reference hydrofoils 56
5.13 Foils, Pareto front and L/D obtained with CF1 FIVE C for hydrofoils of thickness t/c = 12% 57
5.14 Thickness of 12%, optimization FIVE C - Comparison of free and forced transition regimes with various distributions 57
5.15 Thickness of 12% - Comparison with reference hydrofoils 58
5.16 Foils, Pareto front and L/D obtained with CF1 SEVEN C for hydrofoils of thickness t/c = 12% 59
5.17 Thickness of 12%, optimization SEVEN C - Comparison of free and forced transition regimes with various distributions 59
5.18 Foils, Pareto front and L/D obtained with CF1 EIGHT C for hydrofoils of thickness t/c = 12% 60
5.19 Thickness of 12%, optimization EIGHT C - Comparison of free and forced transition regimes with various distributions 61
5.20 Thickness of 12% - Comparison of cavitation margin vs L/D performance for both regimes and all optimizations 62
5.21 Thickness of 12%, optimization EIGHT C - Comparison with reference hydrofoils 63

6.1 IST-MT1-24 - Geometry of the hydrofoil and related data 66
6.2 IST-MT1-21 - Geometry of the hydrofoil and related data 67
6.3 IST-MT1-18 - Geometry of the hydrofoil and related data 68
6.4 IST-MT1-15 - Geometry of the hydrofoil and related data 69
6.5 IST-MT1-12 - Geometry of the hydrofoil and related data 70
6.6 Chosen hydrofoils incorporating redesigned turbine blades 71

7.1 IST-MT-15 hydrofoil, performance and cavitation bucket - data obtained with XFOIL 73
7.2 Redesigned turbine blades' chord and pitch distribution 74
7.3 Power coefficient variation with TSR 74
7.4 Redesigned and reference turbine C_P vs TSR comparison 75
7.5 Blade section layout 76

A.1 Sections composing the blades of reference turbine (data retrieved from software XFOIL) 87
A.2 Sections composing the blades of reference turbine (data retrieved from software XFOIL) 88
A.3 Reference turbine blades chord distribution 89
A.4 Reference turbine blades pitch distribution 89
A.5 Reference turbine characteristics at TSR = 6 and U = 2 m/s 90
A.6 Reference turbine performance data at U = 2 m/s 91

B.1 Sections composing the blades of the redesigned turbine (data retrieved from software XFOIL) 93
B.2 Sections composing the blades of the redesigned turbine (data retrieved from software XFOIL) 94

B.3 Redesigned turbine blades chord distribution 96
B.4 Redesigned turbine blades pitch distribution 96
B.5 Redesigned turbine characteristics at TSR = 6 and U = 2 m/s 97
B.6 Redesigned turbine performance data at U = 2 m/s 98

Nomenclature

Greek symbols

α	Angle of attack - AOA	
β	Yaw misalignment angle	
λ_r	Local TSR (at section r)	$\lambda_r = \frac{\Omega \cdot r}{U}$
μ	Blade cone or pre-bend angle	
ν	Fluid kinematic viscosity	
Ω	Turbine rotational speed	
ϕ	Local inflow angle (at blade section)	
Ψ	Azimuthal blade rotation angle	
ρ	Fluid density	
σ	Cavitation number	$\sigma = \frac{p_\infty - p_v}{1/2 \cdot \rho {V_{eff}}^2}$
σ_i	Cavitation inception number	
Γ	Circulation	
θ	Blade pitch angle	

Roman symbols

A	Swept area	
a	Axial induction factor	
a'	Tangential induction factor	
c	Hydrofoil chord	
C_D	Drag coefficient	
C_L	Lift coefficient	
C_P	Power coefficient	$C_P = \frac{P}{1/2 \cdot \rho A U_0^3}$

C_p	Pressure coefficient	$C_p = \frac{p-p_\infty}{1/2 \cdot \rho {V_{eff}}^2}$
$C_{p_{min}}$	Minimum pressure coefficient	$C_{p_{min}} = \frac{p_{min}-p_\infty}{1/2 \cdot \rho {V_{eff}}^2}$
C_T	Thrust coefficient	$C_T = \frac{T}{1/2 \rho A U^2}$
D	Drag force	
d	Section depth to mean sea level	
d_0	Rotor hub depth	
D_T	Turbine rotor diameter	
g	Gravity acceleration	
h	Section height to sea bottom	
h_0	Rotor hub height to sea bottom	
K	Yaw misalignment factor	
L	Lift force	
P	Power	
p	Local pressure	
p_{atm}	Atmospheric pressure	
p_{dyn}	Dynamic pressure	$p_{dyn} = 1/2 \cdot \rho V^2$
p_{hyd}	Hydrostatic pressure	$p_{hyd} = \rho g d$
p_∞	Undisturbed flow pressure	$p_\infty = p_{hyd} + p_{atm}$
p_{min}	Local minimum pressure	
p_v	Vapor pressure	
R	Turbine rotor radius	
r	Blade section radius	
Re	Reynolds number	
r/R	Adimensionalized radial position of blade section	
T	Thrust force	
t	Hydrofoil thickness	
t/c	Adimensionalized hydrofoil thickness	
TSR	Tip speed ratio	$TSR = \frac{\Omega \cdot R}{U}$

U Undisturbed (free) flow speed

U_0 Undisturbed (free) flow speed at hub height - rated or design speed

U_r Flow speed at section (including induction)

$U_{r\perp}$ Axial component of U_r

$U_{r\top}$ Tangential component of U_r

U_{SH} Undisturbed (free) flow speed at a given section

V_{eff} Effective (local) flow speed

x Chord-wise position

x/c Adimensionalized chord-wise position

z_r Roughness length

Subscripts

0 Conditions refering to turbine hub

$clean$ Regarding clean regime (natural transition)

$forced$ Regarding forced transition regime

$free$ Regarding natural transition regime

i, j Computational indexes

∞ Undisturbed (free) flow condition

max Maximum value

opt Optimum value

$rough$ Regarding rough regime (forced transition)

Superscripts

ref Reference value

$weighted$ Weighted value

Glossary

AOA	Angle of Attack (α)
BEM	Blade element momentum, can also be blade element momentum theory, BEMT
CFD	Computational Fluid Mechanics
CF	Cost Function
CST	Class Shape Transform (parametrization method for airfoils)
HACT	Horizontal-Axis Current Turbine
HAMCT	Horizontal-Axis Marine Current Turbine
MCT	Marine Current Turbine
NSGA-II	Non-dominated Sorting Genetic Algorithm II - fast sorting and elite multi-objective genetic algorithm
$\mathbf{N_{crit}}$	Logarithm of the amplification factor of the most-amplified frequency which triggers transition in e^n method; user defined parameter in software XFOIL
OES	Ocean Energy Systems (organization)

Chapter 1

Introduction

In this chapter a general overview on renewable energies and motivation for research on hydro-kinetic energy is presented, followed by a brief literature review on horizontal-axis marine current turbines and their blades. The objective for this thesis is then defined, together with an outline for the following chapters.

1.1 Renewable energy overview and motivation

Worldwide energy consumption has been continuously growing year after year due to increasing global population and technological development. This increased consumption has been sustained throughout the years mainly by fossil-fuels and other non renewable sources, which are widely known as being non-sustainable in the long haul and harmful to the environment.

Large progress has been made in the fields of solar and wind energy production, making these the most developed renewable energy production sources available and viable today [1]. However, these sources are subject to monthly and even daily variations due to the weather, making their availability hard to predict and thus hard to extract their full potential. Because of this, it is impossible to exclusively depend on the energy produced from these sources. These variations are aggravated in the case of solar energy production since energy storage is not yet fully optimized, and furthermore, because its cost of installation is still high compared to other more conventional electric energy sources. [1].

Onshore wind as well as offshore wind energy production are mainly affected by weather variations as mentioned before, which are difficult to fully predict. This unpredictability and relative randomness makes this type of energy production unsuitable for sustaining the continuous base load energy demand currently provided by traditional fuel, carbon-based sources.

Due to these limitations and also with environmental and sustainability concerns in mind, research has been conducted in recent years in the area of ocean energy. Cumulative ocean energy capacity has doubled worldwide from less than 12 MW in 2016 to over 25 MW in 2017, according to the OES (Ocean Energy Systems) annual report [2].

Many types of energy can be extracted from the ocean, such as thermal, ocean osmosis (salinity

gradients), biomass, wave energy (power harnessed from wind driven waves) and hydro-kinetic energy (extraction of kinetic energy from current motion), being the last two the main focus of recent research [3]. Among these, hydro-kinetic energy and more specifically the extraction of kinetic energy from currents generated by tidal motion is more advantageous due to the high predictability of its source. Tides are influenced by the gravitational interaction of the Earth-Moon-Sun astronomic system and are mostly independent of weather conditions, making it possible to predict resource availability with decades' notice and very high accuracy [4]. This characteristic is unrivalled by any other renewable energy source.

There are two ways of harnessing tidal energy: building a tidal dam across a bay or estuary or through tidal turbines, extracting kinetic energy directly from the flow. It is estimated that the potential for tidal current energy extraction using available technologies is of 75 GW worldwide and 11 GW for Europe [4]. The main drawback of tidal dams is their environmental impact, changing the hydrology of the installation site and affecting its marine ecosystem [3]. Other advantages of current turbines vs. tidal dams are the easier system scalability and lower cost.

The horizontal-axis current turbine (HACT) appears to be the most technologically and economically viable current harnessing technology currently available [5][6], outperforming their vertical-axis counterparts when it comes to self-starting capability, torque fluctuations and overall efficiency [4].

1.2 Horizontal-axis current turbines

Hydro-kinetic horizontal-axis turbines are here referred to as horizontal-axis current turbines as their use is not limited to marine tidal currents. This type of turbines can also be employed in river beds or man made channels, with the appropriate modifications and limitations. However, emphasis is put on marine current as this is expected to be the main application for this type of turbines [6], and this work focuses on this application.

Marine current turbines can be broadly split into two categories: *perpendicular axis turbines* (axis is perpendicular to flow direction, horizontally or vertically) and *parallel axis turbines* (axis is parallel to flow direction). Table 1.1 shows present day industrialized horizontal axis marine current turbines (HAMCTs) and main technical characteristics.

Table 1.1: Brief data on largest HAMCTs currently industrialized, adapted fom: [4][7][8][9]

Company	DCNS, EDF	Atlantis Resources			Voith	Sabella	GE-Alstom
Device	OpenHydro	AR1000	AR1500	MCT Seagen S	Voith 1 MW	D10	Alstom 1 MW
Rated power [kW]	$2{\cdot}10^3$	$1{\cdot}10^3$	$1.5{\cdot}10^3$	$2{\cdot}10^3$	$1{\cdot}10^3$	$1.1{\cdot}10^3$	$1{\cdot}10^3$
Rated current speed [m/s]	4	2.65	3	2.4	2.9	4	2.7
Blade number per rotor	10	3	3	2	3	6	3
Rotor diameter [m]	16	18	18	20	16	10	18
Blade swept area [m^2]	181	254	254	314	194	78.5	254
Estimated $C_{P_{max}}$ value	0.34	0.41	-	0.45	0.41	0.43	0.39
Pitch-able blades	No	No	Yes	Yes	No	No	Yes
Design depth [m]	35-40	30	-	40	-	55	35-80

(a) OpenHydro (b) AR1000 (c) Seagen S

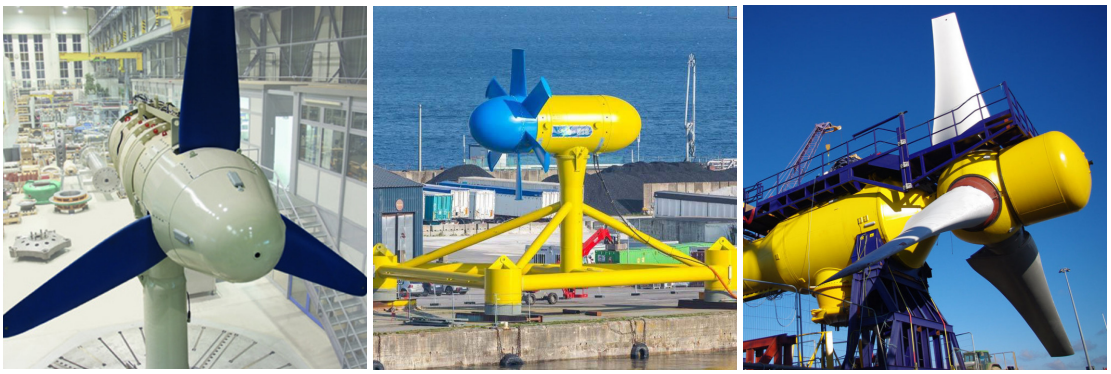

(d) Voith 1 MW (e) Sabella D10 (f) Alstom 1 MW

Figure 1.1: Large industrialized HAMCTs mentioned in table 1.1.
Sources, from left to right: first row, [10][8][11]; second row, [12][13][14]

Although there are many similarities between wind turbines and HAMCTs, the latter pose different problems and engineering challenges due to the harsh environment in which they operate.

A brief summary of the many technical problems and situations to consider when designing this type of machine is now made in a manner of reference for future developments.

1.2.1 Operation in marine environment

Marine environment is considerably harsher than low level atmospheric conditions in which wind turbines operate. Among other hazards, the following are identified as the most important:

- **Corrosion** - Since seawater is a saline solution, any metallic components have to be protected from the surrounding water. Blades have to be galvanized, painted or made from materials resistant to corrosion. Turbine nacelles have to be well sealed, as corrosion might give way to infiltrations into the turbine generator, leading to catastrophic failure. Another option is to build thicker components, in order to offset the material loss in operation. The roughness due to corrosion will probably exclude the use of uncoated steel in the turbine blades [7].

- **Debris impact** - Debris carried in the flow could damage the turbine, being the blades more susceptible to this hazard, due to their rotational speed and thinness relative to the other components.

- **Marine growth/fouling** - Seaweed and other organisms may become attached to the turbine

blades, as usually observed in ship hulls. It is harmful for human economic activities and severely affects the service life of marine structures [15]. On a marine turbine, fouling of the blades would increase drag, thus reducing overall performance. Research indicates that a higher level of fouling on the blades can reduce the efficiency up to 70% [15]. MCTs are not able to produce the estimated electricity over the envisioned lifetime if serious marine fouling occurs.

1.2.2 High loading on structure

Since the density of seawater is about 1000 times higher than air, an underwater turbine will be subject to very high axial thrust. Thrust is the force generated in the flow direction resulting from the energy extraction by the turbine, and its value is given by:

$$T = {}^1\!/_2\, C_T \rho A U^2 \tag{1.1}$$

where C_T is the thrust coefficient and U is the flow velocity. The structure as a whole must withstand this force in order not to fail.

1.2.3 Extreme weather conditions, waves and fatigue

On land, wind turbines are vulnerable to cyclones and extreme weather phenomena. In a marine environment, extreme sea conditions have to be studied to ensure the durability of MCTs. Not only the support structures are susceptible to degradation due to these events but also the blades and nacelle structure [16]. Although the underwater conditions are more calm and predictable than at the surface, if the turbine is installed at shallow depths, research indicates that the surface waves generated by extreme events negatively influence the rotor blades, resulting in significant variation of thrust and torque [15], which influence the sustainability and fatigue life of the components. Fatigue damage has to be taken into account when designing a turbine rotor. Designers suggest blades be designed to sustain $1{\cdot}10^8$ cycles over a 20 year service life [15].

Besides surface waves, surface gravity waves can be important. These waves are caused by a vertical perturbation on the surface of oceans in which the gravitational force responds by trying to re-establish equilibrium [17]. When the depth is greater than the wavelength, the wave can be assumed as a gravity wave. Noruzi *et.al* [17] proposes equations for the modelling of surface gravity waves and inlet velocity of a HAMCT having in consideration the depth of installation, which can greatly influence the MCT performance, as well as the fatigue life of the blades.

Extreme weather events could also drag and carry debris in the flow, as already mentioned in subsection 1.2.1.

1.2.4 Seabed scour

At the planning stage of marine projects, the impacts on the seabed due to device installation are part of required environmental studies. Besides the effect of the supporting structure and the passing flow on

the seabed, the presence of a MCT changes the flow pattern, accelerating the flow in its vicinity and can lead to local scour if there is not enough clearance between the rotor and seabed [16]. It is important to foresee this impact as seabed degradation can lead to structure instability.

There are four main types of support structures: gravity structure, mono-pile, tripod/piled jacket and floating structure (see figure 1.2).

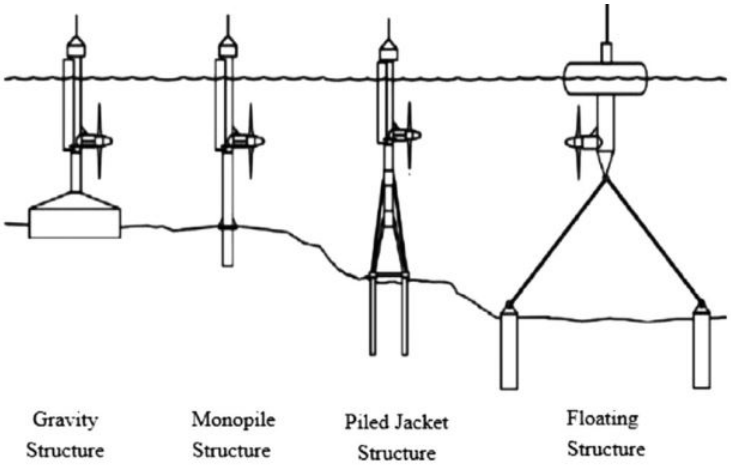

Figure 1.2: Support Structures for MCTs, adapted from [16]

The mono-pile has been applied on the Seagen S turbine (see figure 1.1(c)) [4], providing stability to the twin rotor assembly, as well as the capability of lifting the rotors from the sea water for maintenance. Sabella D10 (see figure 1.1(e)) employs tripod/piled jacket support.

The application of mono-pile structures is suggested from both a cost and structure stability point of view [15]. Chen *et al.* [16] propose equations (analytical method) with great potential to predict seabed scouring around a MCT, though further validation is still needed.

1.2.5 Maintenance

Maintenance and repair of MCTs require the use of ships. Additionally, if the turbine structure is not prepared to lift the rotor(s) above the surface (such a structure can be seen on the Seagen S turbine (see figure 1.1c)), maintenance may involve divers or specialized ships. Good quality sealants, lubricants, bearings and strong, well designed blades are needed in order to reduce the need for maintenance.

1.2.6 Summary

Table 1.2 shows a summary for this section.

Table 1.2: Brief summary on remedial actions to take on MCTs, adapted from [15]

Concerns	Time scale	Component at risk	Probability of failure	Remedial action
Corrosion/erosion	Long term	Blade, tower, nacelle	Medium	Composite material and painting
Marine fouling	Long term	Blade, nacelle	Medium	Fouling release painting
Extreme weather	Immediate	Blade, tower	High	Uninstall blades
Fatigue	Long term	Blade	Medium	Composite material
Seabed scour	Long term	Foundation, cable	Medium	Scour Protection

1.3 Cavitation

Cavitation occurs when the local pressure drops below the vaporization pressure of the surrounding fluid. When this happens, vapour bubbles form within the flow, which then, when pressure increases, can implode in a violent manner, damaging the surrounding components (see figure 1.3). Depending on the blade geometry, water quality and operating conditions, different types of cavitation (tip vortex, sheet, bubble, cloud, etc.) may develop individually or in any combination [18].

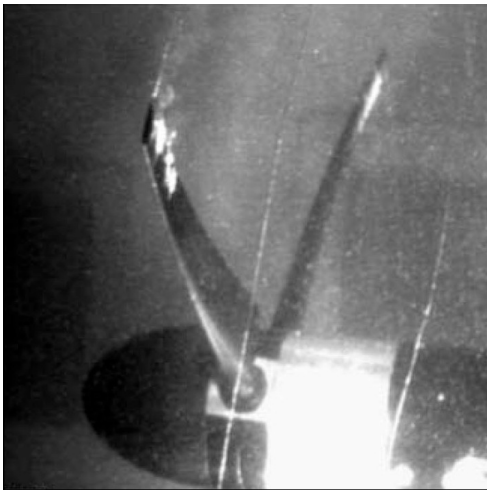

Figure 1.3: Cavitation observation on a model turbine in a cavitation tunnel, by Bahaj *et.al*. Source [19]

Depending on its extent and severity, cavitation can cause breakdown of turbine operation, blade surface erosion, noise and vibration [18]. In particular, cavitation erosion can damage the turbine blades by removing the protective coating and exposing the blade shell to aggressive marine environment, followed by gradual damage to the blade material. The probability of cavitation inception can be lowered by reducing the rotational speed of the turbine rotor, shortening the blades and placing the rotor deeper under water. However, these measures negatively affect the power production efficiency of the turbine. Thus, cavitation is a major factor to take into account in the choice of a marine current turbine's operational conditions [18].

Cavitation potential can be characterized through the cavitation number, a dimensionless coefficient which expresses the relationship between the difference of local pressure or undisturbed fluid pressure p_∞ from vapour pressure p_v and the dynamic pressure p_{dyn}:

$$\sigma = \frac{p_\infty - p_v}{1/2 \cdot \rho {V_{eff}}^2} \tag{1.2}$$

where V_{eff} is the local effective velocity, [20]; p_∞ is equal to $p_\infty = p_{hyd} + p_{atm}$, where p_{hyd} and p_{atm} are the hydrostatic or water column pressure and atmospheric pressure, respectively.

From equation 1.2 we can infer that the higher the value of σ, the less likely cavitation will occur. We can also observe that it is a function of pressure and fluid velocity. A high fluid velocity combined with a decreased pressure (p_∞) would decrease σ, precipitating the occurrence of cavitation. It follows that, in a steady uniform flow, the turbine blades are most susceptible to cavitation at their tips when

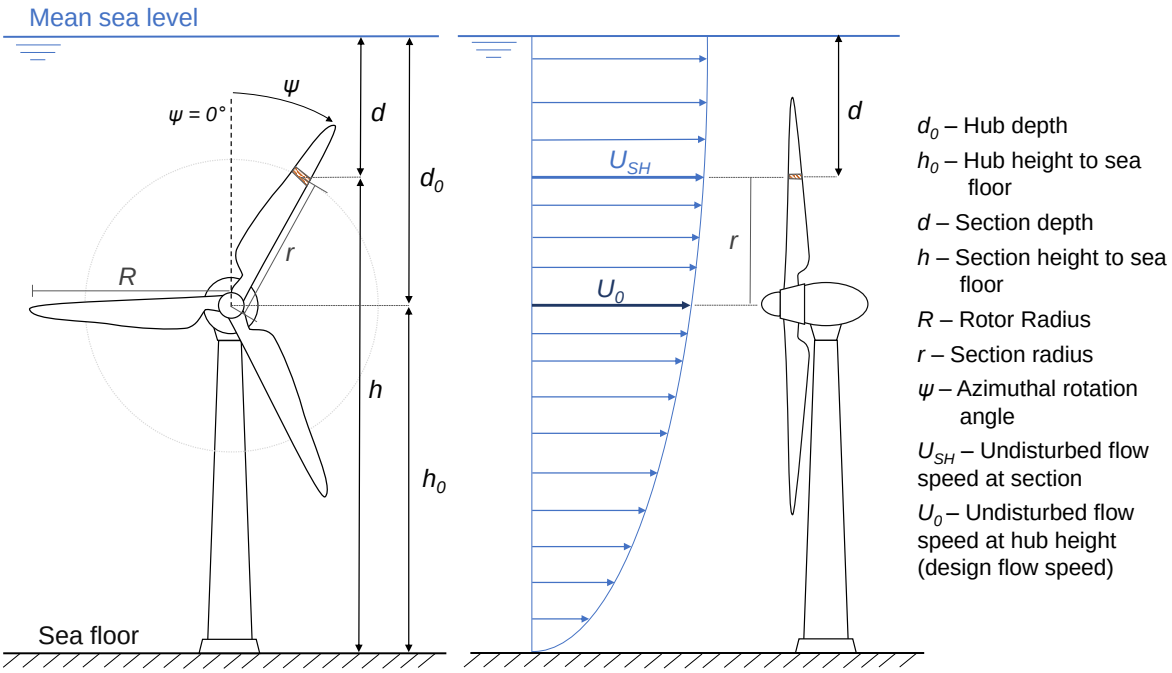

Figure 1.4: HAMCT scheme - Left-hand side, front view ;
right-hand side, side view with shear (non-uniform) flow representation

passing at the top of their revolution (azimuthal angle Ψ = 0°) - pointing upwards in vertical position (see the left-hand side of figure 1.4). This happens because it is at this point in the blade rotation that the hydrostatic pressure p_{hyd} reaches the lowest value (since $p_{hyd} = \rho g d$, where d is the section depth), and the effective velocity V_{eff} at the tip reaches its maximum, since $V_{eff} \approx \Omega \cdot R$, where Ω is the rotational speed of the rotor.

Cavitation inception is likely to occur when the cavitation number σ equals the minimum pressure coefficient, $C_{p_{min}}$, such that:

$$\sigma_i = -C_{p_{min}} \tag{1.3}$$

where σ_i is termed cavitation inception number, and where:

$$C_{p_{min}} = \frac{p_{min} - p_\infty}{{}^1/_2 \cdot \rho {V_{eff}}^2} \tag{1.4}$$

where p_{min} is the minimum pressure in the flow. The minimum pressure coefficient $C_{p_{min}}$ is intimately related with the foil section (see figure 1.5).

The cavitation inception number σ_i will vary along the blade span, depending on the effective local velocity V_{eff} and water column pressure p_{hyd}. Cavitation will occur for conditions where:

$$\sigma < \sigma_i \Leftrightarrow \sigma < -C_{p_{min}} \tag{1.5}$$

This subject will be discussed in detail throughout this work, so further considerations are left to a subsequent section.

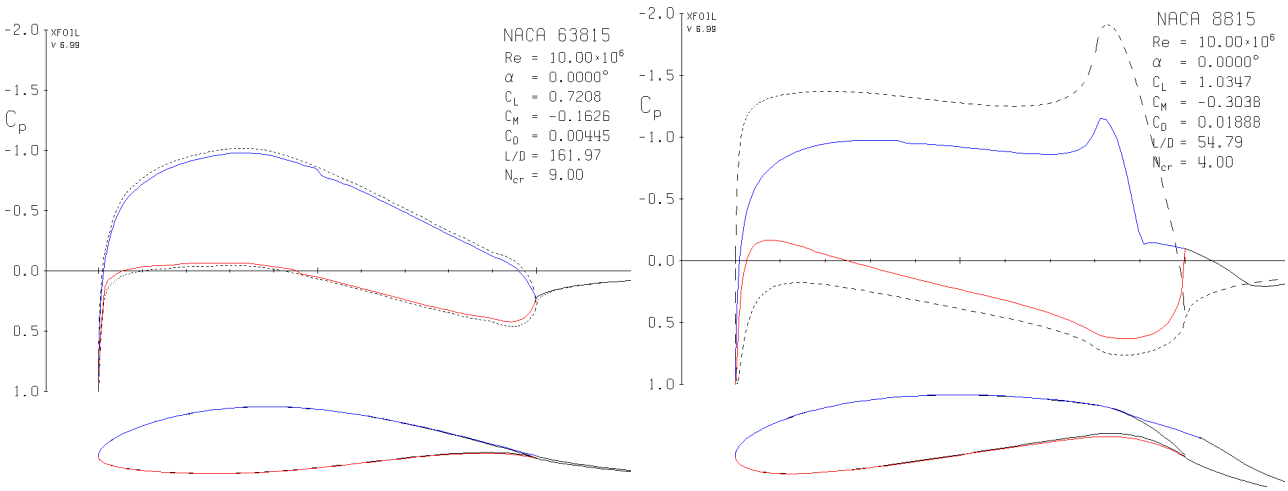

(a) NACA 63-815

(b) NACA 8815

Figure 1.5: Two airfoil sections and respective boundary layer at angle of attack of 0° , Reynolds of $1{\cdot}10^7$ - XFOIL preview of C_p distribution along chord

1.4 HACT blade profiles - Hydrofoils

One of the most important components that constitute a turbine are the rotor blades. These components generate lift and are responsible for the exchange of momentum between fluid and rotor. Each blade section has a geometry which corresponds to a hydrofoil, such as the one in figure 1.6.

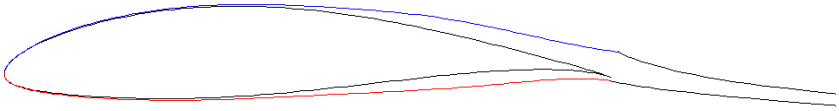

Figure 1.6: NACA 63-815 hydrofoil with respective boundary layer

The use of different hydrofoils as blade sections can make the power coefficient, C_P of a HACT vary significantly, even under the same operating conditions (pitch and inflow velocity) [5].

The power coefficient is defined as:

$$C_P = \frac{P}{1/2 \cdot \rho A U^3} \tag{1.6}$$

where P is power extracted by the machine.

Important hydrodynamic characteristics of hydrofoils include the pressure distribution on the hydrofoil surface; lift coefficient, C_L; drag coefficient, C_D and lift to drag ratio (L/D).

Additional blade parameters that need to be considered in the design stage are pitch and twist distribution of the blade and the performance characteristics during rotation. The design increases in complexity due to the non-uniformity of speed and direction of the flow, the shear profile of the tidal flow and the influence of water depth and free surface.

Perhaps the most important restriction is the avoidance of cavitation, which has to be tackled directly in the design stage of both hydrofoil and blades, and has to be achieved while maintaining high L/D

ratio, delaying separation and stall, over a wide range of angles of attack and flow conditions.

In order to have structural integrity and long operating life, blade sections must be thick, especially near the root region [21].

1.5 Thesis objectives

Taking the considerations of section 1.4 into account, this thesis seeks to:

- Design a full scale reference turbine, based upon a previous experimental model turbine [19], aiming to improve on its design and performance ;
- Develop a hydrofoil design procedure employing an already existing foil optimization framework [22]. Cost functions are developed towards the goal of improving the hydrodynamic performance of the hydrofoils while also decreasing the possibility of cavitation;
- Redesign the reference turbine with blades incorporating the obtained novel optimized hydrofoils and check for overall improved performance.

1.6 Thesis Outline

This thesis is organized into eight chapters: chapter 1 offers an overview on renewable energies and motivation for the present work, a brief background research on horizontal axis current turbines and finally the proposed objectives. Chapter 2 presents a short literature review, describing previous developments in hydrofoil and turbine blades design and optimization. Chapter 3 describes the definition of the reference turbine for which hydrofoils will be optimized (reference case). Chapter 4 presents the developed cost functions. Chapter 5 presents the obtained results, consisting of optimized hydrofoil geometries. Chapter 6 specifies the optimized hydrofoils chosen to integrate the redesigned turbine. Chapter 7 describes the novel rotor, as well as the analysis of its performance. Finally, Chapter 8 comprises conclusions and recommendations for future research.

Chapter 2

Background - Hydrofoil Design

This chapter aims to offer an overview of the latest developments and current techniques employed in the area of hydrofoil design and optimization. Also, since one of the objectives of the current work is to present a turbine composed of the newly designed hydrofoils, a brief review is provided on the most recent and relevant work on the design of marine current turbine rotors.

2.1 Two-dimensional blade section design

The earliest work found to be relevant to the present development is that of Ouyang *et.al* [23], in 2006. In this paper, a numerical procedure for the optimization of a two-dimensional hydrofoil is developed. The foil shape is parametrized by Bezier curves, and the optimization is performed using a genetic algorithm under three objective functions that translate into enhanced performance regarding lift and drag. This study uses Head's [24] entrainment integral method which solves a system of ordinary differential equations to obtain the momentum thickness, shape factor, and friction coefficient along the vane surface. The genetic algorithm departs from an initial pool composed of 100 profiles, and the maximum generation roof was 500.

Cost functions used by Ouyang *et.al* [23]:

$$CF_1(X) = \frac{C_L^2}{C_D} \tag{2.1a}$$

$$CF_2(X) = \frac{C_L}{C_D} \tag{2.1b}$$

$$CF_3(X) = C_L - 100 \cdot C_D \tag{2.1c}$$

In this work, for 0° angle of attack, final profiles were found to deliver high lift (≈ 0.6) and low drag (≈ 0.0055) coefficients, but cavitation performance was overlooked as an optimization objective. Another drawback to this work is that optimization was performed for 0° angle of attack only.

Although limited in many aspects, this is the earliest reference found that resembles the present work and as such is considered mention-worthy.

More recently in this field, in 2011, Goundar *et.al* [25] published work that, despite not being an optimization exercise, culminated in the presentation of a profile for the outer half span of a turbine blade that outperforms previous designs: the HF-Sx. This experimental profile is based on the standard S1210 with a 20% increase in camber and thickness (see figure 2.1).

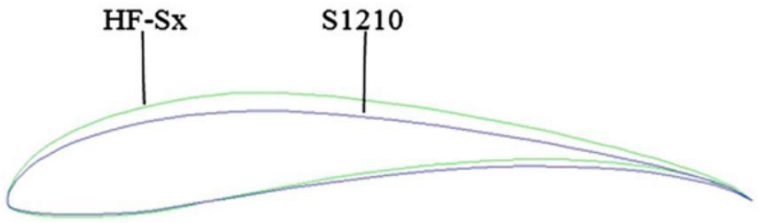

Figure 2.1: Profiles S1210 and HF-Sx shape comparison. Source: [25]

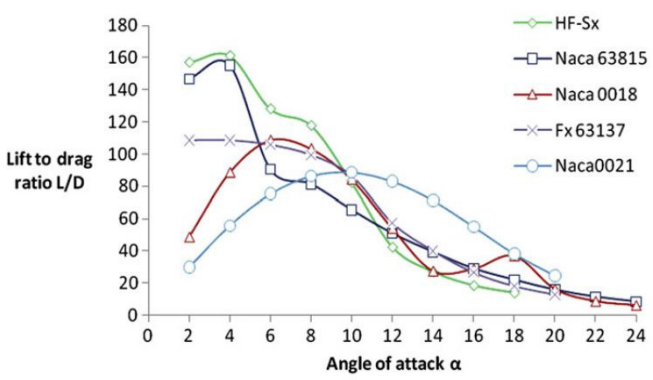

(a) Lift to drag ratio L/D performance comparison of tested profiles

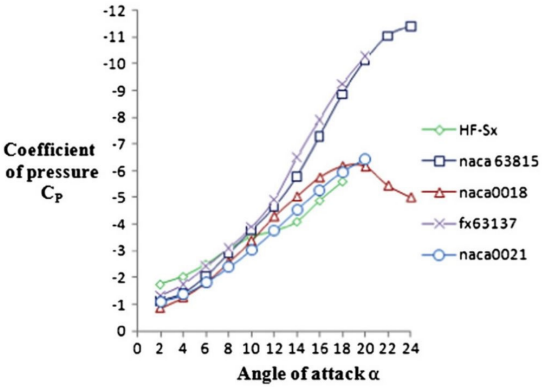

(b) Minimum pressure coefficient $C_{p_{min}}$ performance comparison of tested profiles

Figure 2.2: Graphs comparing the performance of various tested hydrofoils for Re = 2.1·10^6. Source: [25]

As it can be seen on figure 2.2a, the profile HF-Sx outperforms all other profiles for angles of attack between 2 and 10 degrees in terms of L/D. The data presented here was obtained through the use of software XFOIL at Reynolds number of 2.1·10^6 [25]. The optimized hydrofoil HF-Sx was then fabricated in the laboratory for 2-D scale testing. The Reynolds number of airflow in the wind-tunnel test section was matched with seawater flow velocity. XFOIL predictions for pressure distributions, C_L and C_D show good agreement with the experimental results obtained.

It is important to notice that this particular section shape (HF-Sx) outperforms the foil NACA 63-815. which was numerically and experimentally tested in previous work, by Bahaj *et.al* [19][26][27]. One can notice, particularly from figure 2.2a, that for most AOA, the ratio of L/D is superior. Also, from figure 2.2b, HF-Sx maintains a higher $C_{p_{min}}$ for higher AOA between 8 and 18° .

In this work it is also concluded that HF-Sx can be effectively used in a three-bladed, 10 m diameter rotor, from $r/R \approx 0.5$ to the tip to maximize rotor performance while avoiding cavitation at a design TSR of 4.3 [25].

In 2014, Xing-Qi *et.al* [28] published a paper in which a multipoint optimization method is proposed.

In this work the foil shapes are parametrized by Bezier curves and the optimization is carried out by the genetic algorithm NSGA-II. The hydrofoil's characteristics are obtained through computational fluid dynamics, CFD, simulation, more specifically, the finite volume method is used to solve the Navier-Stokes equations. The SST $k-\omega$ model is applied to close the Navier-Stokes equations.

The lift to drag ratio and cavitation performance are the objective functions, and the optimization effort focuses on enhancing the performance of the NACA 63-815 profile under three typical conditions. Finally, the optimized profiles are analysed in detail. This study results in three distinct profiles, all based on the NACA 63-815, called NACA 63-815GA, GB and GC.

Table 2.1: The percentage of performance improvement. Source: [28]

	Improvement of comprehensive performance	
	Lift to drag ratio performance	Cavitation performance
63-815GA	11.97 %	12.53 %
63-815GB	8.71 %	17.52 %
63-815GC	15.14 %	5.24 %

In table 2.1 we can observe the general results of this effort. These improvements are relative to the original foil at the same prescribed working condition. NACA 63-815GB was optimized in order to favour cavitation performance and GC the lift to drag ratio, while GA hangs in balance between these two. In general, improvements of more than 10% were obtained.

More recently, in 2017, Kostas *et.al* [29] published a paper on 2D section shape optimization using a geometric parametric modeller for the hydrofoil (see figure 2.3), an iso-geometric boundary element method (BEM) solver for potential flow and the NSGA-II genetic algorithm for optimization.

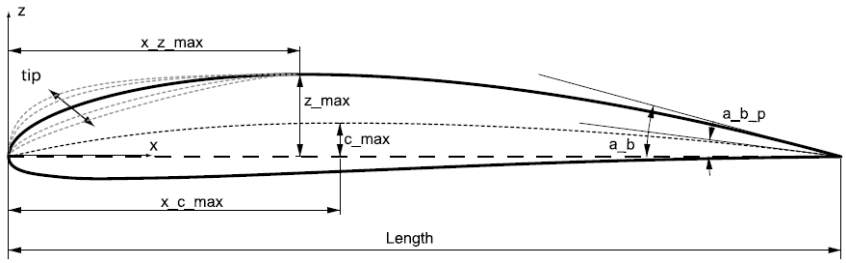

Figure 2.3: Parametric model of a hydrofoil and its defining parameters. Source: [29]

Multi-objective shape optimization is carried out and the method is successful in maximizing lift coefficient while maintaining a minimum deviation of the hydrofoil area from a reference section area (see figures 2.4 and 2.5).

It must be noticed that no mention was made to cavitation in this work, which has already been pointed out as one of the major concerns regarding hydrofoils.

In 2018, Sacher *et.al* [30] published an investigation on the use of constrained surrogate models

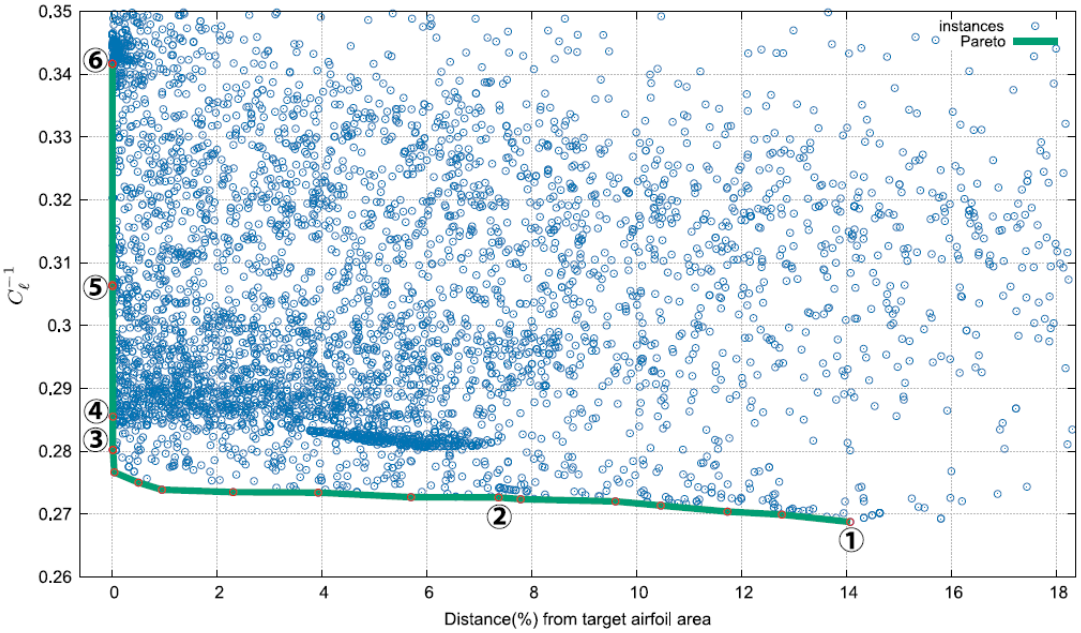

Figure 2.4: Pareto front for the inverse of the average lift coefficient and the area-deviation criteria. Source: [29]

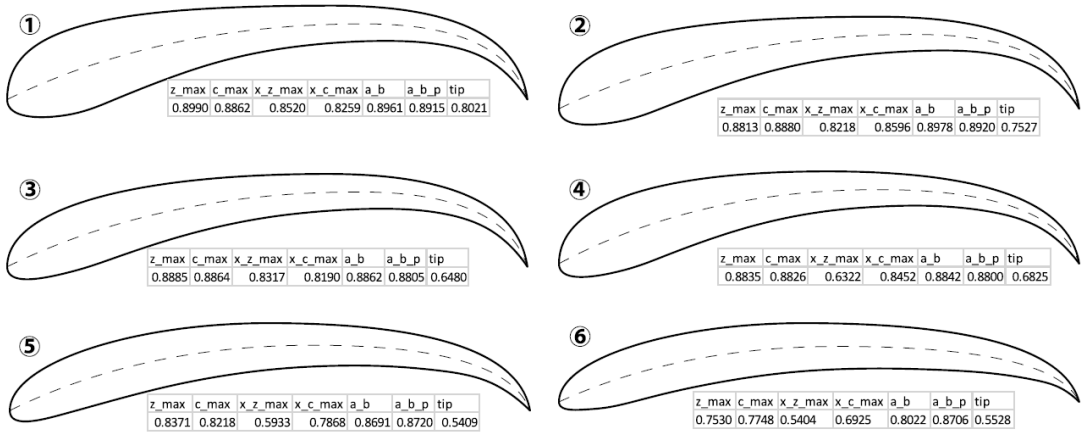

Figure 2.5: Instances of the hydrofoil parametric model on the Pareto front depicted in figure 2.4 Decreasing lift coefficient in a left-to-right, top-to-bottom fashion. Source [29]

to solve the multi-design optimization problem of a hydrofoil with a flexible trailing edge, being this the latest work found on hydrofoil optimization. Although not directed to marine current turbines, this work renders interesting results regarding cavitation and the method followed sets it apart from the remaining literature.

The surrogate-based optimization (EGO) substitutes the objective function of the problem by a model constructed from a limited number of computations at selected design points. This procedure is applied to the design of the shape and the elastic characteristics of a hydrofoil equipped with deformable elements providing flexibility to the trailing edge.

The optimization concerned the minimization of the hydrofoil drag while ensuring a non-cavitating flow, at selected sailing conditions (boat speed and lifting force). The drag value and cavitation criterion are determined by solving a two-dimensional non-linear fluid-structure interaction problem, based on a

Figure 2.6: Flexible hydrofoil composed of 6 elastic elements. Source [30]

static vortex lattice method with viscous boundary layer equations, for the flow, and a non-linear elasticity solver for the deformations of the elastic components of the foil. It was found that the flexible hydrofoil performs better over the same set of conditions that the rigid hydrofoil was optimized for: the flexible hydrofoil was found to have drag forces lower than that of the rigid on the whole range of boat speeds, except around 20 knots (37.04 km/h) where the two cases have the same drag force. The improvement in the drag force brought by the flexibility is particularly noticeable for the highest boat speeds $\geq$ 35 knots (64.82 km/h) and around 25 knots (46.3 km/h).

2.2 Blade Design

The first work considered belongs to Wu *et.al* [31], dating from 2013. In this paper a new method for horizontal-axis turbine blade design named Schmitz design is introduced. This new procedure, having the same philosophy as the Glauert theory, is simpler than the latter, not having an iterative routine for obtaining the axial and tangential induced velocity coefficients (a and a', respectively).

The method proves successful in the design, having a good consideration of the startup torque and taking into account cavitation, stall and separation. When contrasting with experimental data, [32] and [33], the method proves successful, yielding a decrease in the calculated thrust coefficient while keeping the power coefficient at the same level.

The second work considered is by Silva *et.al* [34]. In this paper, a mathematical approach for the design of hydro-kinetic blades which figures a cavitation prevention methodology is employed.

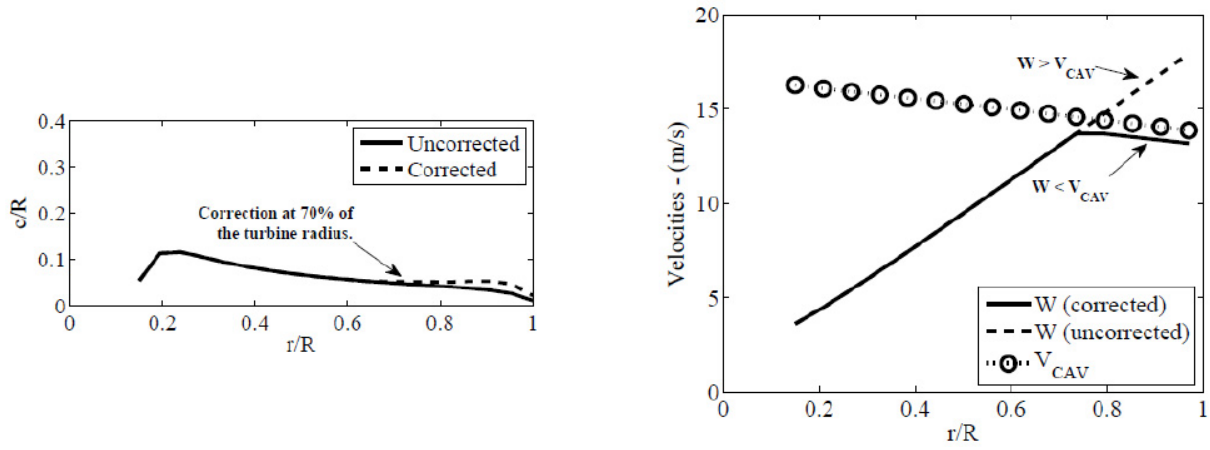

Figure 2.7: Corrected chord for non-cavitating conditions. Source: [34]

The proposed model extends on the classical Glauert's optimization method. A correction of the thrust coefficient is performed in which the minimum pressure coefficient is used as a limit in order to

avoid the blade cavitation. In the calculation of the optimum shape of the hydro-kinetic blade, the chord and twist angle are corrected.

The cavitation criterion presented consists on ensuring that the relative flow velocity W at a given section is smaller than a critical velocity, V_{cav}. This critical velocity is based on the minimum pressure coefficient at the section and is the limit flow velocity that triggers cavitation. When the relative flow velocity is greater than V_{cav}, ie. $W \geq V_{cav}$, a correction is made to the blade chord (see figure 2.7). The results are compared with the Glauert's optimization model showing good performance. The model described in this work is an approach which may be used in the design of hydro-kinetic turbine blades, which corrects the shape of the blade, aiming to prevent the cavitation.

The latest work considered is by Garg *et.al* [35], published in 2017. A hydro-structural design optimization approach that can handle large numbers of design variables, multiple design points, as well as design constraints on cavitation, maximum von Mises stress and manufacturing tolerances was developed. The hydro-structural solver couples a 3D nearly incompressible Reynolds-averaged Navier–Stokes solver with a 3D structural finite-element solver.

The approach was demonstrated and validated on a cantilevered aluminum NACA 0009 tapered hydrofoil with no sweep at Re = $1.0 \cdot 10^6$. The coupled hydro-structural solver was validated against experimental measurements for in-air natural frequencies, hydrodynamic load coefficients, and tip bending deformations. Good agreement was achieved between the numerical predictions and the experimental measurements: the average difference in the C_L predictions was 3.5%, the average difference in C_D predictions was 5.4%, the average difference in tip bending deflection was 5.5%, and the difference in the first in-air natural frequency was 1.6%.

A single-point hydro-structural optimization of the NACA0009 baseline hydrofoil yields a 12.4% increase in lift-to-drag ratio, a 2.5% reduction in mass, and a 45% increase in the cavitation inception speed. However, the performance of the single-point optimized hydrofoil is found to be worse than the baseline at off-design conditions. On the other hand, a multipoint optimization yields improved performance over the entire range of expected operating conditions with a weighted average increase in lift-to-drag ratio of 8.5%, and an increased cavitation inception speed of 38%. The computational time for the multipoint hydro-structural optimizations was roughly 50 hours using 192 processors, being possible to perform such optimizations overnight using 1000 processors [35].

Chapter 3

Reference Turbine

This chapter is dedicated to the turbine considered as reference for the subsequent hydrofoil optimization. The definition of a reference turbine is needed to characterize the operating conditions to which the blade sections are be subjected to, namely, Reynolds number, effective inflow speed, V_{eff}, and cavitation number, σ.

3.1 Sections considered

The reference turbine is designed based on work published by Bahaj *et.al* [19], as this is by far the most cited paper in the field of current turbines and the first known work to produce model experimental data.

The Bahaj turbine is composed of sections NACA 63-824, 63-821, 63-818, 63-815 and 63-812, from root to tip, respectively. These sections are studied in terms of aerodynamic performance L/D and cavitation performance with the widely used subsonic airfoil analysis software XFOIL [36]. The results can be seen in figure 3.1 for NACA 63-815, present at r/R = 0.75.

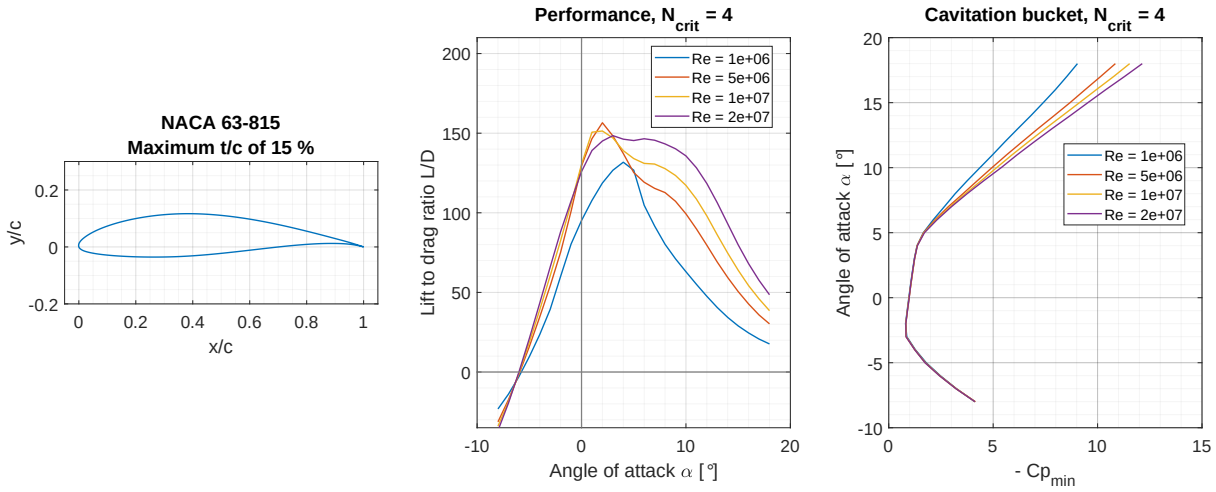

Figure 3.1: NACA 63-815 foil, performance and cavitation bucket

Results for the remaining airfoils that compose the reference turbines' blades may be seen in appendix A.1.

3.2 $\mathbf{N_{crit}}$ factor influence on foil performance

The N_{crit} factor is studied regarding its influence on foil performance for various relevant Reynolds numbers.

The N_{crit} factor is the exponent in what is called the e^n method, which has been widely used since its introduction in 1956 by Smith *et.al* [37]. It was the first method to directly model the growth of Tollmien-Schlichting waves in the boundary layer, which was shown by Schubauer *et.al* to be the precursor to transition in a low-turbulence environment [37]. Implemented in XFOIL, the user-specified parameter N_{crit} is the logarithm of the amplification factor of the most-amplified frequency which triggers transition. The value of this parameter depends on the ambient disturbance level in which the foil operates, and mimics the effect of such disturbances on transition [38].

It is relevant to study this influence due to the operating environment of the foils in the present work, which are, in principle, subject to large free stream turbulence and inflow disturbances.

The NACA 63-815 section and Reynolds number of $1{\cdot}10^6$, $5{\cdot}10^6$, $1{\cdot}10^7$ and $2{\cdot}10^7$ are considered.

The value of 9 corresponds to the standard value for N_{crit} [38], emulating the conditions in an average wind tunnel. N_{crit} = 1 corresponds to a situation in which flow disturbances are very large, precipitating transition almost instantly. N_{crit} = 4 is an intermediate value between 1 and 9, closer to the large disturbances of N_{crit} = 1. Table 3.1 shows a summary of real scenarios to offer a better grasp on this value's influence.

Table 3.1: N_{crit} values in real-life situations for reference. Source [38]

Situation	N_{crit} value
Sailplane	12 - 14
Motorglider	11 - 13
Clean wind tunnel	10 - 12
Average wind tunnel	9
Dirty wind tunnel	4 - 8

As can be observed from figure 3.2, there is a significant loss of performance as factor N_{crit} is reduced from 9 to 1, as well as a change in the optimum angle of attack (to which corresponds the maximum value of L/D). In figure 3.3, it can be noticed that, as expected, transition occurs earlier for all angles of attack as N_{crit} decreases.

Given the environment in which marine turbines operate and the possibility that fouling occurs on the blades, roughening their surface and thus promoting earlier transition, N_{crit} = 1 is plausible for the current study. However, such a loss in performance is considered too dramatic and (hopefully) unrealistic. As such, N_{crit} = 4 is considered an appropriate value for "mimicking" the operating conditions. From this point on, all data relative to foil performance takes this parameter value into account.

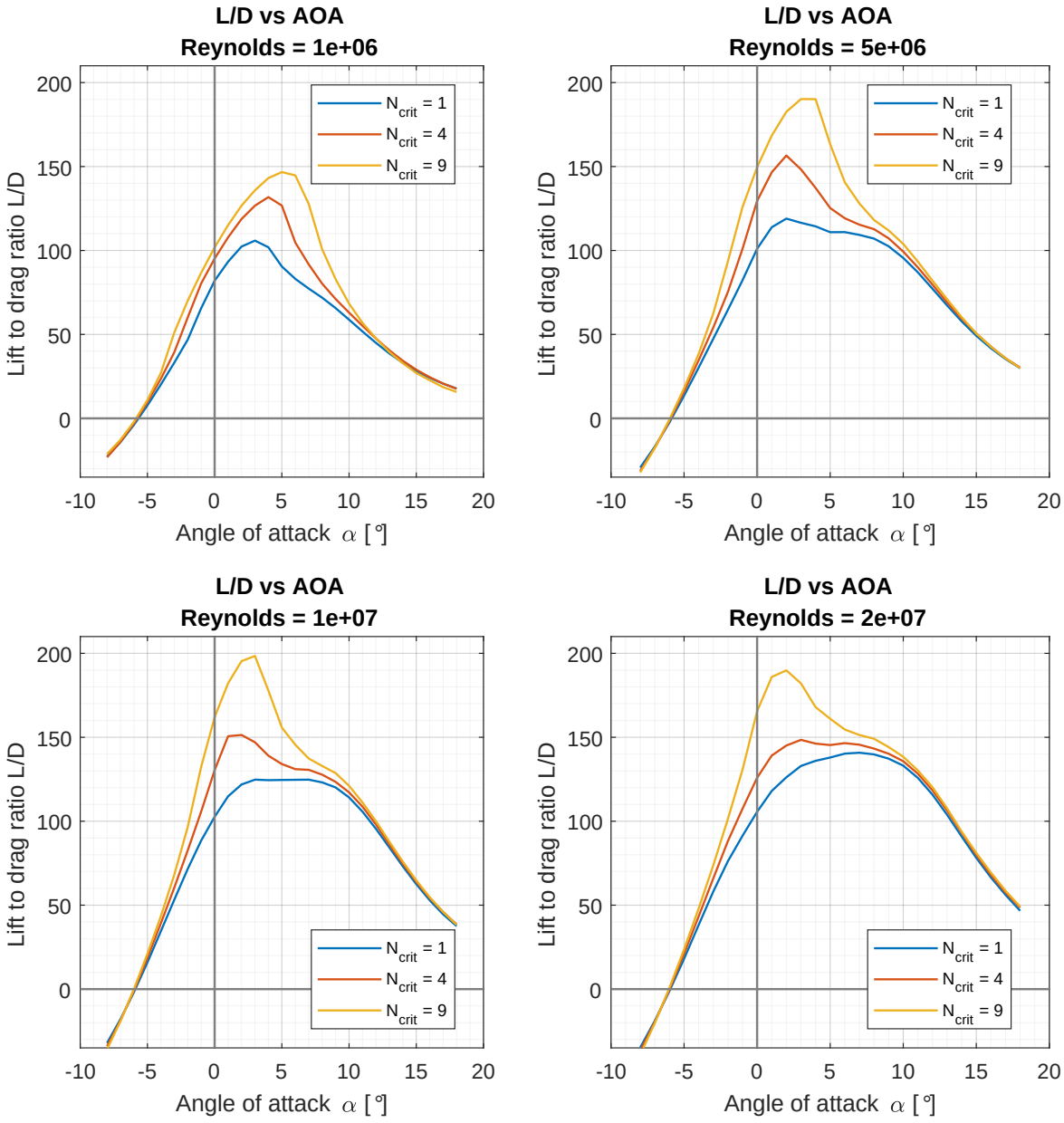

Figure 3.2: N_{crit} influence on L/D vs AOA for various Reynolds numbers

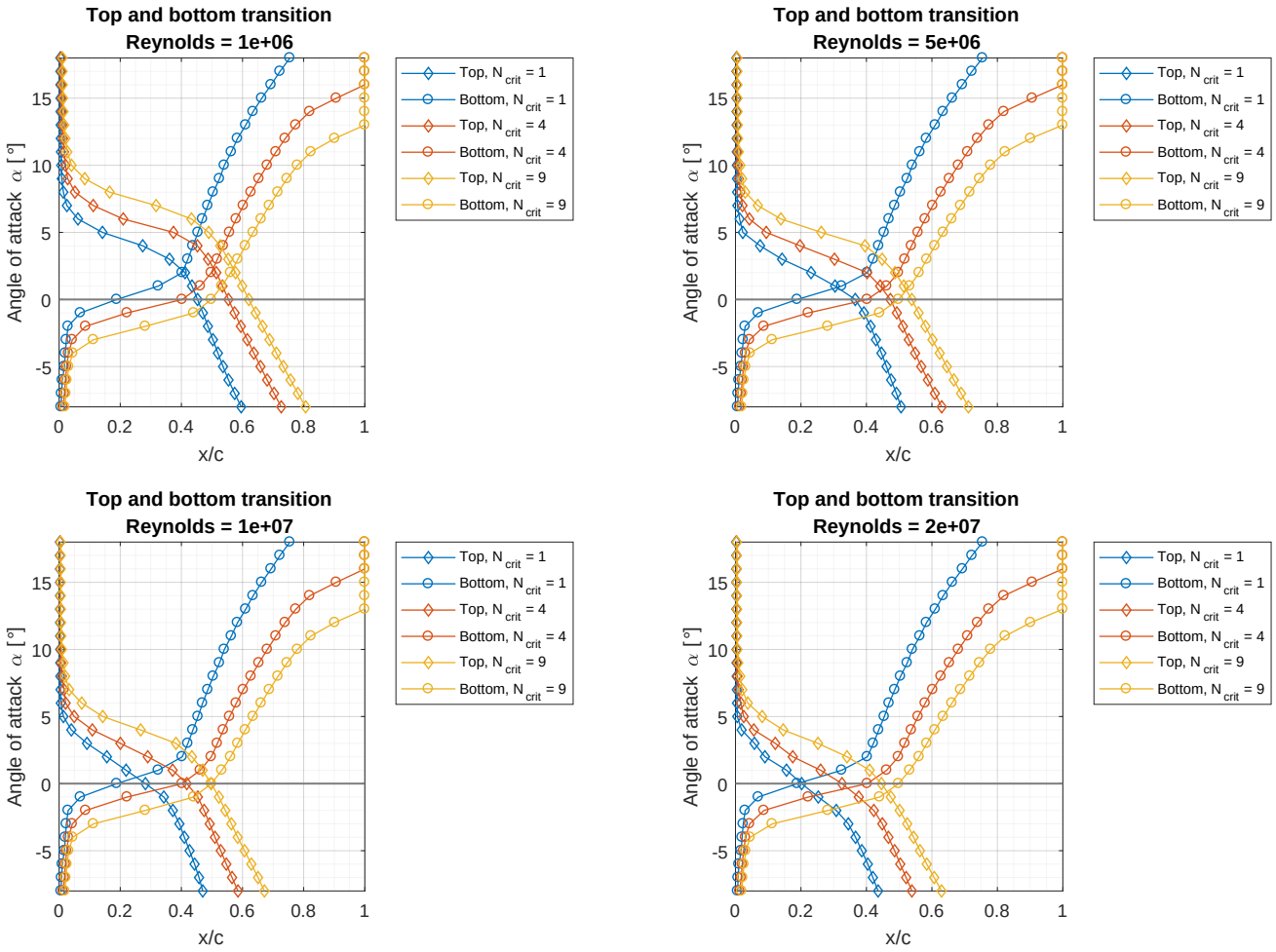

Figure 3.3: N_{crit} influence on the transition location on the upper and lower foil surfaces for various Reynolds numbers

3.3 Designed reference turbine

Taking the data mentioned in section 3.1 into account, a reference turbine is designed using a computer routine based on lifting line theory, developed at Instituto Superior Técnico, in Lisbon, Portugal [20] [39].

3.3.1 Design method - lifting line theory based routine

The problem of finding the conditions under which a horizontal-axis turbine extracts the maximum power from a fluid stream is of major importance both in the wind and marine current fields. For rotors with blades of high aspect ratio, the lifting line theory offers a suitable model for the lifting action of the blades which inherently takes into account the finite number of blades. This theory was originally introduced by Prandtl *et.al* for wings and later adapted to propellers in the classical works of Betz, in 1919 [40] and Goldstein, in 1929 [41]. For marine propellers the lifting line model evolved to a well-established tool for the hydrodynamic design of these systems. Among others, this was due to the work of Lerbs in 1952 [42]. The method used for the present work applies the optimization of Betz to a horizontal-axis turbine modeled by lifting line theory. The calculation of the induced velocities due to a helicoidal vortex is based on the analytical expressions of the induction factor method (Lerbs, 1952 [42], Wrench *et.al*, 1965 [43]). The vortex lattice method (Kerwin *et.al*, 1986 [44]) is used for the numerical calculation of the principal value integral at the lifting line. The method is applicable both to wind or marine turbines. For additional information see [20] and [39].

For the different radial sections r/R the values of optimum L/D are defined. From this specification, the optimum angle of attack and lift coefficient C_L for each section are selected as input design variables. Using the classical optimization criterion of constant induced hydrodynamic pitch distribution, the optimum circulation distribution is calculated for a specified tip speed ratio TSR and a prescribed thrust coefficient C_T, for which the corresponding optimal value of power coefficient C_P is calculated. The blade pitch and chord distributions follow from the hydrodynamic pitch and circulation distributions with the selected design angle of attack and lift coefficient and they are the design output variables.

3.3.2 Reference turbine characteristics and performance

The reference turbine is designed using a routine based on lifting line theory, as already mentioned. Table 3.2 presents both turbine and fluid flow physical data variables used as input for the lifting line routine. Table 3.3 presents the chord, thickness, pitch and Reynolds number radial distributions at the design conditions of the reference turbine along the blade span. Figures 3.4a and 3.4b represent the reference turbine blades' chord and pitch distribution, respectively. Figures 3.5a and 3.5b show the turbines' power coefficient variation with TSR and power curve, respectively. Further data on the reference turbine characteristics and performance can be viewed in appendixes A.3 and A.4, respectively.

In figure 3.6, lifting line predictions of the reference turbine C_P vs TSR distribution are shown. On the same figure, lifting line predictions of the Bahaj model turbine [45] and a curve fit to experimental data of the Bahaj model turbine [19] are shown. The lifting line routine analysis of the model turbine

Table 3.2: Turbine physical dimensions and flow characteristics

Variable	Symbol		Value
Hub height to sea floor	h_0	m	15
Hub depth to mean sea level	d_0	m	15
Diameter	D_T	m	20
Number of blades	-	-	3
Fluid density	ρ	kg/m^3	1025
Fluid vapour pressure	p_v	Pa	1670
Fluid kinematic viscosity	ν	m^2/s	$1.18{\cdot}10^{-6}$
Rated flow speed	U_0	m/s	2
Design tip speed ratio	TSR	-	6

Table 3.3: Reference turbine data

Span r/R [%]	Chord c/R [%]	Thickness t/c [%]	Pitch θ [$^\circ$]	Reynolds Re [-]
20	15.0	24.0	24.4	3.9e+06
25	14.8	22.5	23.4	4e+06
30	14.4	21.0	21.6	4.1e+06
31	13.9	20.7	19.4	4.3e+06
35	13.3	19.5	17.2	4.5e+06
40	12.6	18.7	15.1	4.8e+06
44	11.9	18.1	13.2	5.1e+06
45	11.1	18.0	11.6	5.3e+06
50	10.2	17.6	10.2	5.5e+06
55	9.3	17.1	8.9	5.6e+06
60	8.4	16.6	7.8	5.6e+06
65	7.7	16.1	6.9	5.5e+06
70	7.0	15.6	6.2	5.5e+06
74	6.5	15.1	5.7	5.4e+06
75	5.9	15.0	5.4	5.3e+06
80	5.2	14.6	5.2	4.9e+06
85	4.4	14.1	5.1	4.2e+06
90	3.3	13.6	5.0	3.3e+06
93	2.1	13.1	4.9	2.1e+06
100	0.7	12.0	4.9	7.2e+05

predicts a lower maximum C_P of 0.4393 (3.68% lower), which is predicted for a higher TSR of 7, than is obtained through experimentation, which measures a maximum C_P of 0.4555 at a TSR of 6. Through comparison of the orange and yellow lines on figure 3.6, it is possible to observe the differences obtained between experiments and what lifting line theory predicts for the same model turbine design.

It can also be observed that the lifting line routine predicts a higher C_P of 0.4833 for the full scale reference turbine than for the Bahaj model turbine (C_P is higher by 10%), at the same TSR. This is most likely due to scale effects. On a full scale turbine the Reynolds number is higher, which is favourable in terms of L/D on the blades (usually, at higher Re, foils exhibit higher L/D ratio). Thus, comparing between the yellow and blue curves in figure 3.6, scale effects can be appreciated.

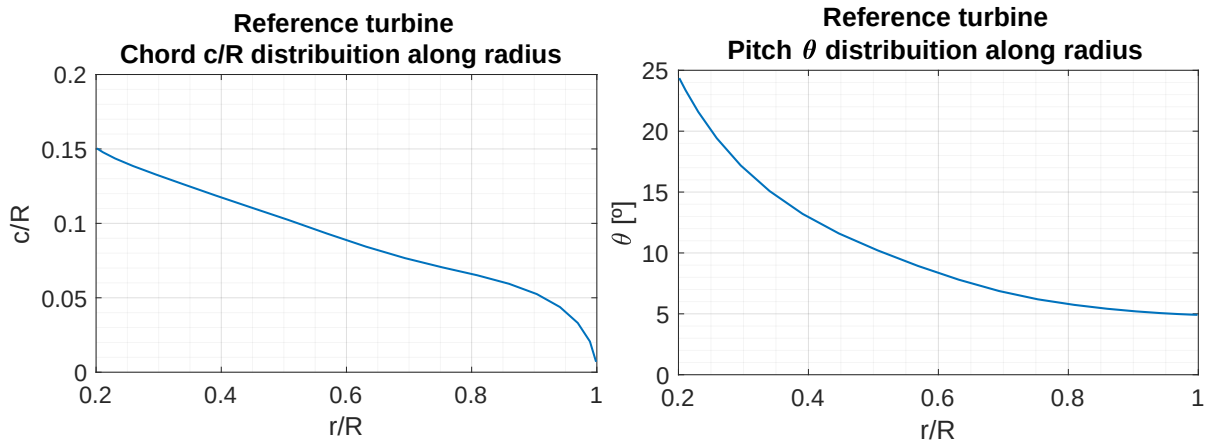

(a) Chord distribution

(b) Pitch distribution

Figure 3.4: Reference turbine blades' chord and pitch distribution

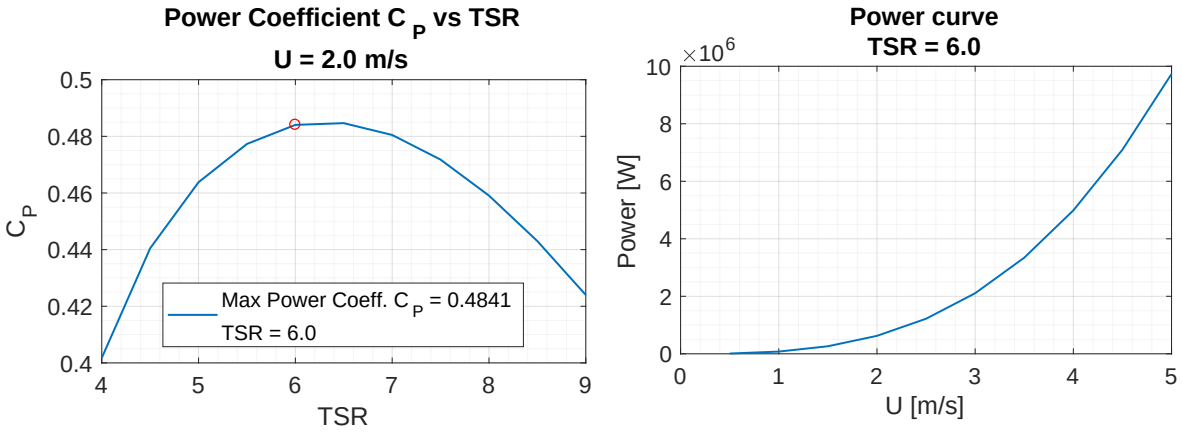

(a) Power coefficient variation with TSR

(b) Power curve

Figure 3.5: Reference turbine blades' chord and pitch distribution

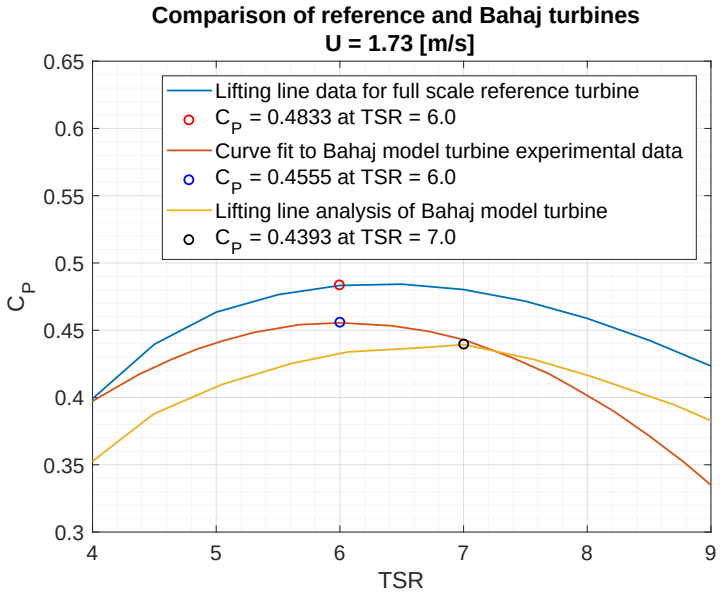

Figure 3.6: Reference full scale turbine lifting line data, Bahaj curve fit to experimental data of model turbine [19] and lifting line predictions of Bahaj model turbine [45].

3.3.3 Reference turbine blades

As mentioned before, the blades of the reference turbine are composed by the hydrofoils NACA 63-824, 63-821, 63-818, 63-815 and 63-812. Table 3.4 and figure 3.7 detail the information regarding the blades along their span.

Span r/R [%]	Foil at section	Reynolds Re [-]
20	NACA 63-824	3.9e+06
30	NACA 63-821	4.1e+06
45	NACA 63-818	5.3e+06
75	NACA 63-815	5.3e+06
100	NACA 63-812	7.2e+05

Table 3.4: Blade section information

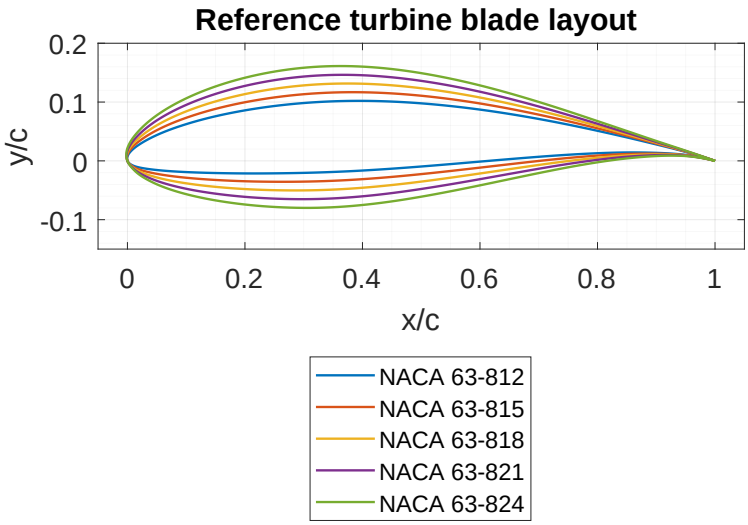

Figure 3.7: Blade section layout

3.4 Operating curves

Figure 3.8 displays the operating curves of the reference turbine, i.e the cavitation number σ and angle of attack α felt on the section along the blade span as it rotates azimuthally (Ψ = 0° to 360°).

The cavitation number is calculated through equation 3.1:

$$\sigma = \frac{p_\infty - p_v}{1/2 \cdot \rho {V_{eff}}^2} \tag{3.1}$$

The calculation of the effective flow speed at the section V_{eff} and the local inflow angle ϕ are described in the following subsections.

3.4.1 Effective flow speed $\mathbf{V_{eff}}$ calculation

In order to calculate the effective flow speed at a section V_{eff} in a manner that could be implemented in a computer routine, an analytical method based on [46] is adapted. This method originally consists on an analytical expression to calculate the probability of perturbations to the operational blade-section angle of attack, taking into account the combined influence of flow shear, yaw-misalignment and turbulence intensity. In this adaptation, for the sake of simplicity, flow stream turbulent perturbations on V_{eff} were

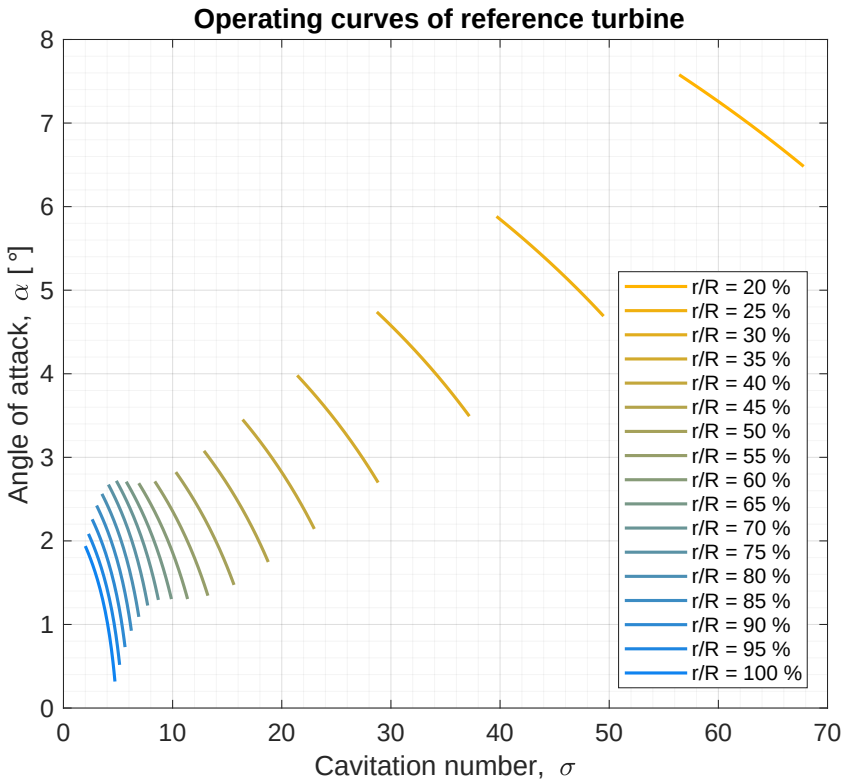

Figure 3.8: Operating curves of blade sections along the span - cavitation number vs AOA at section

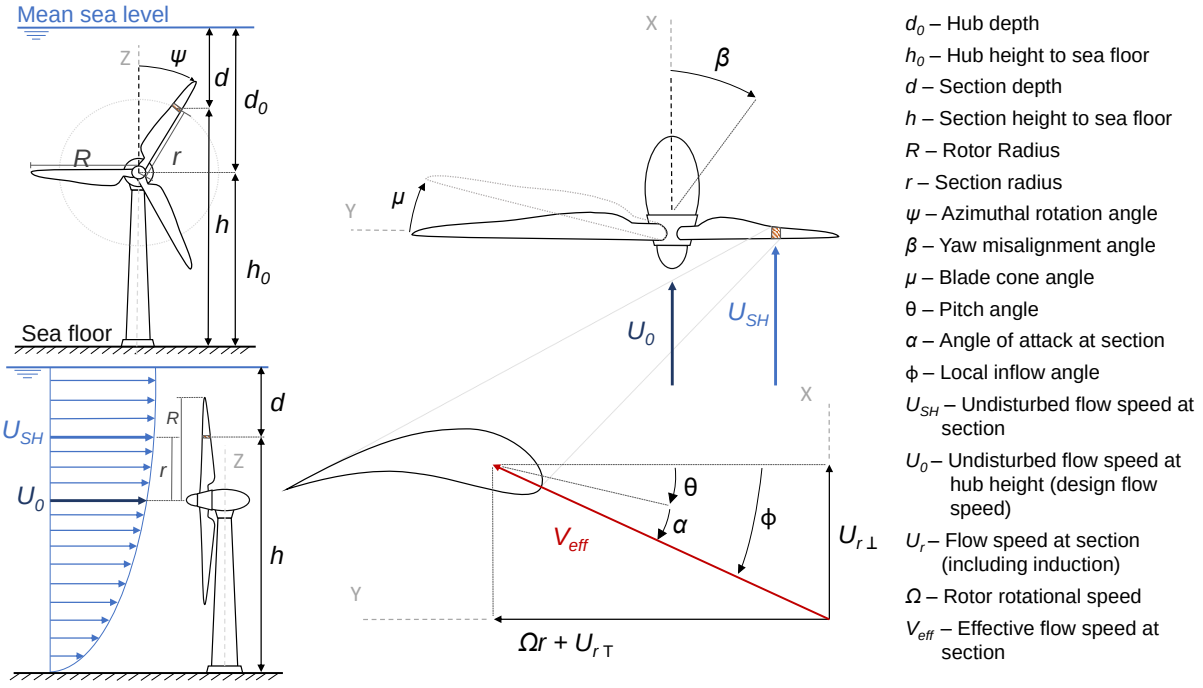

Figure 3.9: Overview and blade section view

not taken into account. The effective flow speed V_{eff} at the section is calculated through the following expression (refer to figure 3.9):

$$V_{eff} = \sqrt{U_{r\perp}^2 + (\Omega r + U_{r\top})^2} \tag{3.2}$$

where $U_{r\perp}$ and $U_{r\top}$ are as follows:

$$U_{r\perp} = U_{SH} \cdot \cos\beta \cdot (1 - a - K \cdot \sin\Psi) \tag{3.3}$$

$$U_{r\top} = U_{SH} \cdot \sin\beta \cdot \cos\Psi \tag{3.4}$$

where β is the yaw misalignment angle, a is the axial induction factor, Ψ is the azimuthal rotation angle, U_{SH} is the flow speed at the section (due to flow shear, SH, see figure 3.9) and K is the yaw misalignment factor, a parameter that depends on the radial coordinate and the yaw misalignment:

$$K = \frac{15\pi}{32} \cdot \frac{r}{R} \cdot \left(\frac{\beta(0.6 \cdot a + 1)}{2} \right) \tag{3.5}$$

Marine current shear is approximated by the logarithmic shear law:

$$U_{SH} = U_0 \frac{\ln h - \ln z_r}{\ln h_0 - \ln z_r} \tag{3.6}$$

where h is the section height, U_0 is the undisturbed flow speed at the hub height (see figure 3.9) and z_r is the roughness factor. This value is taken as 3 cm, according to [47], [48] and [49]. The section height is calculated as $h = h_0 \cdot rcos\Psi \cos\mu$, where μ is the rotor pre-bend or cone angle.

The axial induction factor a used in these calculations is a result of the lifting line routine mentioned in section 3.3.1, and thus the final result incorporates both analytical and computational methods. The tangential induction factor is not included in this method as it is considered negligible [46].

The results can be seen in table 3.5 as well as figure 3.10, for Ψ = 90° . The maximum difference between both sets of values is lower than 10% and decreases to less than 1% at the blade tip, which is acceptable (the reference value is resulting from lifting line predictions).

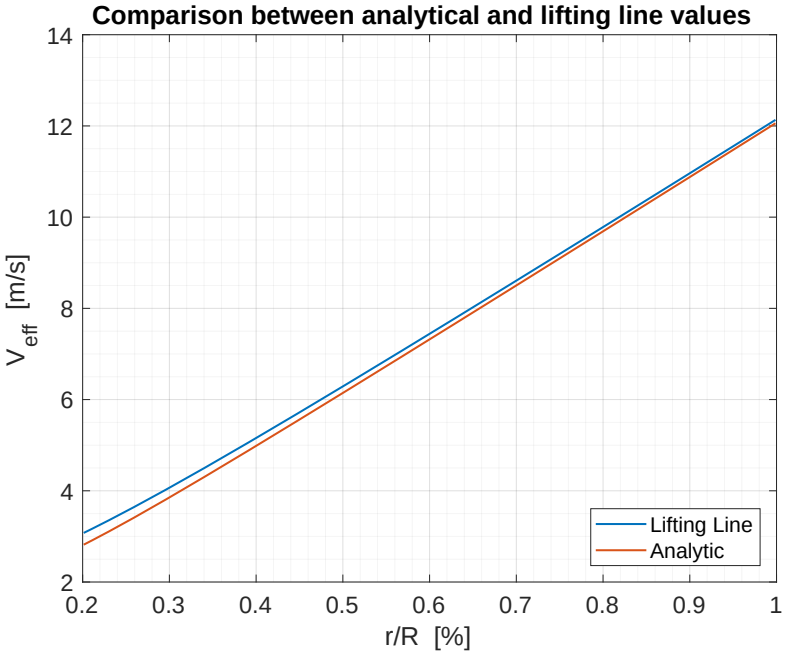

Figure 3.10: Comparison between analytical and computational values

Table 3.5: Comparison between analytical and computational values for V_{eff}

Span ratio r/R [%]	Analytical method V_{eff} [m/s]	Lifting line V_{eff} [m/s]	Relative difference [%]
20	2.82	3.08	8.38
21	2.91	3.17	8.02
23	3.11	3.36	7.32
26	3.41	3.64	6.38
30	3.81	4.02	5.34
34	4.30	4.50	4.34
39	4.88	5.06	3.48
45	5.53	5.68	2.77
51	6.22	6.36	2.22
57	6.95	7.08	1.81
63	7.69	7.81	1.49
69	8.42	8.53	1.25
75	9.13	9.23	1.07
81	9.80	9.89	0.93
86	10.40	10.49	0.83
90	10.93	11.01	0.75
94	11.37	11.45	0.69
97	11.71	11.79	0.65
99	11.94	12.02	0.63
100	12.06	12.13	0.61

Please note that despite being possible to calculate the yaw misalignment, rotor pre-bend and azimuthal rotation influences on the effective flow speed at the section through this analytical method, the results presented in table 3.5 and figure 3.10 do not show these effects because:

- The lifting line routine used considers uniform flow, i.e., shear flow influence is not calculated and thus is not taken into account ;
- The lifting line routine outputs the effective flow speed at each section corresponding to the turbines blade at the horizontal position, Ψ = 90° , thus a more complete comparison between analytical and lifting line values is not possible.

Despite the previous considerations, the values presented are still illustrative to the accuracy of the analytical method.

3.4.2 Local inflow angle ϕ calculation

Following the same logic as for V_{eff}, the local inflow angle ϕ calculation is based on the analytical method described in [46], and is calculated as follows:

$$\phi = \arctan\left(\frac{cos\beta \cdot (1 - a - K \cdot \sin\Psi)}{\lambda_r - \sin\beta\cos\Psi}\right) \tag{3.7}$$

where λ_r is the local TSR at the section r :

$$\lambda_r = \frac{\Omega \cdot r}{U_{SH}} = \frac{\Omega \cdot r}{U_0} \cdot \frac{\ln h_0 - \ln z_r}{\ln h - \ln z_r} \tag{3.8}$$

The angle of attack α is finally calculated as the difference between the local inflow angle ϕ and the local pitch angle θ : $\alpha = \phi - \theta$. For this calculation the computational value (obtained from the lifting line routine) of the axial induction factor a is used as well.

Although the influence of yaw misalignment as well as pre-bend angle on both V_{eff} and ϕ can be studied using this approach, as mentioned before, for the sake of simplicity, the reference turbine and the redesigned turbine presented in chapter 7 are considered to be fully aligned with the main flow direction (β = 0°) as well as having a rotor with no pre-bend (μ = 0°).

Chapter 4

Optimization Setup

In this chapter the design and optimization routine as well as the simulation specifications are briefly described. The cost functions developed to reach the intended hydrofoil-specific design goals are then described in detail.

4.1 Optimization tool - *OptiFlow*

The routine used for this work was originally conceived as a new airfoil design strategy, relying on the mathematical description of the foil shape with CST parametrization [50] and the NSGA-II multi-objective optimization algorithm to render optimal compromises between design goals. This optimization tool is here adapted for the first time to the design and optimization of hydrofoils, having been extensively used and proven effective for the design of optimized airfoils in previous efforts. The following subsections offer brief descriptions of several aspects concerning the optimization tool's characteristics and inner workings. For more detailed information the reader is referred to [22], [51], and [52].

4.1.1 Optimization framework

Optiflow is an optimization framework implemented in the *MATLAB* computing environment. Its code is built around an object-oriented data structure and relies on Symbolic Computation, Spline and Global Optimization toolboxes. The code's objects are designed following a team paradigm, meaning, each object can be conceived as a worker within a team which then call on other "workers" (objects) to execute tasks they are specialized in, namely:

- **system_context** - handles interaction with operating system and hardware;
- **simulation_worker** - executes simulations in RFOIL or XFOIL and requests shape generation;
- **shape_definition** - stores and uses information about the airfoil shape, using two parametrization objects (one for each side of he foil);
- **global_cost_function** - evaluates the complete cost function, reconditioning optimizer requests, handing simulations to the *simulation_worker* and their results to the interpretation functions;

- **gamultiobj_manager** - sets up and controls execution of the optimization algorithm.

The evaluation of the cost function is the most complex and time consuming operation in the optimization process, as it involves evaluating the quality of the airfoil, generating its geometry, writing a command file for R/XFOIL, executing the simulation, acquiring the data and interpreting the polar. This framework allows to perform several experiments on the same airfoil within the same optimization loop, for example, evaluate airfoil performance for natural and forced transition. Although it is not considered in the present work, it is also possible to consider actuation on the airfoils within the optimization framework.

4.1.2 Geometry parametrization

The Class Shape Transform CST parametrization method was developed at Boeing and is presented in detail in reference [50]. The airfoil (or hydrofoil) shape is represented as the product of two functions, a class $C_{(x)}$ and a shape $S_{(x)}$ function, summed with a trailing edge thickness function $z_{(x)}$.

$$t = S_{(x)}C_{(x)} + z_{(x)} \tag{4.1}$$

Each side of the airfoil is represented separately, as an analytical function of the relative thickness versus position, tailored with parameters that define the design. The class function provides the base airfoil shape, and the shape function is used to perturb the class function, thereby defining the design. The additional trailing edge thickness function allows for thick trailing edges to be represented accurately [22].

The class function is a simple analytical function providing the essential features of an airfoil shape, and is defined as:

$$C_{(x)} = (1-x)\sqrt{x} \tag{4.2}$$

In the CST method as presented in [50], the shape function is a Bezier curve, meaning, a weighted sum of Berstein polynomials; these polynomials are the basis functions used to generate the shape function $S_{(x)}$ as a linear combination with coefficients b_n:

$$S_{(x)} = \sum_{r=0}^{r=N-1} s_{(x)}^{rN} b_n \qquad \begin{cases} x \in [0,1] \subset \mathbb{R} \\ b_n \in \mathbb{R}^n \end{cases} \tag{4.3}$$

b_n is a 1-tensor holding the linear combination coefficients, and the basis functions are the complete set of Bernstein polynomials of order N and degree $N-1$, given analytically as:

$$s_{(x)}^{rN} = \binom{N-1}{r} x^r (1-x)^{n-r} \qquad \begin{cases} r \in [0, N-1] \subset \mathbb{Z} \\ \binom{n}{r} = \frac{n!}{r!(n-r)!} \end{cases} \tag{4.4}$$

A Bernstein polynomial order of 8 is employed in this work, as it is sufficient to cover the airfoil design space effectively [22], corresponding to a set of 17 parameters describing the airfoil shape, 8_{upper} + 8_{lower} + $1_{\text{trailing edge}}$. Other geometry constraints, such as maximum and minimum camber or thickness, are limited by the extreme values of reference feasible airfoils included in the optimization framework.

4.1.3 Hydrodynamic performance analysis tool - RFOIL

RFOIL-Suc is a fully coupled viscous-inviscid code based on XFOIL 5, modified by the Institute for Wind Energy to account for rotational effects on blade section performance, also featuring better stall prediction. Particular effort was put into strengthening the convergence properties of RFOIL, resulting in greater consistency and accuracy in results when compared to XFOIL, even for flow without rotational effects [22].

The inviscid flow problem is solved with a potential flow model using a vortex discretization of 160 or more panels. The viscous problem consists in the solution of the boundary layer equations and it is coupled with the potential problem using a virtual surface transpiration approach. Despite the progress made, both RFOIL and XFOIL still suffer from strong limitations for the simulation of thick profiles, specially in the presence of leading edge soiling.

4.2 Experimental measurements and X/RFOIL calculations data comparison

In this section, some brief considerations are made regarding the numerical accuracy of the performance analysis tool RFOIL and why it is used instead of XFOIL within the optimization framework. Both tools are integrated in *Optiflow* but the performance analysis for this work (within the optimization procedure) is carried out by RFOIL.

Figures 4.1a and 4.1b show a comparison of XFOIL, RFOIL and experimental measurements of the lift and drag coefficients, C_L and C_D, respectively, versus the angle of attack for foil NACA 63-815. Measurements are made at Re = $0.8{\cdot}10^6$. Calculations from XFOIL and RFOIL consider natural (free) transition and the N_{crit} value assumed is 4, as stated in section 3.2; experimental data comes from measurements made in a cavitation tunnel by Bahaj *et.al* [53].

From figures 4.1a and 4.1b it is possible to observe that RFOIL measurements are closer to the experimental values taken for most angles of attack measured and more so for high values of AOA. RFOIL appears to be exceptionally better than XFOIL at predicting C_L values for larger angles of attack (between 10° and 18°), as XFOIL largely over predicts them. Regarding C_D, both method appear off in their predictions, with RFOIL being more reliable for larger angles of attack (between 8° and 18°). This discrepancy between experimental and X/RFOIL values can be partly explained by the conditions in the experimental setup, as stated by Bahaj *et.al*: "... tests did not strictly simulate two-dimensional flow as there is the influence of the wall boundary layers at the ends of the span, the gap between the foil and the centre-line partition and possible interference drag with the base plate (...) trailing edge of the foils

was thickened a little for strength reasons. These are all likely to have contributed to an increase in drag above the true two-dimensional value" [53].

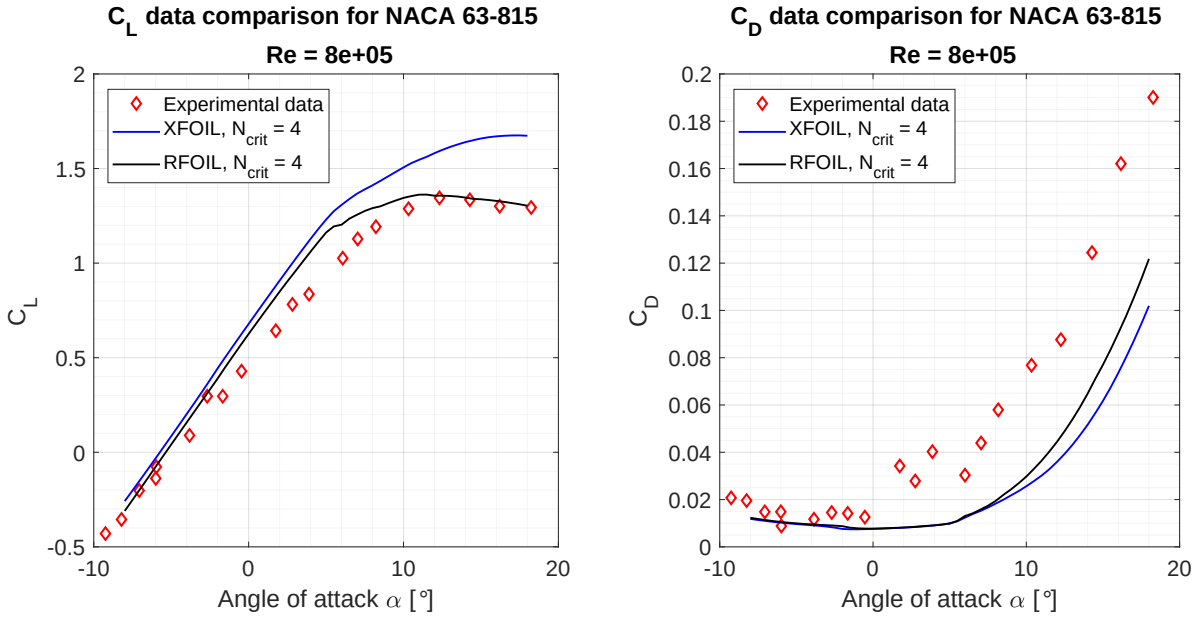

(a) Data comparison of lift coefficient C_L at Re = 0.8·10^6 for NACA 63-815

(b) Data comparison of drag coefficient C_D at Re = 0.8·10^6 for NACA 63-815

Figure 4.1: Data comparison of lift and drag coefficient between XFOIL, RFOIL and experimental values from reference [53] - measurements for foil NACA 63-815

Table 4.1 shows the relative difference between the minimum and maximum lift and drag experimental data and values calculated by X/RFOIL for the same AOA.

Table 4.1: Comparison between experimental maximum C_L and minimum C_D measurements and X/RFOIL calculations at the same AOA

	Lift coeff. at α = 12.3° C_L [-]	Relative difference [%]	Drag coeff. at α = -6° C_D [-]	Relative difference [%]
Exp. value	Max. exp. value 1.345	-	Min. exp. value 0.0088	-
XFOIL	1.592	18.4	0.0102	15.6
RFOIL	1.357	0.86	0.0105	19.2

From this table we can verify the remarkably lower relative difference in the maximum C_L value prediction by RFOIL compared to XFOIL. Regarding C_D, RFOIL slightly over predicts the value compared to XFOIL, but in figure 4.1b it is possible to observe that this tendency is inverted as predictions are made for larger AOA values. Validation of RFOIL calculations was not pursued as it falls out of the scope of the present work; for more details the reader is referred to [22] and [54].

In light of these considerations, allied to RFOIL's increased robustness when compared to XFOIL, this tool is preferred when making hydrofoil performance calculations within the optimization framework.

4.3 Simulation - Initial considerations

The genetic algorithm considers 100 foil candidates per generation and each optimization run considers 50 generations. The initial reference ”genetic” pool is composed of 40-60 airfoils and hydrofoils. The latter are mentioned in this way as they have been tested and experimented as foils adequate for marine turbines in previous work, like the NACA 63-8XX [53] and 66-8XX [55] series, and S1210, as it is the closest to the HF-Sx foil previously mentioned (refer to chapter 2).

Two specific hydrofoil performance cost functions are defined as design goals. Cost function 1, CF1, relates to hydrodynamic performance, contrasting with cost function 2, CF2, cavitation performance. Cavitation performance is defined as increasing the margin between cavitation number σ and the minimum pressure coefficient $C_{p_{min}}$, as mentioned in chapter 1. The evolution of both cost functions as well as the inner workings of the final CF1 and CF2 versions are further detailed in sections 4.4 and 4.5.

For each hydrofoil candidate, two lift and drag polars are calculated at a user defined Reynolds number in AOA steps of 0.5 degrees, for a range defined by the user. The first polar is obtained without prescribing the transition location (natural transition, also called free transition in this work) - this is termed the *clean configuration* or *clean regime*. For the second polar, transition is located at x/c = 10% and 5% (as proposed by Timmer *et.al* [56]) for the lower and upper faces, respectively - named *rough configuration* or *rough regime*. Letters **A**, **B** and **C** are used to specify when a simulation or cost function version is carried out or tested considering:

- **A** - only natural (free) transition ;
- **B** - only forced transition ;
- **C** - a weighted contribution of both regimes and respective polars.

Although forcing transition is not sufficient for simulating roughness, this is the common way of simulating soiled or rough surface on foils [56]. In order to be more accurate, RFOIL would have to calculate foil performance with other velocity profiles other than the Swafford velocity profiles [22].

The objective of an optimization of type C is to obtain hydrofoils that have a balanced performance between clean and rough regime. The way this is made is explained for each specific cost function version in the subsequent sections. It is important to point out that in all optimizations of type C the value of CF1 is composed by a weighted average of the lift to drag ratio in both clean and rough regimes, and thus does not represent the value of L/D of the respective hydrofoil in either regime. Unlike type C, the value of CF1 for types A and B directly represents the value of L/D for the clean and rough regimes, respectively. The value of CF2 directly represents the cavitation margin of the given hydrofoil for any type of CF1 version.

Each hydrofoil candidate is evaluated by CF1 and CF2 and receives a ”score” according to its performance. Each optimized hydrofoil has a unique score when considering a specific cost function. These scores are then displayed in a Pareto front, which is composed by the set of design CF scores, or design points, that are Pareto efficient, i.e., it is impossible to increase one of the objective function’s value without decreasing the other (see figure 4.2). This also means that each point in the Pareto fronts in the following sections represents an optimized hydrofoil.

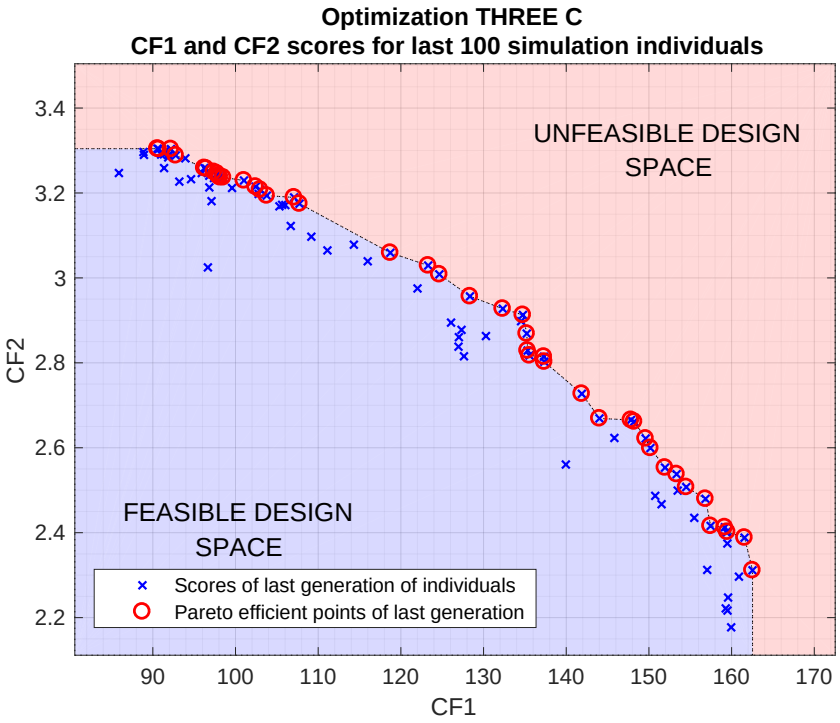

Figure 4.2: Pareto efficient points in last generation of simulation THREE C

For the reader's better comprehension of these cost functions and corresponding results, CF2 is described first.

4.4 Cavitation margin cost function - CF2

Cost function 2, CF2, is related with the cavitation margin experienced at each section for each foil, and is calculated as follows:

$$\mathbf{CF2} = (\sigma_{\mathbf{r/R}})_{\mathbf{min}} - (-\mathbf{C}_{\mathbf{p_{min}}})_{\mathbf{max}} \tag{4.5}$$

$\sigma_{r/R})_{min}$ is calculated through the method described in section 3.4. Hence, it corresponds to the minimal cavitation number of each operation curve (see figure 3.8), for each section of the turbine blades. $(-C_{p_{min}})_{max}$ corresponds to the minimum C_p value found within the range of operating angles of attack of the hydrofoil at the section, meaning:

- The AOA$_{opt}$ is the AOA at which the foil exhibits the highest L/D value ;
- C_p distribution around the foil is calculated for angles of attack ranging between $AOA_{opt} - {}^{\Delta\alpha}/_2 \rightarrow AOA_{opt} + {}^{\Delta\alpha}/_2$, being $\Delta\alpha$ the variation in angle of attack experienced at the section (see figure 3.8) ;
- The minimum value of $C_{p_{min}}$ for this whole range, which corresponds to $(-C_{p_{min}})_{max}$, is taken.

Through this method, a positive cavitation margin is ensured for the whole range of AOA at which a foil will operate at the given section, i.e., a positive cavitation margin is ensured for the totality of the blades' rotation at design conditions. If the value of CF2 is negative, cavitation will most likely occur.

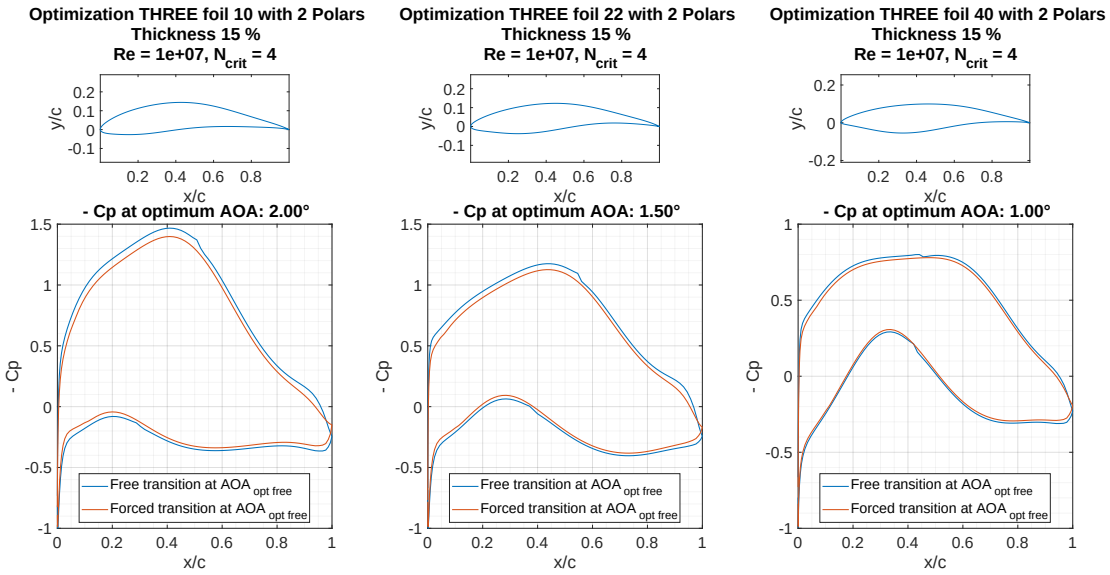

(a) $-C_p$ distribution of foil 10 of opt. THREE C

(b) $-C_p$ distribution of foil 22 of opt. THREE C

(c) $-C_p$ distribution of foil 40 of opt. THREE C

Figure 4.3: Comparison of $-C_p$ distributions for various foils in the same Pareto front
$-C_p$ distribution calculated for clean and rough regimes at the same AOA

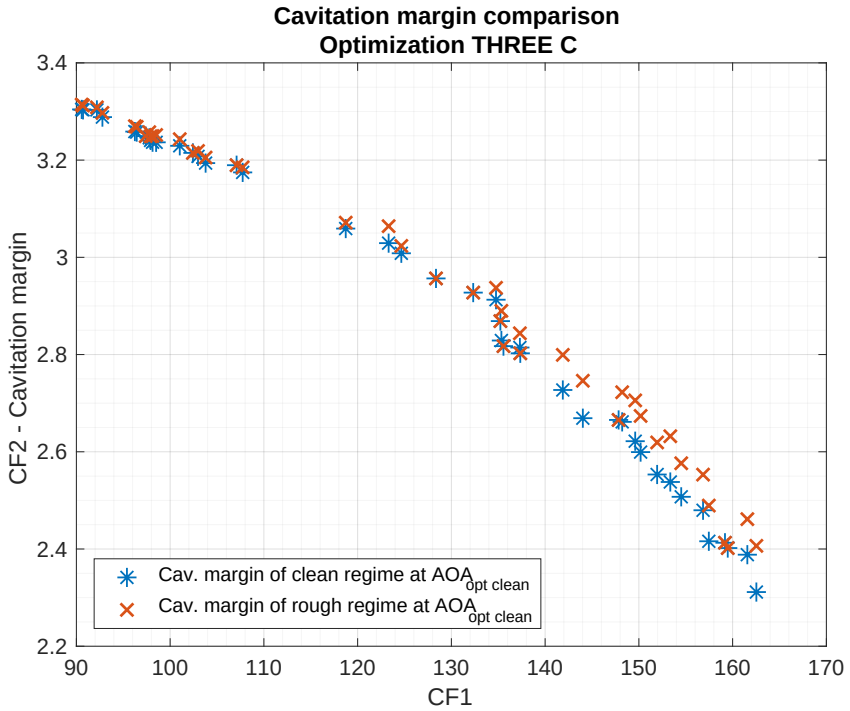

Figure 4.4: Cavitation margin comparison between clean and rough regimes

C_p distribution is always calculated only for the clean regime. With forced transition, for the same AOA, the suction peak is always weaker (as illustrated in figure 4.3, the highest value of $-C_p$ is always lower for the rough regime). This happens because the turbulent boundary layer is thicker than the laminar boundary layer, which makes the hydrofoil be perceived within the flow as having less camber, thus making the suction peak less intense. In figure 4.4 it is possible to observe that the cavitation margin is always equal or higher in the rough regime than in the clean regime.

For the section at r/R = 75% and an effective flow speed V_{eff} of 9.1 m/s, a decrease in cavitation

margin (CF2) of 1 unit requires an increase in V_{eff} of $\approx$ 2.4 m/s. This means that, for the cavitation margin to decrease by 1, the flow speed at this section would have to increase by 2.4 m/s, which is substantial. For this to occur, the rotational speed of the turbine Ω would have to increase by 3.07 rpm at TSR of 6. This could occur if the rotor decouples from the generator. Rotational speed would increase as there would be no momentum to counteract the hydrodynamical momentum felt by the rotor. On the other hand, due to in-flow vortices of small scale, axial flow speed can abruptly increase momentarily and locally. An increase of U_0 by 1 m/s, becoming U_0 = 3 m/s, while maintaining rotational speed at Ω = 1.2, yields an increase of AOA by approximately 6 degrees. For this hydrofoil, this AOA change increases the value of $-C_{p_{min}}$ by 1.6, which could possibly lead to cavitation.

4.5 Cost function 1 - Hydrodynamic performance

In this section, the evolution of cost function 1, CF1, is described in detail. Table 4.2 is left as a summary, containing the final version of each cost function generation. The objectives and additional conditions are detailed in the subsequent sections.

The improvement of CF1 was made considering the section at r/R = 75% and Reynolds of $1{\cdot}10^7$, which is representative of a turbine blade section at full scale [20]. Maximum thickness was specified as t/c_{max} = 15% (except for version ZERO, which was left free).

Table 4.2: Cost function 1 history

Version of CF1	Type of optimization (transition)	Objective	Additional conditions
ZERO	A - Free (natural)	L/D maximization at AOA$_{optfree}$	-
ONE	A - Free (natural) B - Forced C - Both contributions	L/D maximization at AOA$_{optfree}$	Imposition of C_L >0.2
TWO	A - Free (natural) B - Forced	L/D maximization weighted with azimuthal rotation influence	Imposition of C_L >0.2 AOA$_{opt}$ is not close to the edge of the AOA range Trailing edge minimum thickness specification
THREE	A - Free (natural) B - Forced C - Both contributions	L/D maximization weighted with azimuthal rotation influence	Imposition of C_L >0.6 AOA$_{opt}$ is not close to the edge of the AOA range Trailing edge minimum thickness specification
FOUR	A - Free (natural) B - Forced C - Both contributions	L/D and C_L maximization weighted with azimuthal rotation influence	Imposition of C_L >0.6 AOA$_{opt}$ is not close to the edge of the AOA range Trailing edge minimum thickness specification Direct comparison with reference values
FIVE	A - Free (natural) C - Both contributions	(L/D and C_L)^2 maximization weighted with azimuthal rotation influence	Imposition of C_L >0.6 AOA$_{opt}$ is not close to the edge of the AOA range Trailing edge minimum thickness specification Direct comparison with reference values

4.5.1 Version ZERO

This is the very first version of CF1. Quite simply, its objective is to maximize L/D at the optimum AOA of the free (natural) transition (clean) regime (AOA$_{optfree}$). However, this procedure incurs in point design, i.e., hydrofoils that have very good performance at a specific AOA and much poorer in others. This is to be avoided because, as seen in section 3.4, the rotation of the blades induces variation of AOA and it is intended that designed hydrofoils have good performance in all operating conditions.

4.5.2 Version ONE

As the cavitation margin obtained in version ZERO was high, an effort was made to limit the minimum value of optimum C_L while maintaining the objective of CF1 version ZERO.

In optimization **ONE C** (**CF1 version ONE with contributions from both polars**), the value of CF1 is calculated as follows:

$$\mathbf{CF1 = 0.5 \cdot L/D_{free} + 0.5 \cdot L/D_{forced}} \tag{4.6}$$

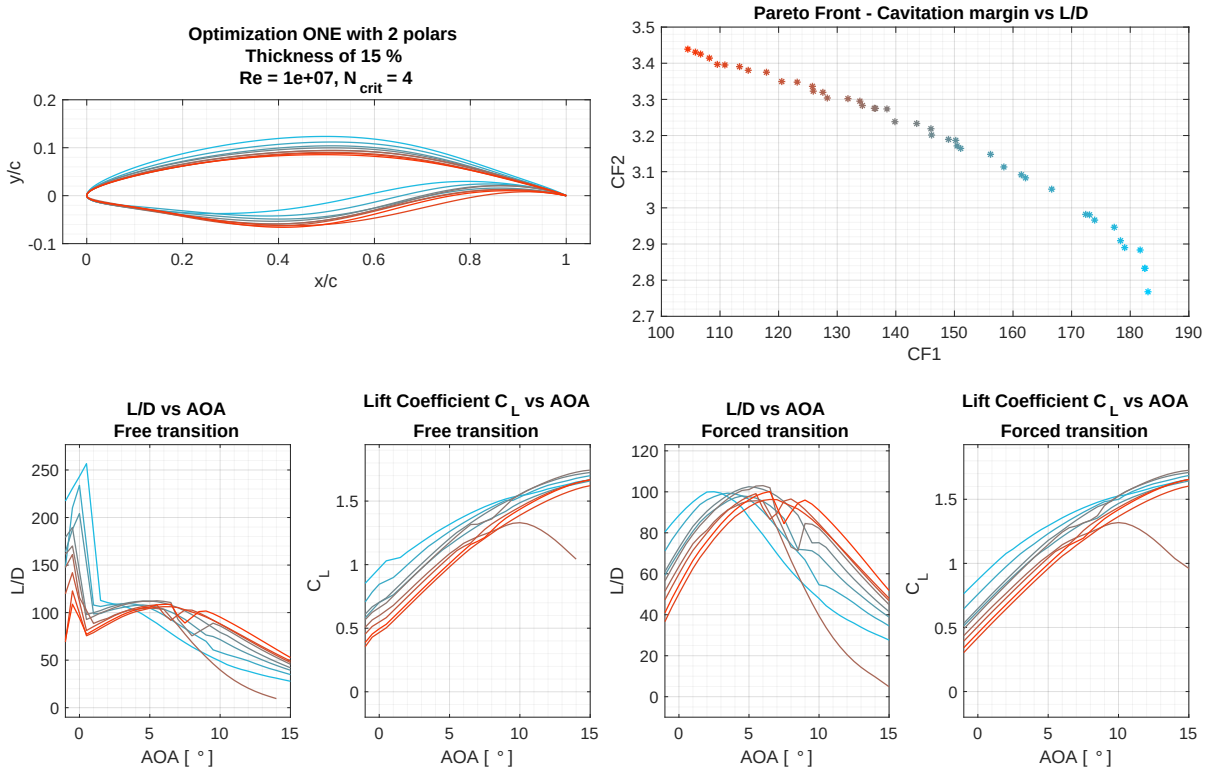

Figure 4.5: Foils, Pareto front and L/D obtained with CF1 ONE C

The results are presented in figure 4.5 - foils obtained, Pareto front, L/D curves as well as C_L polars for both regimes. The value of L/D_{forced} is, as the name indicates, the value of L/D in the rough regime, calculated at the AOA$_{optfree}$ (not the AOA that maximizes L/D_{forced}). The objective, as mentioned before, is to obtain hydrofoils which have a balanced performance for both clean and rough regimes at the clean regime optimum angle of attack.

4.5.3 Version TWO

Version TWO of CF1 is the pioneer of two very important modifications.

The first is the imposition of a minimum thickness for the trailing edge. This is carried out taking into account reference hydrofoils (NACA 63-8XX series) and ensuring that the new foil trailing edge thickness is not smaller than a fraction of the thickness of the reference foils at the specified coordinate, i.e.:

- $t/c_{\,new\ foil}|_{x/c=90\%} = 0.7 \cdot t/c_{\,NACA63-8XX}|_{x/c=90\%}$
- $t/c_{\,new\ foil}|_{x/c=75\%} = 0.7 \cdot t/c_{\,NACA63-8XX}|_{x/c=75\%}$

The factor used while developing CF1 was of 0.7, as indicated above. The thickness is specified to ensure that the resulting hydrofoils are feasible from a production point of view, i.e., that they are not fragile and have realistic thickness at the trailing edge, being possible to manufacture.

The second is the accounting of the influence on the angle of attack of the azimuthal rotation of the blades. This is done in the following manner:

$$\begin{gathered}\mathbf{CF1} = \mathbf{L/D^{weighted}} = \mathbf{w_1} \cdot \mathbf{L/D}\,|_{\mathbf{AOA_{i-j}}} + \mathbf{w_0} \cdot \mathbf{L/D}\,|_{\mathbf{AOA_i}} + \mathbf{w_2} \cdot \mathbf{L/D}\,|_{\mathbf{AOA_{i+j}}} \\ w_1 = w_2 = 0.25 \qquad w_0 = 0.5 \\ AOA_i = AOA_{opt} \\ AOA_{i-j} = AOA_{opt} - {}^{\Delta\alpha}/_2 \qquad AOA_{i+j} = AOA_{opt} + {}^{\Delta\alpha}/_2\end{gathered} \tag{4.7}$$

$\Delta\alpha$ is the variation in angle of attack experienced at the section; in this case, r/R = 75% (see figure 3.8). This means that the value of L/D is weighted between the value of L/D at the minimum and maximum AOA experienced at that section, as well as the optimum AOA, according to the relative weights w_x. This procedure mitigates the appearance of point-design type hydrofoils, i.e., results in hydrofoils which have balanced performance for the range of AOAs experienced at the given section (see figures 4.6 and 4.7). This cost function version assumes that the rotor blades are designed so that sections work near the optimum AOA.

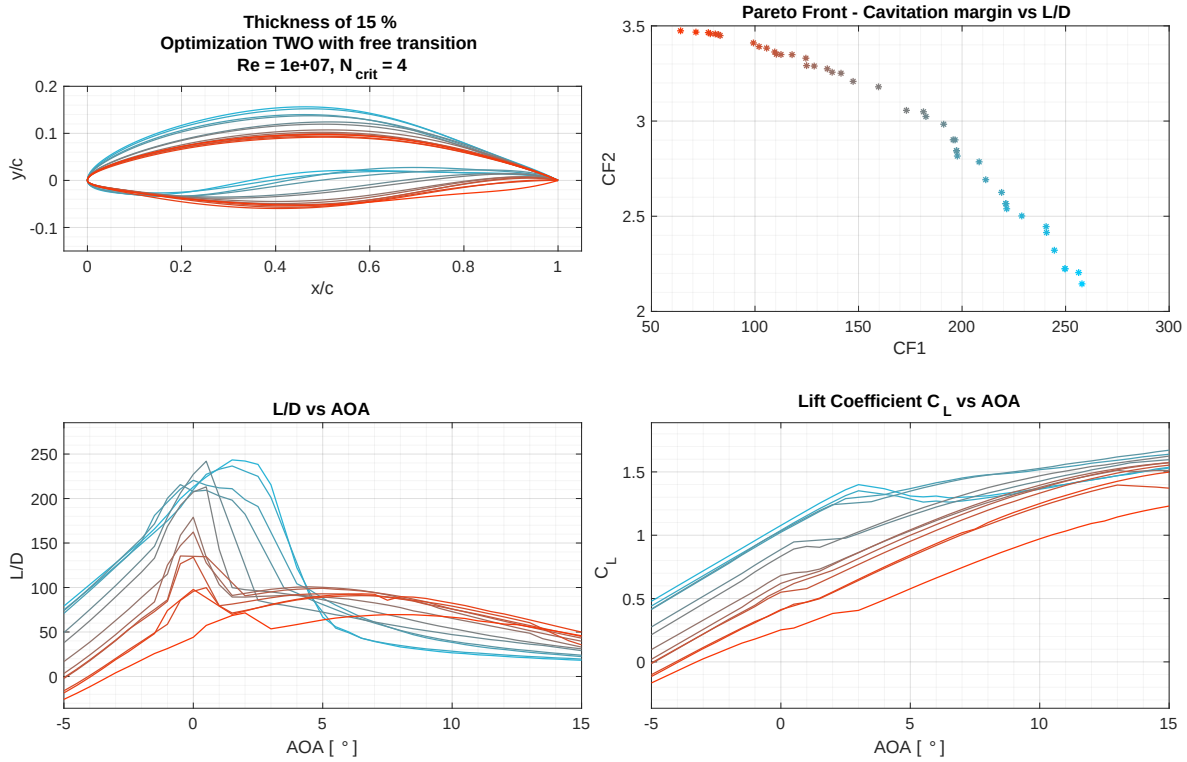

Figure 4.6: Foils, Pareto front and L/D obtained with CF1 TWO and free (natural) transition

Another important modification is the range of AOA for which polars are calculated. Version ZERO and ONE consider a range of -1 to 15 degrees while version TWO considers -5 to 15. For foils with

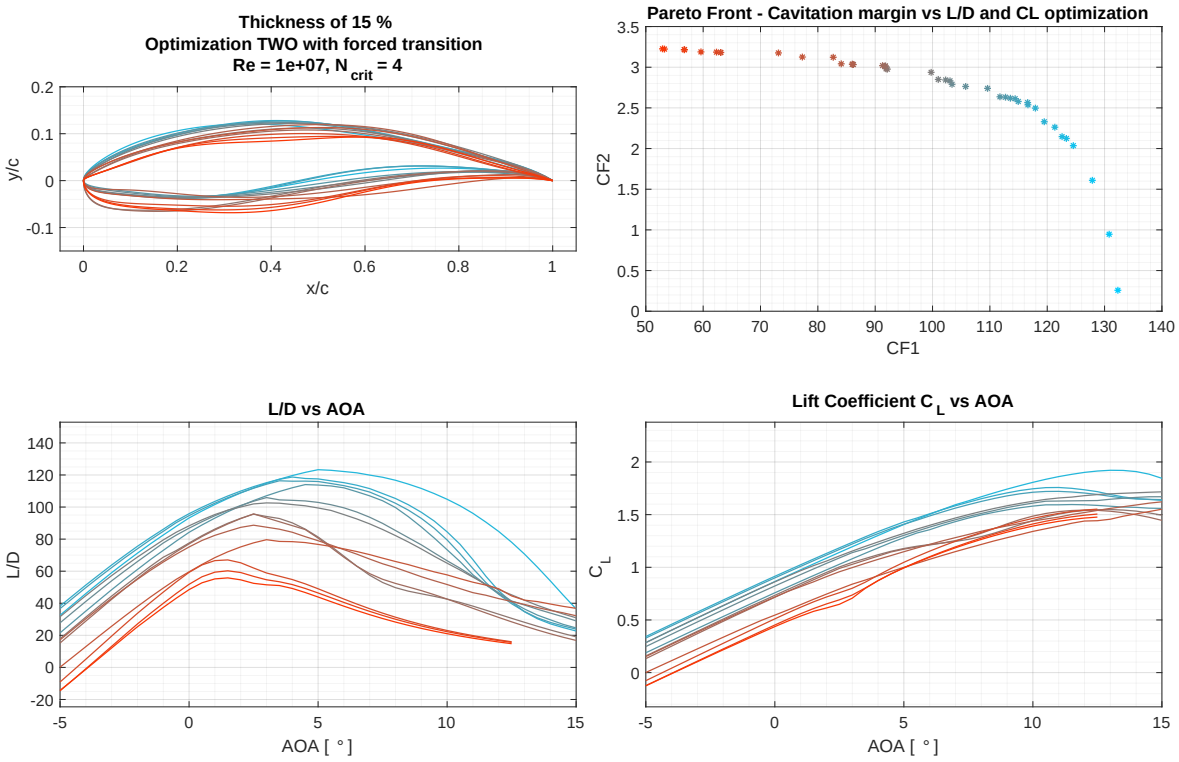

Figure 4.7: Foils, Pareto front and L/D obtained with CF1 TWO and forced transition

greater cavitation margin, the optimum angle of attack falls closer to zero for both clean and rough regimes, which is much too close to the edge of the study range. Also, with the inclusion of the azimuthal rotation influence, the increase of this range is needed in order to make a broader study and have a better understanding of maximum L/D for the various operating angles of attack.

Having successfully observed the effects of the modifications of version TWO on the values of CF1 and CF2 with optimizations of type A and B, a type C optimization was skipped.

It is very interesting to observe how the difference in flow regime dramatically alters the shape of the hydrofoil, namely, the maximum thickness and camber positions. Naturally, the values of L/D are much lower in forced than in free (natural) transition, and also, it is possible to notice how the optimization routine had to broaden the range in CF2 in order to reach higher values of CF1 for forced transition.

4.5.4 Version THREE

Version THREE is very similar to version TWO, featuring in addition the specification that the optimum lift coefficient, $C_{L\,opt}$, be higher than 0.6, which enables comparison with the NACA 6 series airfoils, taken as reference.

The value of CF1 version THREE C is calculated as:

$$
\begin{aligned}
L/D_{free}^{weighted} &= w_1 \cdot L/D_{free}\,|_{AOA_{i-j}} + w_0 \cdot L/D_{free}\,|_{AOA_i} + w_2 \cdot L/D_{free}\,|_{AOA_{i+j}} \\
L/D_{forced}^{weighted} &= w_1 \cdot L/D_{forced}\,|_{AOA_{i-j}} + w_0 \cdot L/D_{forced}\,|_{AOA_i} + w_2 \cdot L/D_{forced}\,|_{AOA_{i+j}} \\
AOA_{i-j} &= AOA_{opt} - \Delta\alpha/2 \qquad AOA_i = AOA_{opt\,clean} \qquad AOA_{i+j} = AOA_{opt} + \Delta\alpha/2
\end{aligned}
\tag{4.8}
$$

$$
\mathbf{CF1 = 0.5 \cdot L/D_{free}^{weighted} + 0.5 \cdot L/D_{forced}^{weighted}}
$$

This results in hydrofoils with both balanced performance for AOAs experienced at the section as well as clean and rough regime. Trailing edge minimum thickness specification and others remain. The results can be seen in figure 4.8.

Hydrofoils of version THREE C have a lower L/D_{max} than those of versions ONE C, TWO A and TWO B due mainly to two reasons:

- Regarding version ONE C: due to the shorter AOA range, this version is still incurring in point design, which can be observed from the very high values and then sharp decline of the L/D curves in free transition;
- Regarding versions TWO A and TWO B: these versions were specially optimized for each regime, clean and rough, respectively, while version C accounts and optimizes for both regimes simultaneously, yielding hydrofoils of balanced instead of regime-focused performance. These results also prove the optimization framework's efficiency in acquiring objective driven results.

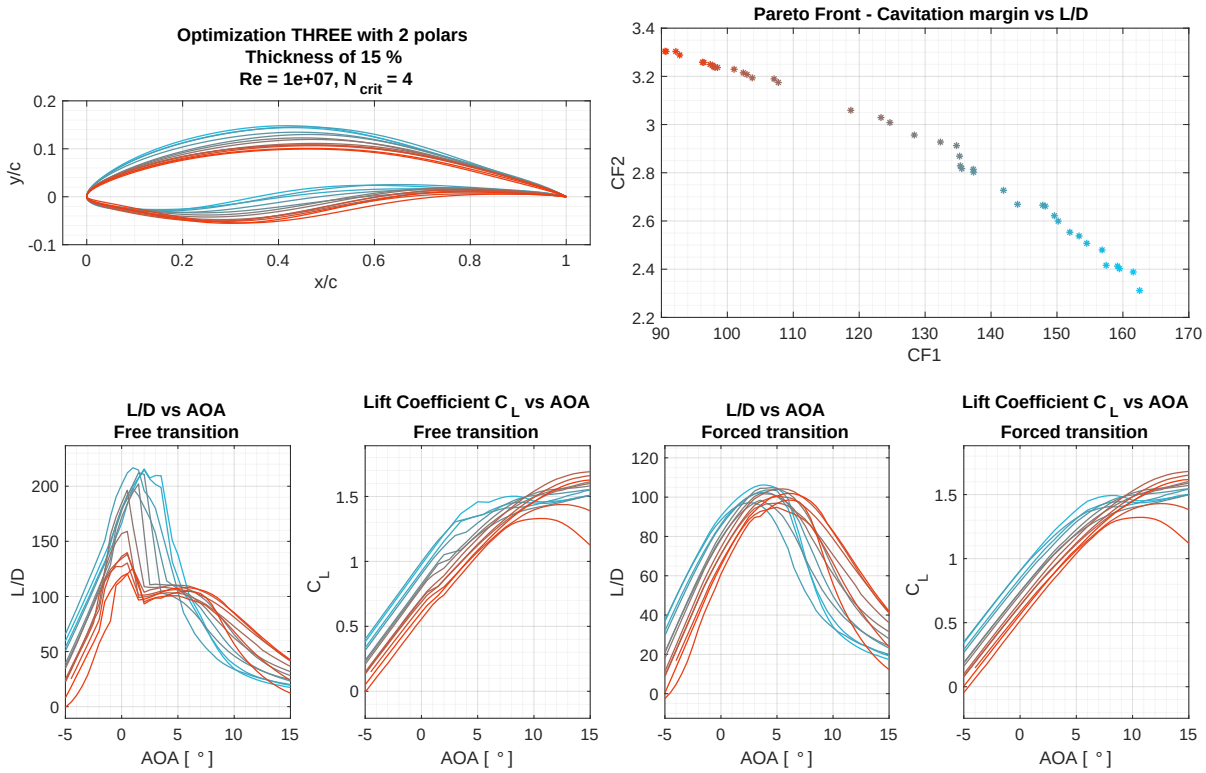

Figure 4.8: Foils, Pareto front and L/D obtained with CF1 THREE C

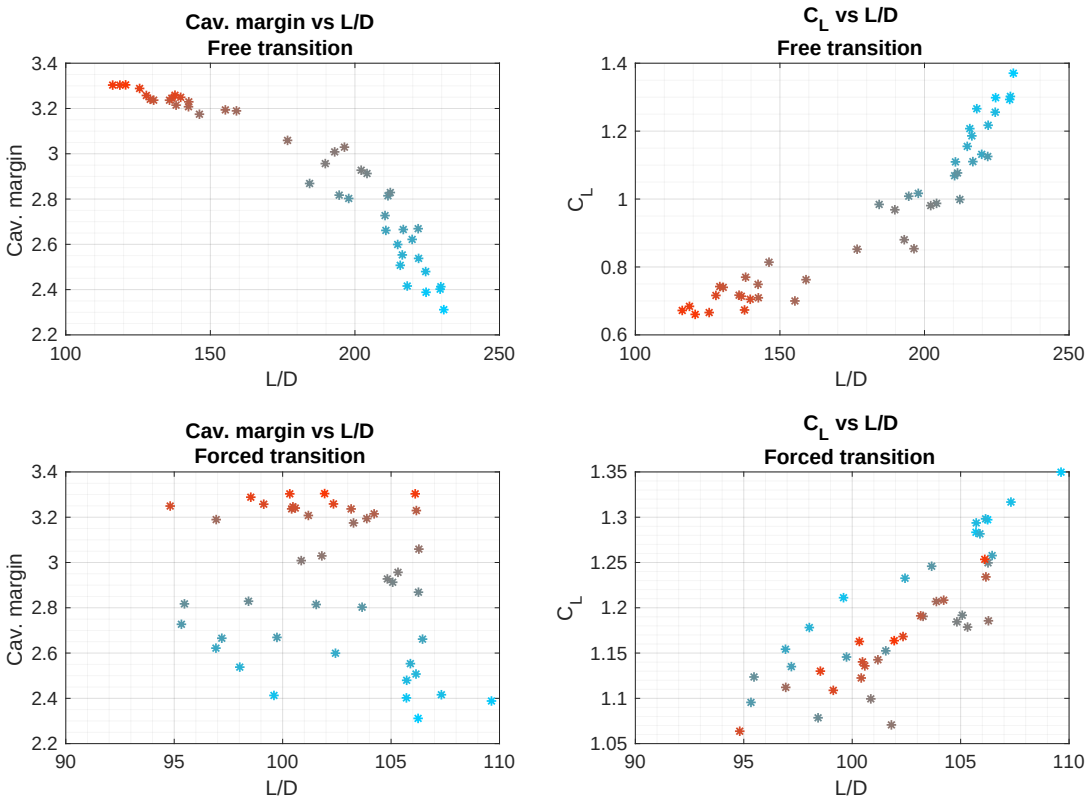

Figure 4.9: Version THREE C of CF1 - Comparison of free and forced transition regimes with various distributions

Also, notice how the hydrofoils of version THREE C seem to have a shape which is the ”average” of those from versions TWO A and B, i.e., the maximum thickness and camber position seem to be intermediate. Figure 4.9 displays the cavitation margin vs L/D_{opt} and $C_{L\,opt}$ vs L/D_{opt} of both regimes for all foils in the Pareto front. Notice how the lower value of $C_{L\,opt}$ is set at 0.6, as mentioned before, and tops at 1.4 for free (natural) and 1.35 for forced transition, as L/D tops at 230 for free (natural) and 110 for forced transition respectively.

4.5.5 Version FOUR

In this version of CF1, the optimization of the lift coefficient C_L at AOA$_{opt\,clean}$ is included as an objective. This version also features direct comparison with the reference foils.

The value of CF1 is calculated as follows:

$$\mathbf{n = number\ of\ reference\ hydrofoils}$$

$$L/D_n^{weighted} = w_1 \cdot L/D_n\,|_{AOA_{i-j}} + w_0 \cdot L/D_n\,|_{AOA_i} + w_2 \cdot L/D_n\,|_{AOA_{i+j}}$$

$$C_{L\,n}^{weighted} = w_1 \cdot C_{L\,n}\,|_{AOA_{i-j}} + w_0 \cdot C_{L\,n}\,|_{AOA_i} + w_2 \cdot C_{L\,n}\,|_{AOA_{i+j}}$$

$$\mathbf{C_L^{ref} = \frac{\sum_{n=1}^{n} C_{L\,n}^{weighted}}{n}} \qquad \mathbf{L/D^{ref} = \frac{\sum_{n=1}^{n} L/D_n^{weighted}}{n}} \tag{4.9}$$

$$L/D_{new\ foil}^{weighted} = w_1 \cdot L/D\,|_{AOA_{i-j}} + w_0 \cdot L/D\,|_{AOA_i} + w_2 \cdot L/D\,|_{AOA_{i+j}}$$

$$C_{L\,new\ foil}^{weighted} = w_1 \cdot L/D\,|_{AOA_{i-j}} + w_0 \cdot L/D\,|_{AOA_i} + w_2 \cdot L/D\,|_{AOA_{i+j}}$$

$$\mathbf{C_{L\,new\ foil}^{adim} = \frac{C_{L\,new\ foil}^{weighted} - C_L^{ref}}{C_L^{ref}}} \qquad \mathbf{L/D_{new\ foil}^{adim} = \frac{L/D_{new\ foil}^{weighted} - L/D^{ref}}{L/D^{ref}}}$$

$$\mathbf{CF1 = 0.5 \cdot \left[C_{L\,new\ foil}^{adim} + L/D_{new\ foil}^{adim}\right]_{free} + 0.5 \cdot \left[C_{L\,new\ foil}^{adim} + L/D_{new\ foil}^{adim}\right]_{forced}}$$

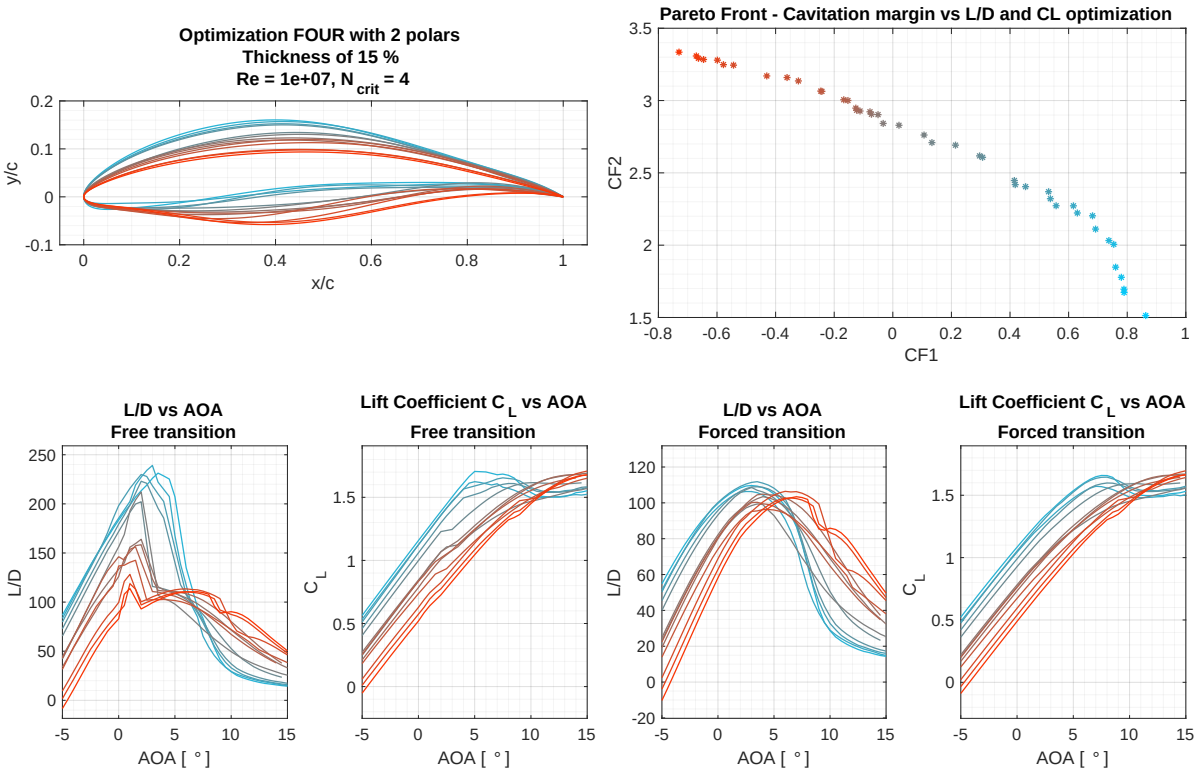

Figure 4.10: Foils, Pareto front and L/D obtained with CF1 FOUR C

The lift coefficient and L/D values of the new foil are thus directly compared to the reference foil and the relative difference between them is then maximized, taking into account the balancing of free (natural) and forced transition performance as in previous versions of CF1 C.

The reference hydrofoils chosen are from series NACA 63-8XX and NACA 66-8XX (the latter are included as suggested by Abadia [55] for having better cavitation behaviour than NACA 63-8XX series). XX stands for the foil maximum thickness (in this case, 15%). The results for this version of CF1 can be seen in figure 4.10. All other specifications remain (see table 4.2).

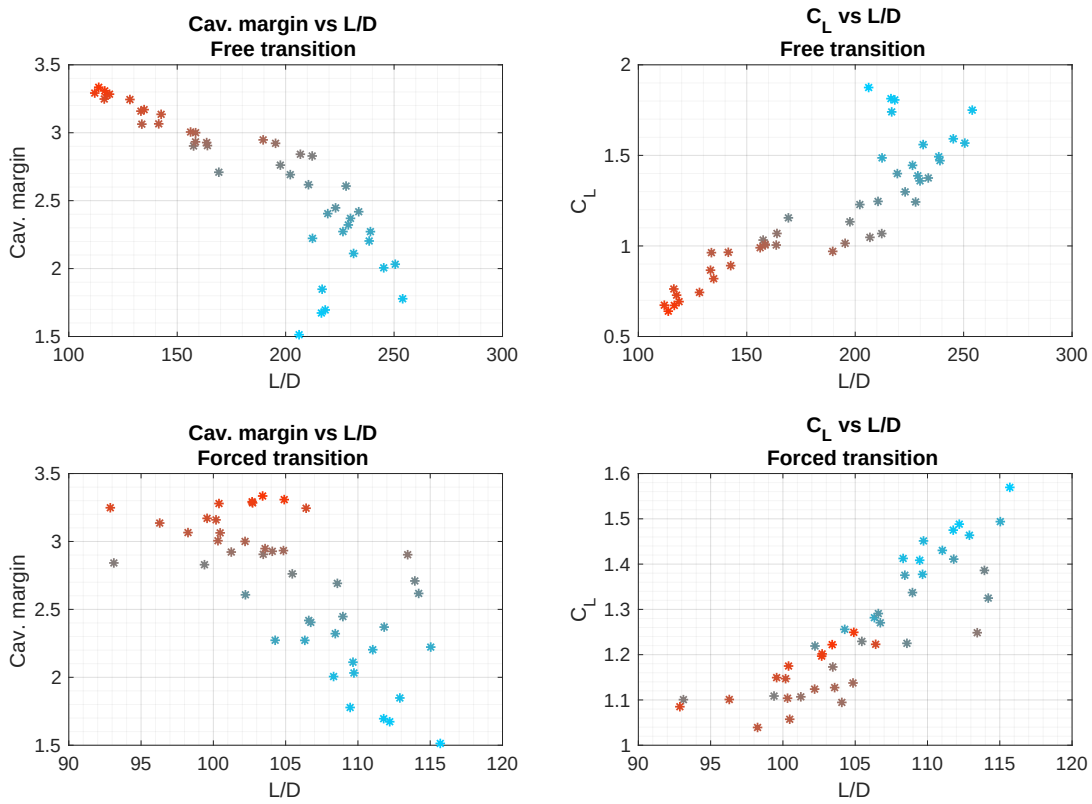

Figure 4.11: Version FOUR C of CF1 - Comparison of free (natural) and forced transition regimes with various distributions

Comparing figures 4.11 and 4.9, it is possible to see an increase in the value of $C_{L\,opt}$ for both regimes. This happens at the expense of cavitation margin, as it is plain to see by the slight broadening of CF2 range. For this CF version, C_{Lopt} tops at 2 and at 1.6 for free (natural) and forced transition, respectively. Also, there is a slight increase in optimum L/D value for forced transition.

4.5.6 Version FIVE

Version FIVE of CF1 is very similar to FOUR:

$$\mathbf{C_L^{ref}} = \frac{\sum_{\mathbf{n=1}}^{\mathbf{n}} \mathbf{1.1 \cdot C_{L\,n}^{weighted}}}{\mathbf{n}} \qquad \mathbf{L/D^{ref}} = \frac{\sum_{\mathbf{n=1}}^{\mathbf{n}} \mathbf{1.1 \cdot L/D_n^{weighted}}}{\mathbf{n}}$$

$$\mathbf{C_{L\,new\,foil}^{adim}} = \left(\frac{\mathbf{C_{L\,new\,foil}^{weighted} - C_L^{ref}}}{\mathbf{C_L^{ref}}} + \mathbf{1} \right)^{\mathbf{2}} \qquad \mathbf{L/D_{new\,foil}^{adim}} = \left(\frac{\mathbf{L/D_{new\,foil}^{weighted} - L/D^{ref}}}{\mathbf{L/D^{ref}}} + \mathbf{1} \right)^{\mathbf{2}}$$

$$\mathbf{CF1 = 0.5 \cdot \left[C_{L\,new\,foil}^{adim} + L/D_{new\,foil}^{adim} \right]_{free} + 0.5 \cdot \left[C_{L\,new\,foil}^{adim} + L/D_{new\,foil}^{adim} \right]_{forced}} \tag{4.10}$$

The objective of formulation 4.10 was to further increase the value of C_L and L/D, taking advantage of the large cavitation margin seen in previous versions. The addition of 1.1 and the inclusion of the square (^{2}) factor direct the optimization tool for the increase of CF1 to a larger detriment of the value of CF2. See [22] for additional information. The resulting foils, Pareto front, L/D curves and C_L polars can be seen in figure 4.12.

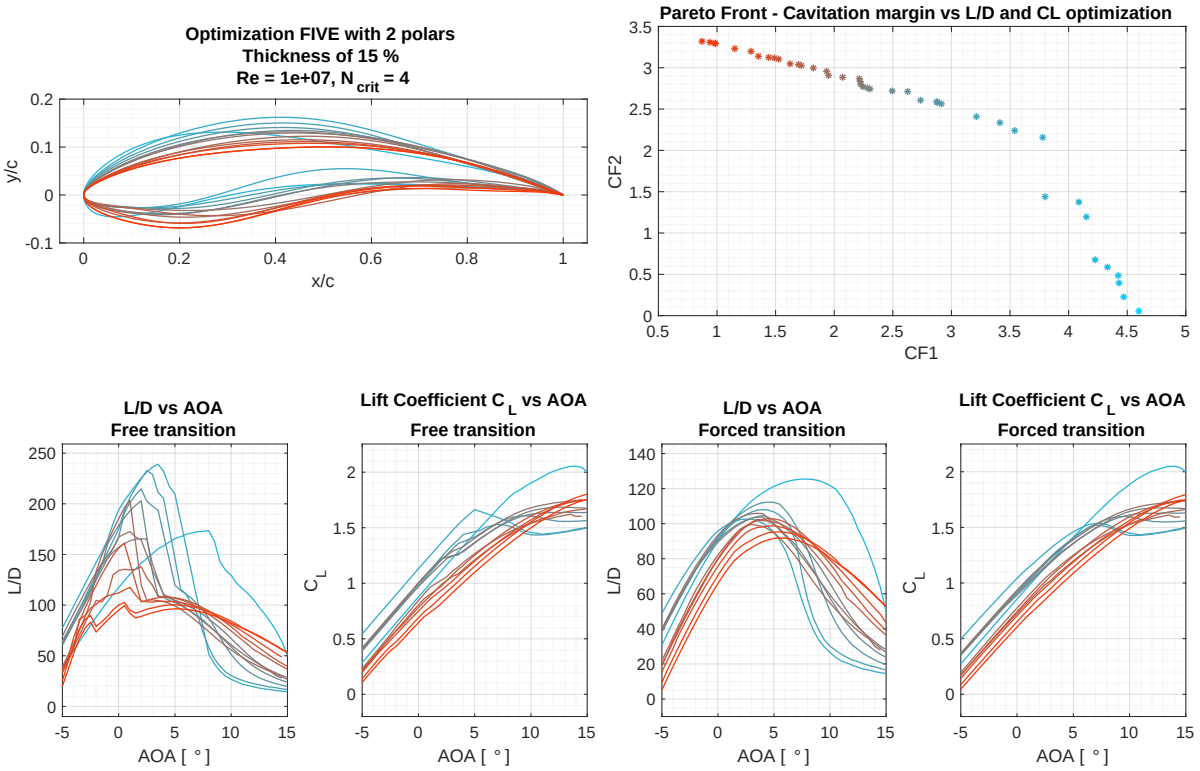

Figure 4.12: Foils, Pareto front and L/D obtained with CF1 FIVE C

There is, in fact, a slight increase in $C_{L\,opt}$ for both regimes due to these changes, as it is possible to observe in figure 4.13. Optimization FIVE C also rendered hydrofoils with higher L/D_{opt} for the rough regime than previous C versions, yielding values similar to version TWO B. It seems as this isolated cluster of foils results of an effort by the optimization setup to increase the maximum value of C_L for both regimes, which results ultimately in a loss of performance in terms of L/D in the clean regime. This result also resulted in a CF2 range between 0 and 3.5, the largest of all versions, and despite C_L and L/D values show a cluster, the Pareto front presents an adequate distribution. It could be said that this cost function fully explores the design space for these conditions.

After the many iterations described along this chapter, version FIVE C of CF1 is chosen as the final version of the cost function, yielding hydrofoils with good cavitation margin as well as a balanced performance between clean and rough regimes, while also assuring the feasibility of the hydrofoils when it comes to structural integrity.

It must be stressed that, because of the way CF1 version FIVE C is formulated, picking a hydrofoil

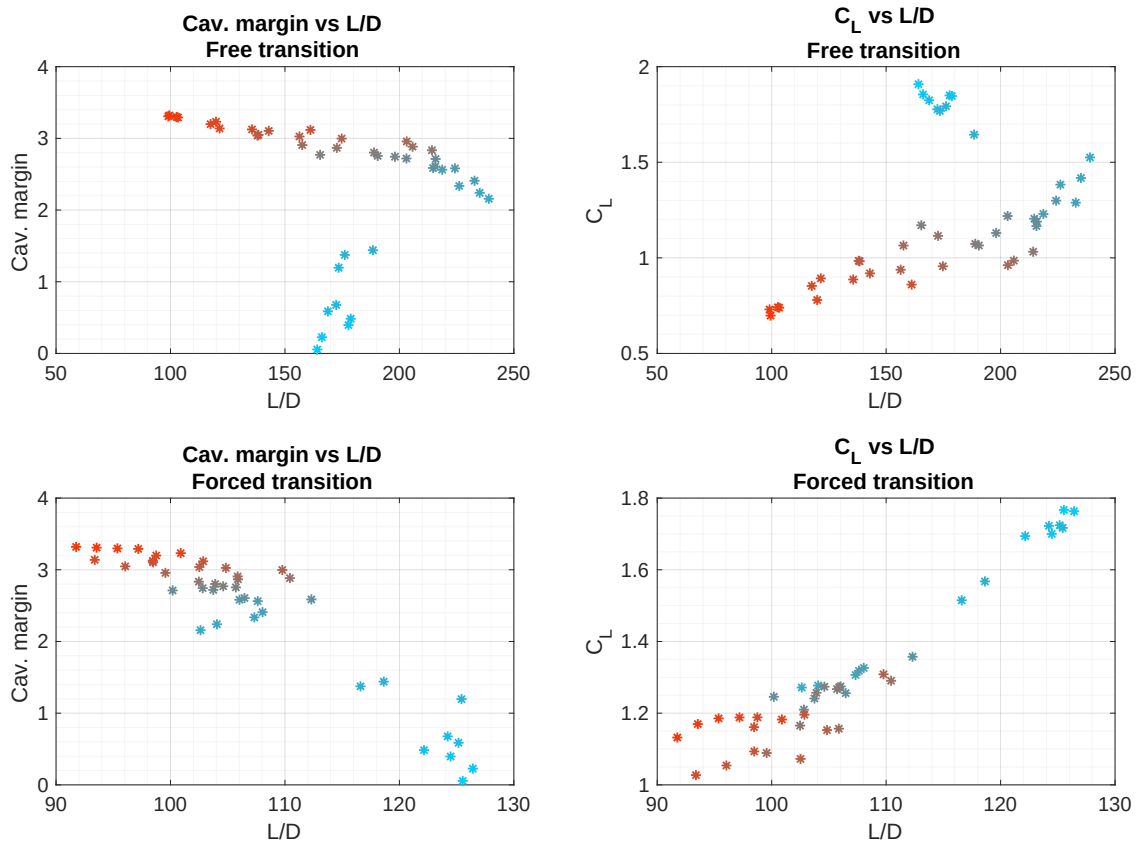

Figure 4.13: Version FIVE C of CF1 - Comparison of free (natural) and forced transition regimes with various distributions

with a larger CF1 value than another does not necessarily mean that it performs better for free (natural) transition or forced transition alone. What it means is that the overall performance, weighted between maximum L/D as well as optimum C_L, for both regimes, is higher. For example, hydrofoil 1 could have lower L/D in the clean regime than hydrofoil 2, but still have a higher CF1 value because hydrofoil 2 has lower L/D in the rough regime as well as optimum C_L for both regimes.

4.6 Other simulations - Increased angle of attack variation

In this section, a specific simulation is described, regarding the case of large AOA variation during turbine blade rotation, which may happen for off-design operating conditions of the turbine.

In figure 3.8 it is possible to notice that in design conditions the variation in angle of attack induced by the azimuthal rotation of the blades is lower than 2 degrees, even at the tip. Thus, it is of interest to observe how hydrofoils would be influenced by an increased variation of angle of attack which can, for example, be caused by yaw misalignment with the main flow direction.

This study is performed using CF1 version FIVE C, and an angle of attack variation of 5 degrees.

However, due to the fact that the objective is to study the influence of a different variable than in the previous sections, this case is named optimization SIX C. The results can be seen in figures 4.14 and 4.15. The Reynolds number is $1{\cdot}10^7$, the section considered is r/R = 75% and maximum thickness is specified as t/c = 15%.

It is possible to observe in figure 4.14 that the hydrofoils obtained are very similar to the ones resulting from version FIVE C and TWO B. Despite the similarity, version SIX C foils have maximum thickness at an earlier point, predominantly before $x/c \leq$ 25%, while versions FIVE C and TWO B have the maximum thickness predominantly after this chord-wise location.

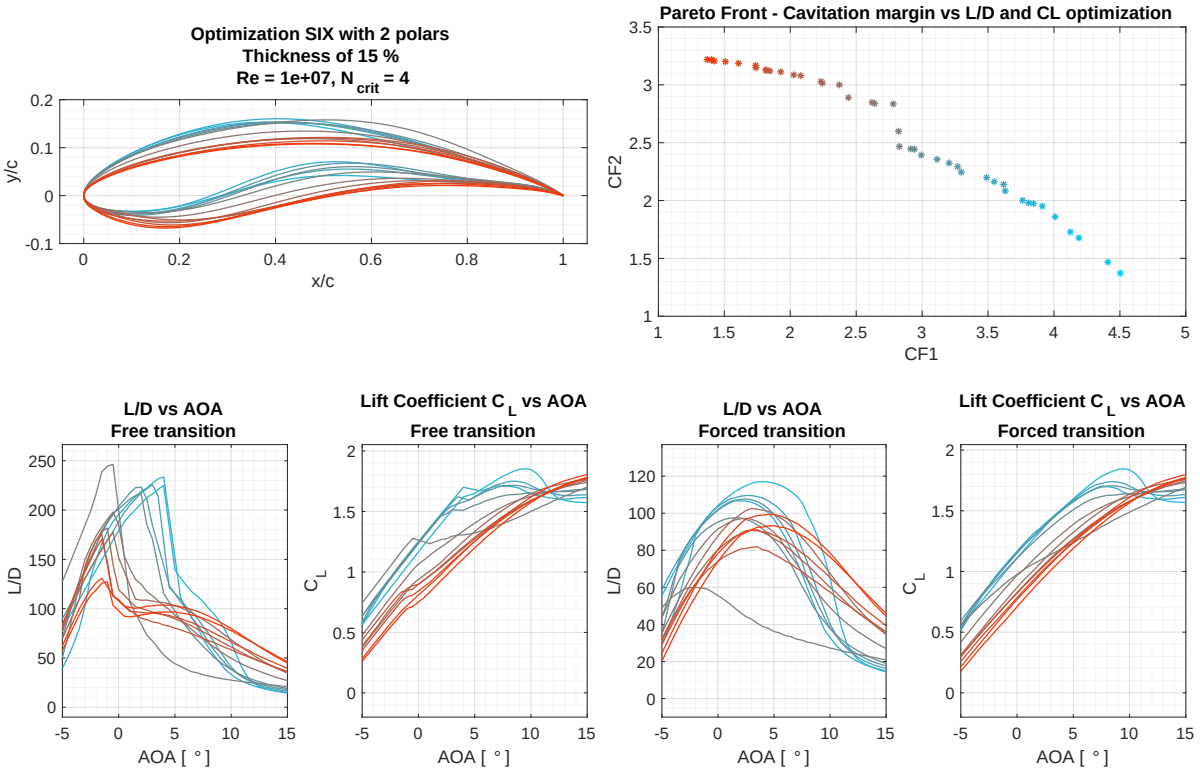

Figure 4.14: Foils, Pareto front and L/D obtained with CF1 SIX C

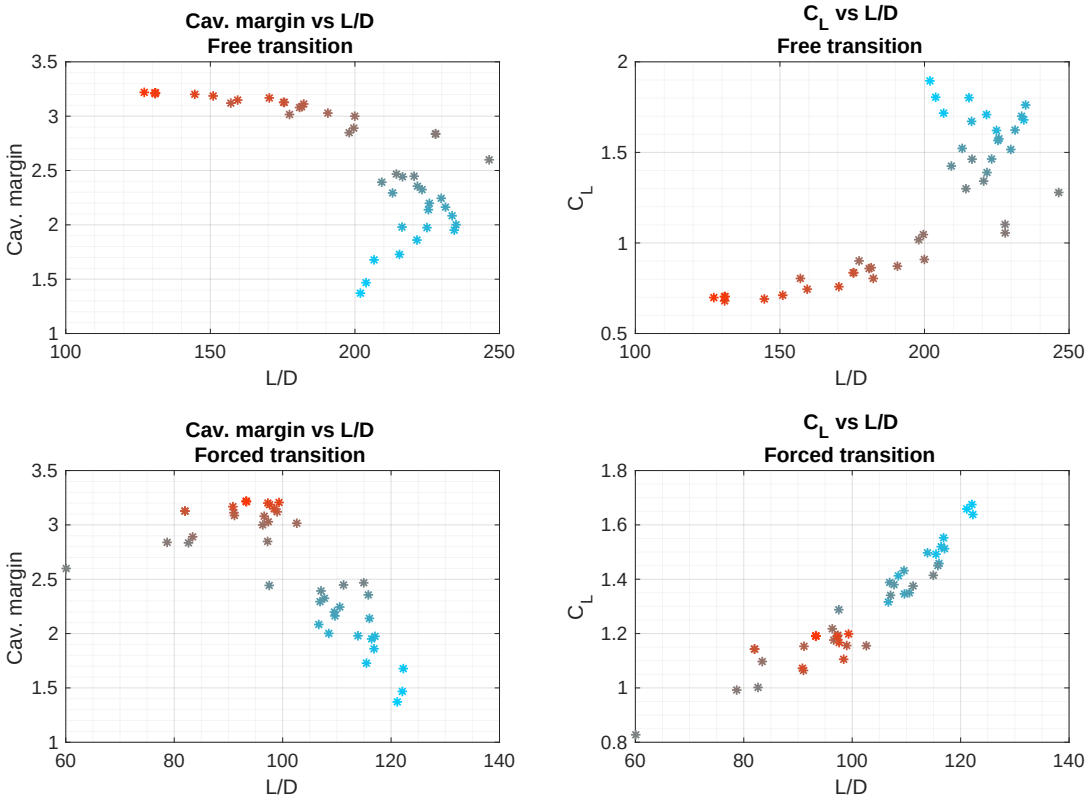

Figure 4.15: Version SIX C of CF1 - Comparison of free (natural) and forced transition regimes with various distributions

Chapter 5

Hydrofoil optimization results

In this chapter the final results for each blade section are presented. The optimization routine outputs an average of 43 hydrofoils per simulation. When obtaining these results, the Reynolds number is corrected for each section in study according to table 3.3. The thickness distribution along the blade span follows the example of the Bahaj *et.al* turbine in [19], and is presented in table 3.3.

For each section and thickness, three images are presented:

- 1st: Image with 5 plots presenting 15 foils selected from the Pareto front, along with the respective L/D curve and C_L polar for free and forced transition; Pareto front with CF1 and CF2 scores for all the hydrofoils resulting from the simulation;
- 2nd: Image with 4 plots presenting, for all the hydrofoils resulting from the simulation, the cavitation margin vs L/D ratio and C_L vs L/D for both regimes ;
- 3rd and final: comparison between scores of CF1 and CF2 for optimized hydrofoils and reference hydrofoils (NACA 66-8XX and NACA 63-8XX series).

The comparison presented in the last figure is made by calculating the performance of the reference foils using CF1 and CF2, which means a score is attributed in the same manner for reference foils as it is for the optimized or Pareto efficient foils. In this way, the comparison is direct.

5.1 Section $\mathrm{r/R}$ = 20% , thickness $\mathrm{t/c}$ = 24%

The section at the root of the blades has the greatest thickness (see table 3.3) for structural reasons [57][21]. It is chosen as 24% following the examples of Bahaj *et.al* [19] and Goundar *et.al* [21].

The results for this thickness can be seen in figures 5.1 and 5.2. The Reynolds number at this section is of $3.9{\cdot}10^6$. The cavitation margin is very high as this is the section that is at greatest depth when Ψ = 0° (see figure 1.4), having a span of $\approx$ 2.8 between the highest and lowest values. Also, the effective velocity is the lowest at this r/R (see figure 3.10).

One can notice how the maximum thickness point of the hydrofoils is displaced from $x/c \approx$ 30% in foils with higher cavitation margin to 10% for foils with higher hydrodynamic performance.

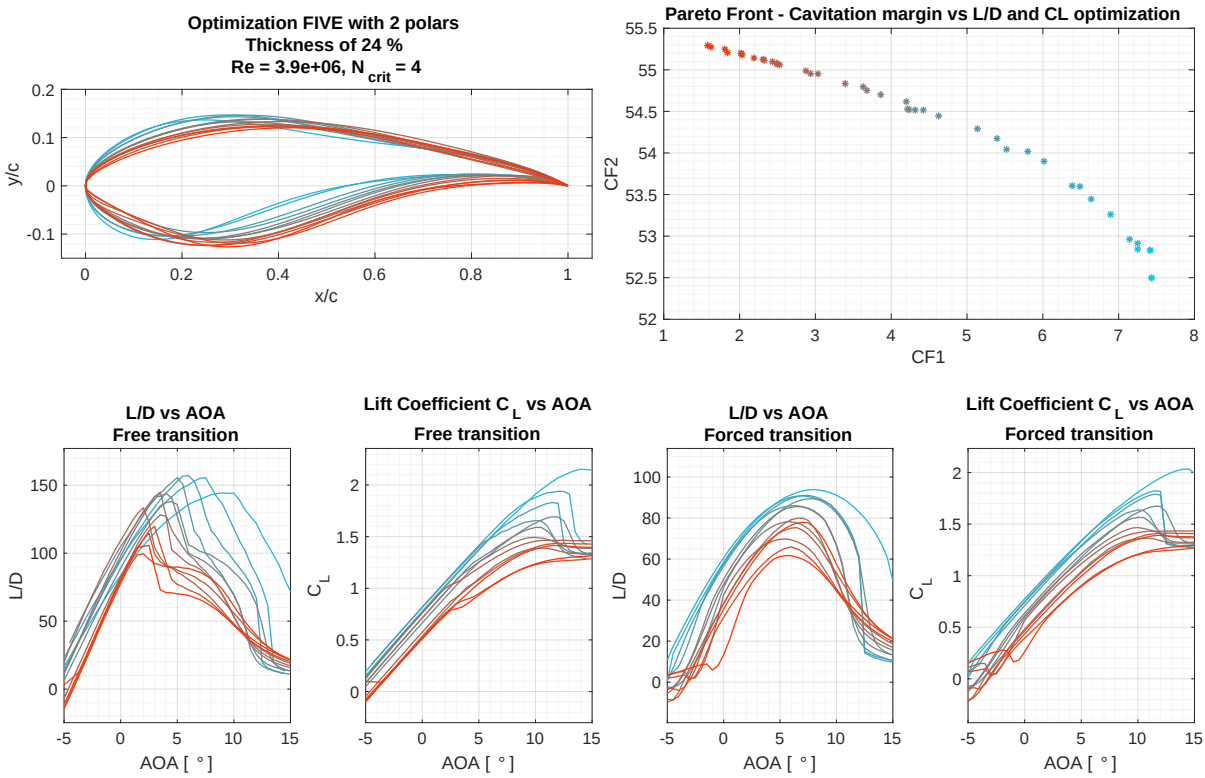

Figure 5.1: Foils, Pareto front and L/D obtained with CF1 FIVE C for hydrofoils of thickness t/c = 24%

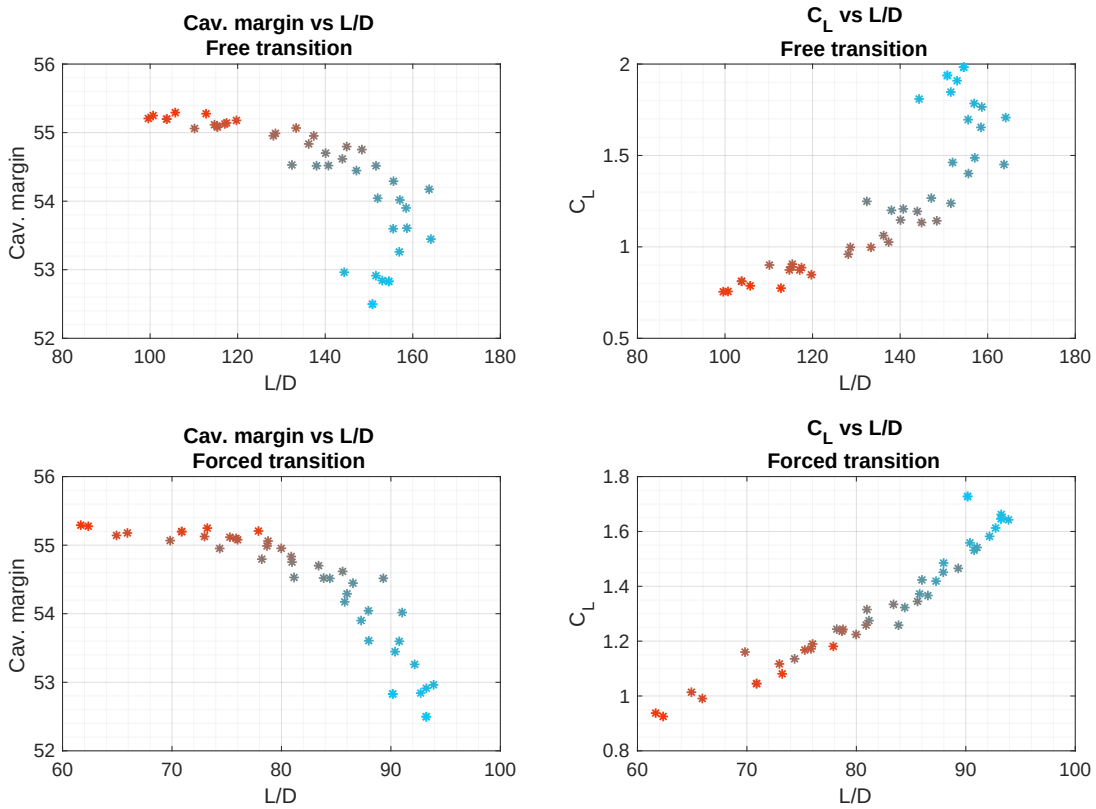

Figure 5.2: Thickness of 24% - Comparison of free and forced transition regimes with various distributions

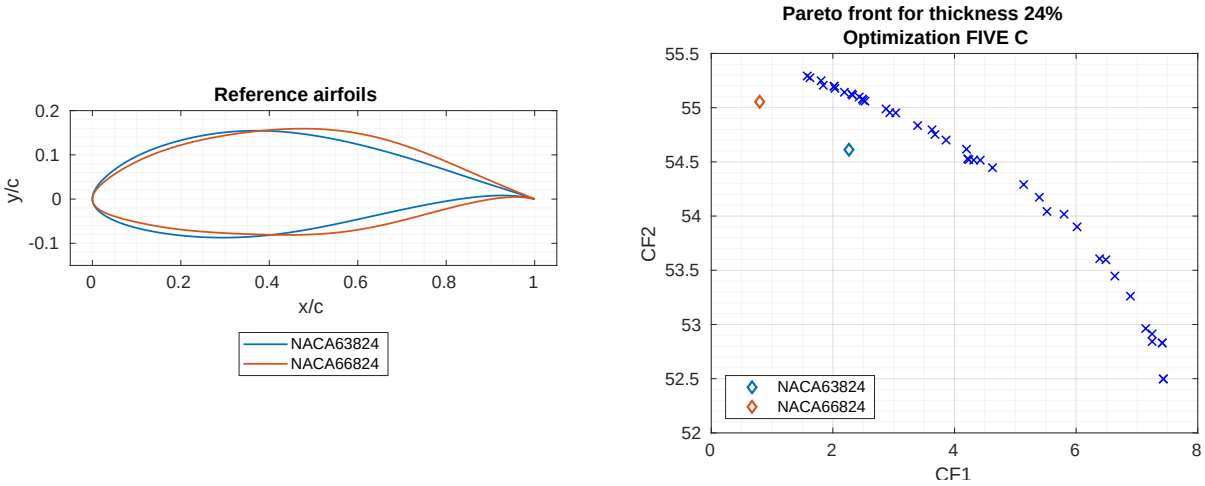

Figure 5.3: Thickness of 24% - Comparison with reference hydrofoils, thickness of 24%

In figure 5.3 it is clearly possible to appreciate the improvement relative to the reference foils considered. One can observe that, for this thickness and for a number of foils, not only the hydrodynamic performance is increased but the cavitation margin as well. Not only that, there are 30 different hydrofoils that, for this target thickness, Reynolds number and N_{crit} value, outperform the reference foils in terms of hydrodynamic performance.

Going into more detail, the optimized hydrofoils exhibit, for the same cavitation margin as for the NACA 63-824, increases of 73.21% and 99.82% in maximum L/D and C_L, respectively, for the rough regime.The same optimized hydrofoil improves the clean regime performance by 4.81% in maximum L/D and 4.01% in optimum C_L.

5.2 Section $\mathrm{r/R}$ = 30% , thickness $\mathrm{t/c}$ = 21%

At r/R = 30 % the maximum blade thickness of the reference turbine is of 21% of the chord. Optimization FIVE C for this section yields the results presented in figures 5.4 and 5.5. The Reynolds number at this section is of $4.5{\cdot}10^6$. Cavitation margin is still very high as this section is also at great depth when Ψ = 0° and experiences low effective flow speed - see figures 3.8 and 3.10.

Similarly to the previous section, it is possible to observe a displacement in the maximum thickness, occurring at an earlier chord-wise location for this section. The difference, however is not as notorious as for t/c = 24% due to the shorter span of CF2 scores (1.8 for this section).

Again, there are a large number of optimized hydrofoils which outperform the references in both cavitation margin and hydrodynamic performance, as it is possible to see in figure 5.6. Comparing with NACA 63-821 for the same cavitation margin, the optimized hydrofoil displays improvements of 12.35% and 11.76% in maximum L/D and optimum C_L, respectively, with clean transition. The same hydrofoil displays improvements of 34.56% in maximum L/D and 49.19% in optimum C_L with forced transition.

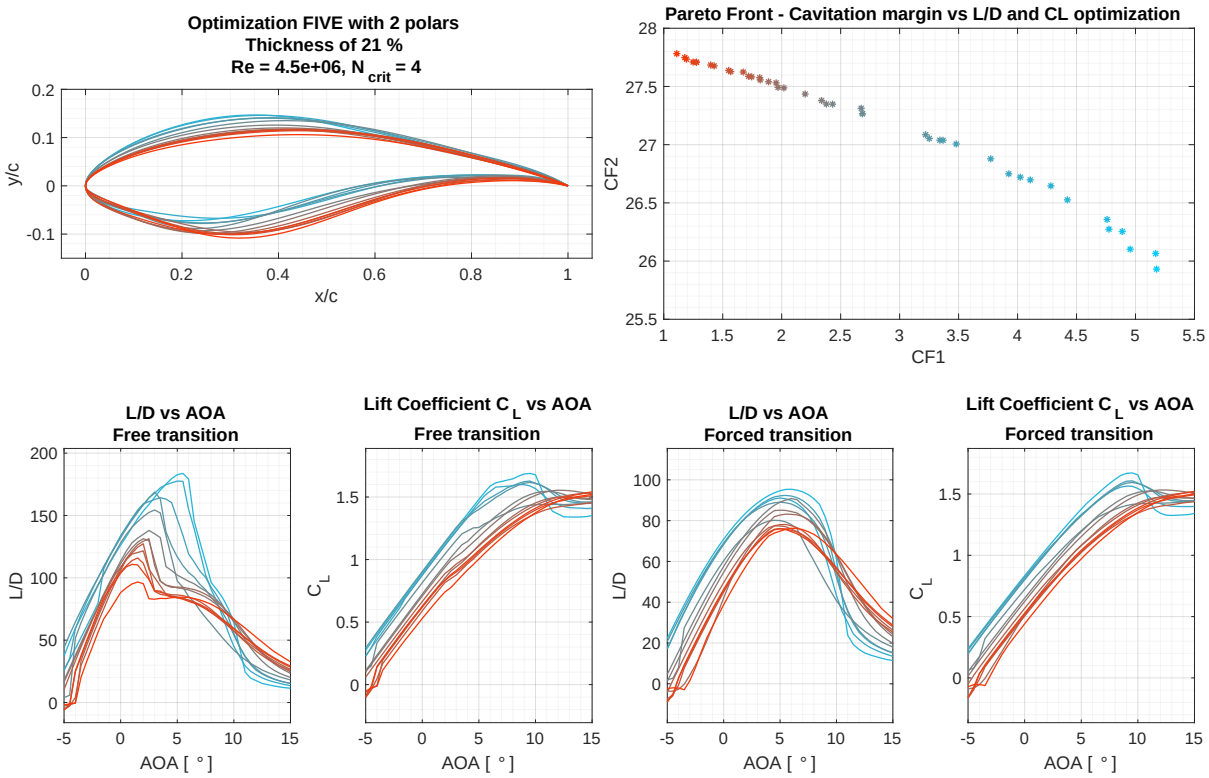

Figure 5.4: Foils, Pareto front and L/D obtained with CF1 FIVE C for hydrofoils of thickness t/c = 21%

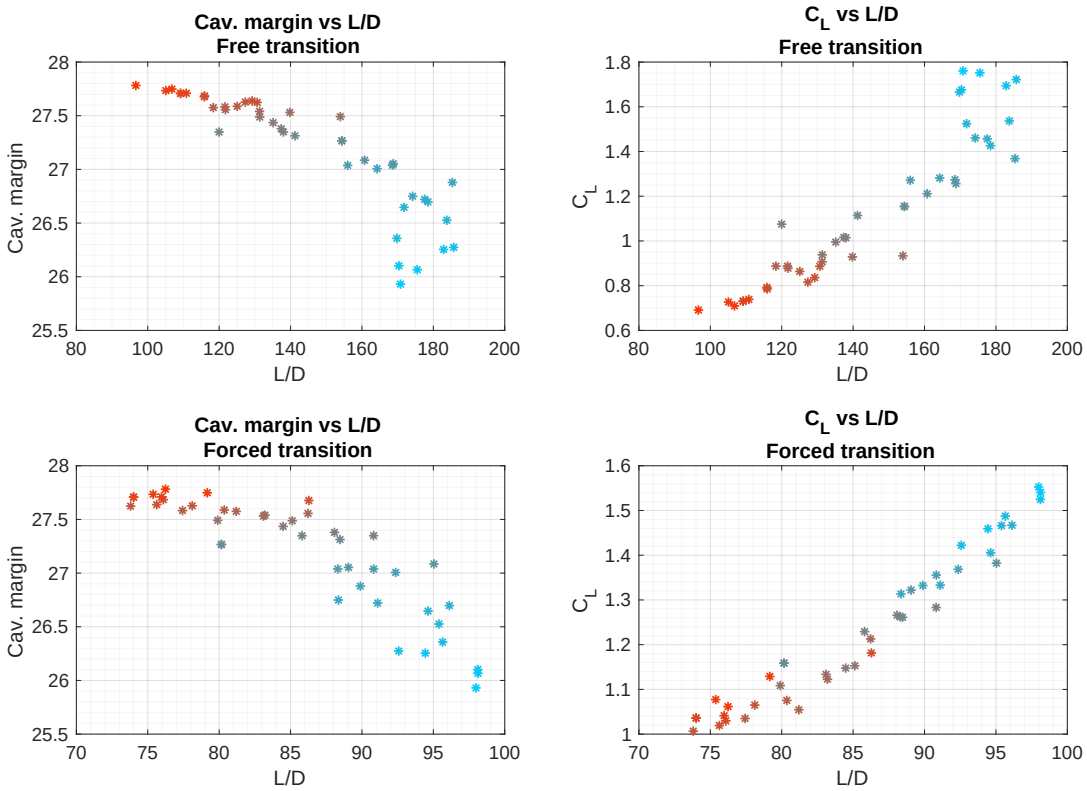

Figure 5.5: Thickness of 21% - Comparison of free and forced transition regimes with various distributions

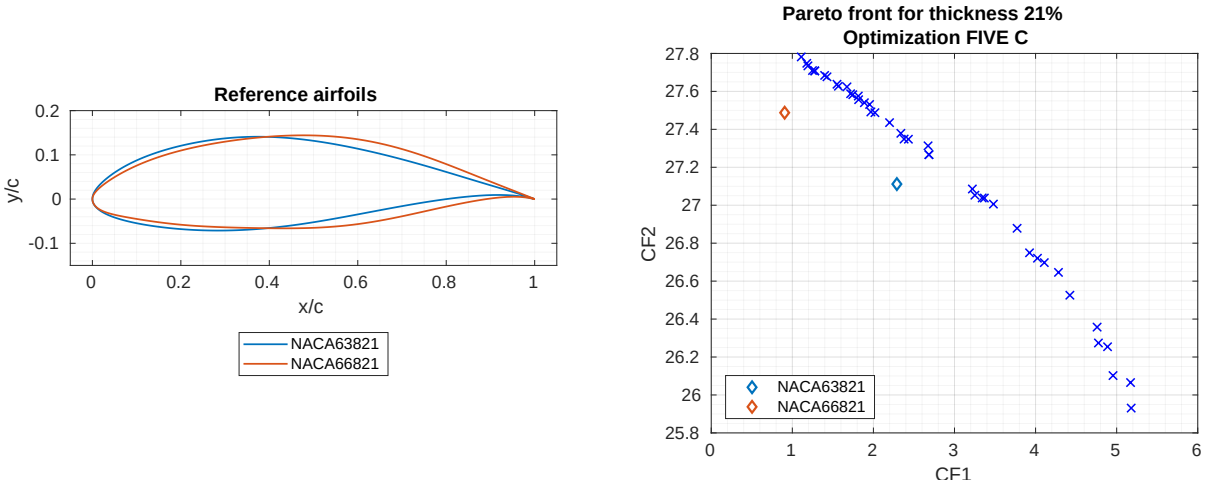

Figure 5.6: Thickness of 21% - Comparison with reference hydrofoils

5.3 Section r/R = 45% , thickness t/c = 18%

At r/R = 45 %, almost half the span of the reference turbine blades, the maximum foil thickness is 18% of the chord. Optimization FIVE C renders the results presented in figures 5.7 and 5.8 for this section. The Reynolds number is $5.3{\cdot}10^6$. The value of CF2, cavitation margin, starts to achieve lower values as this section is at a lower depth when Ψ = 0° and experiences higher effective flow speed than the previous sections.

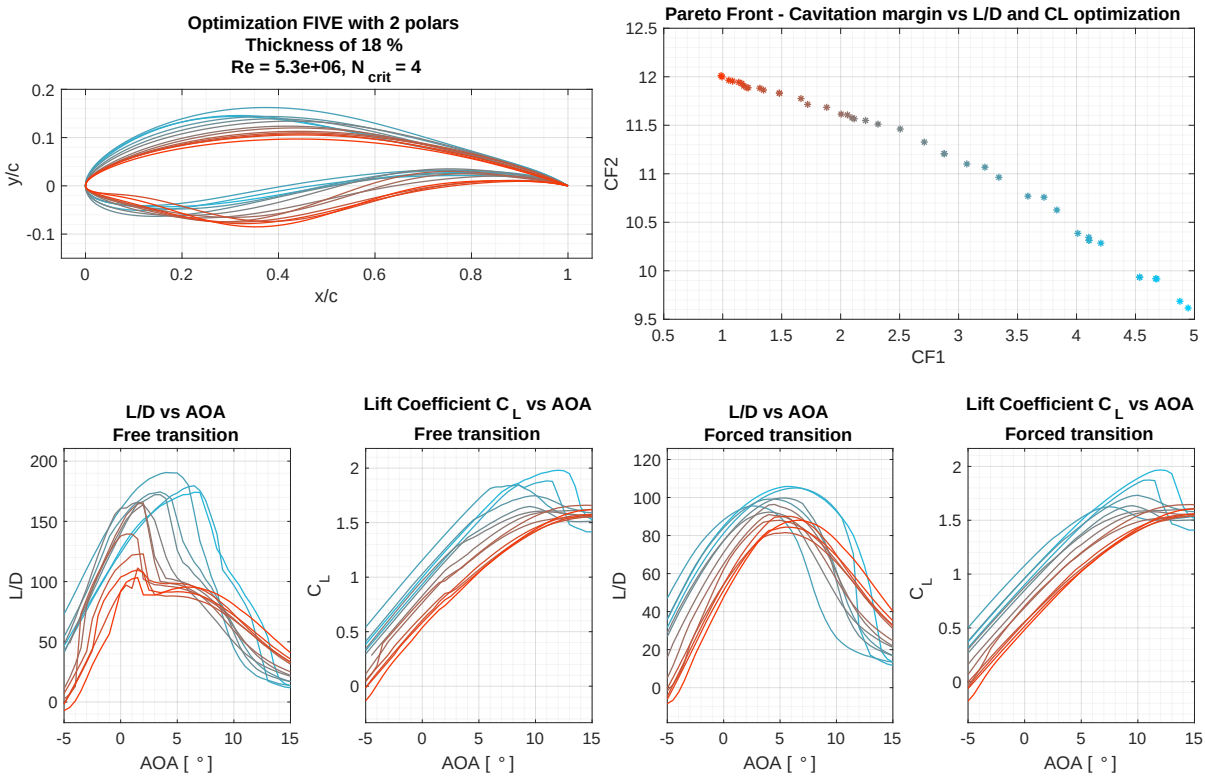

Figure 5.7: Foils, Pareto front and L/D obtained with CF1 FIVE C for hydrofoils of thickness t/c = 18%

In the results for this thickness it is possible to see a greater variety of hydrofoil shapes. This comes

due to the fact that at lower maximum thickness it is possible to attain higher values of C_L and L/D, and the optimization routine reaches this goal while also maintaining a high cavitation margin; also, as for t/c = 24%, there is a span of 2.6 in CF2 scores, allowing for greater heterogeneity of geometries.

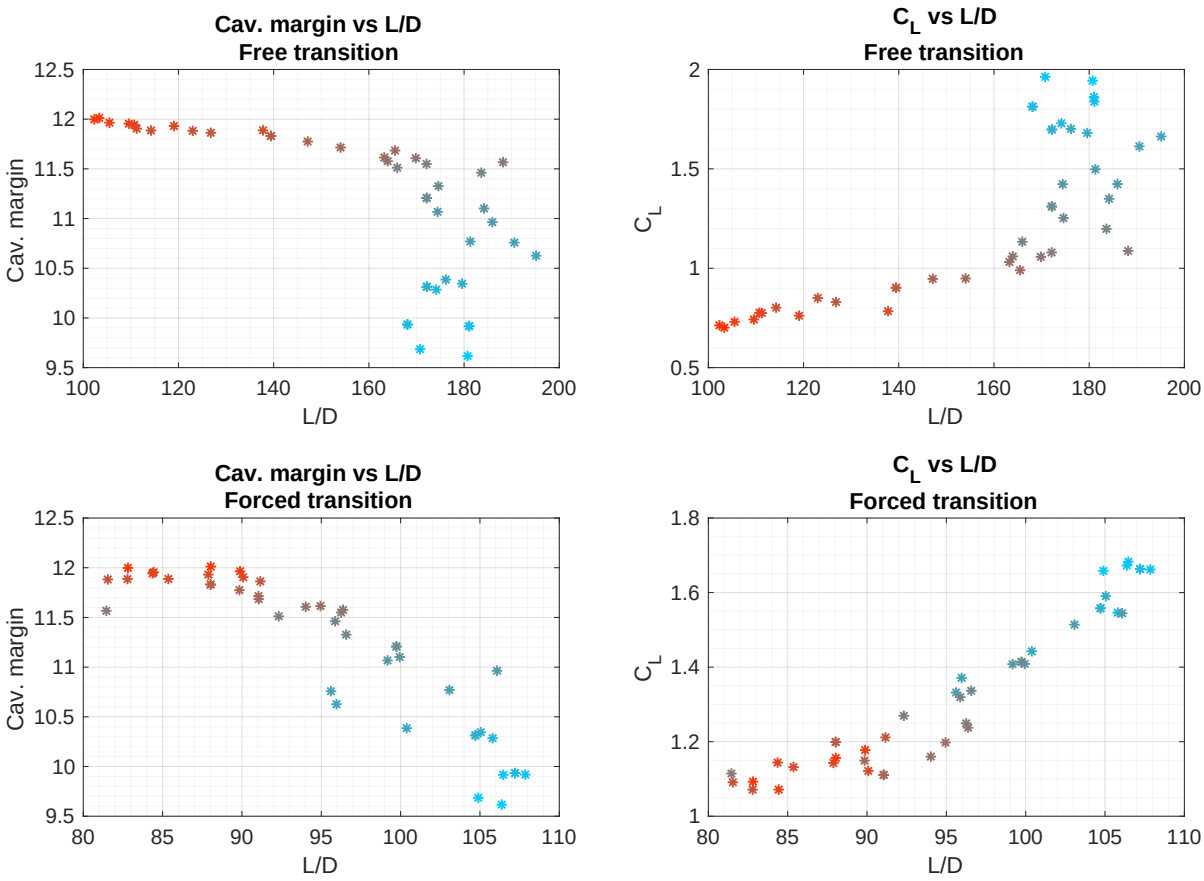

Figure 5.8: Thickness of 18% - Comparison of free and forced transition regimes with various distributions

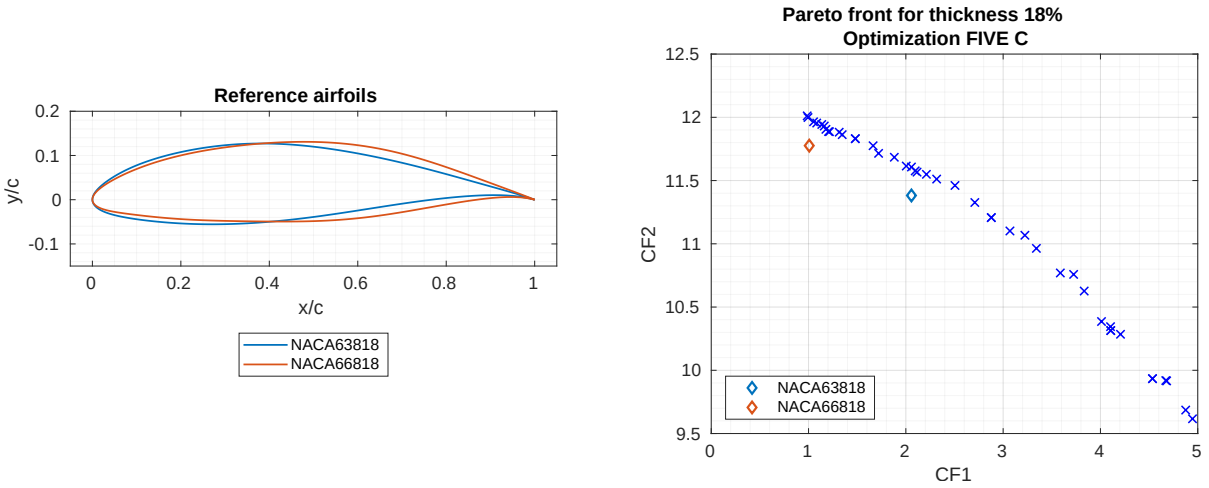

Figure 5.9: Thickness of 18% - Comparison with reference hydrofoils

In figure 5.9 it is possible to observe that, again, the reference foils have been surpassed, although for this target thickness and section the improvement is not as large as seen previously; despite this, for

the same cavitation margin as displays the NACA 63-818, the optimized hydrofoil displays improvements of 28.97% in maximum L/D and 10.17% in optimum C_L for the clean regime, and of 7.20% in maximum L/D and 17.64% in C_L for the rough regime.

5.4 Section $\mathrm{r/R}$ = 75% , thickness $\mathrm{t/c}$ = 15%

At r/R = 75 % the maximum blade thickness is 15% of the chord. Optimization FIVE C renders the results presented in figures 5.10 and 5.11 for this section. The Reynolds number is 5.5·10^6. At this section, the cavitation margin approaches zero as the value of CF1 reaches its maximum.

Comparing with the foils obtained for t/c = 18% there is an even greater variation of hydrofoil shapes. The shapes obtained at CF1 $\approx$ 4.5 show much greater camber than the ones with greater cavitation margin, while the latter possess a sharper leading edge, which is the same tendency observed for t/c = 18%. There is also a more noticeable displacement of the maximum thickness position to an earlier chord-wise location as the cavitation margin increases. This large variety in hydrofoil shapes is due to the also large spans in CF1 and CF2 values, 3 and 4, respectively.

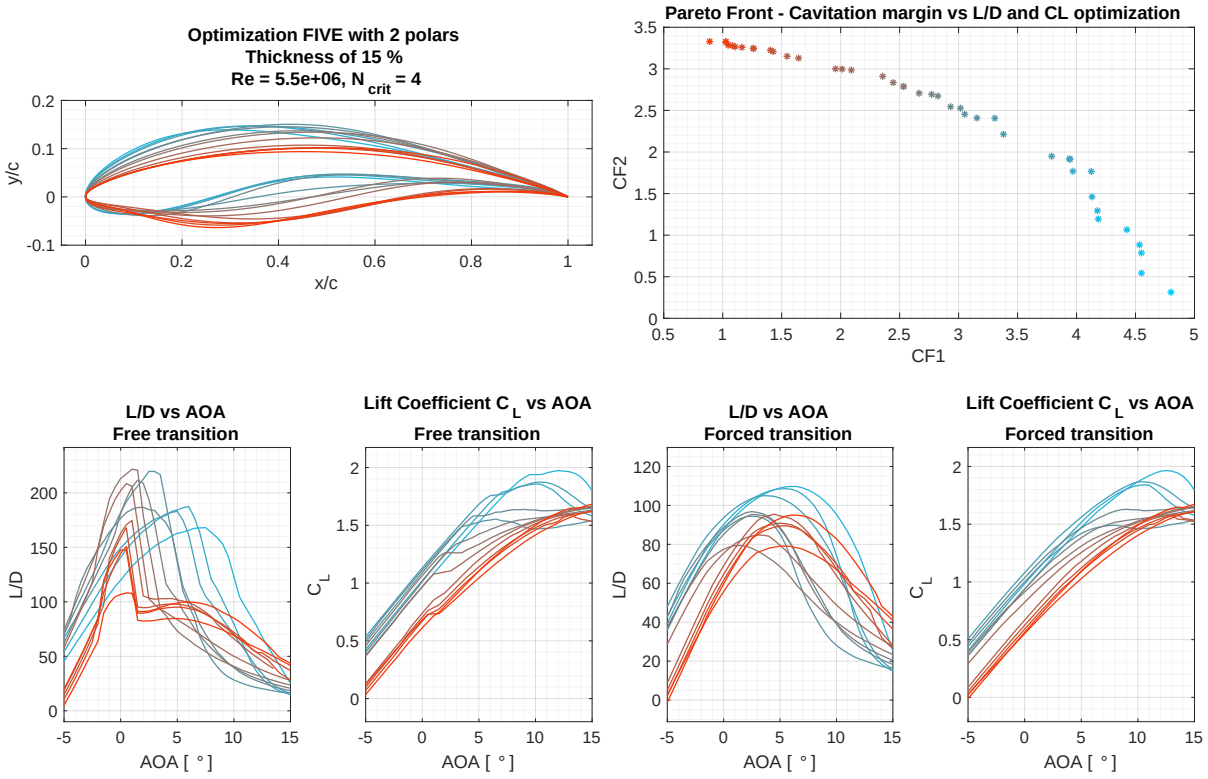

Figure 5.10: Foils, Pareto front and L/D obtained with CF1 FIVE C for hydrofoils of thickness t/c = 15%

As can be seen on figure 5.12, the reference hydrofoils are again outperformed but the margin is straightened when compared to previous sections. For the same cavitation margin as the reference foil NACA 63-815, the optimized hydrofoil displays increases in maximum L/D and optimum C_L of 66.10% and 20.98% for the clean regime and an increase in optimum C_L of 0.90% in rough regime; this foil also shows a decrease in maximum L/D of 23.48% for the rough regime.

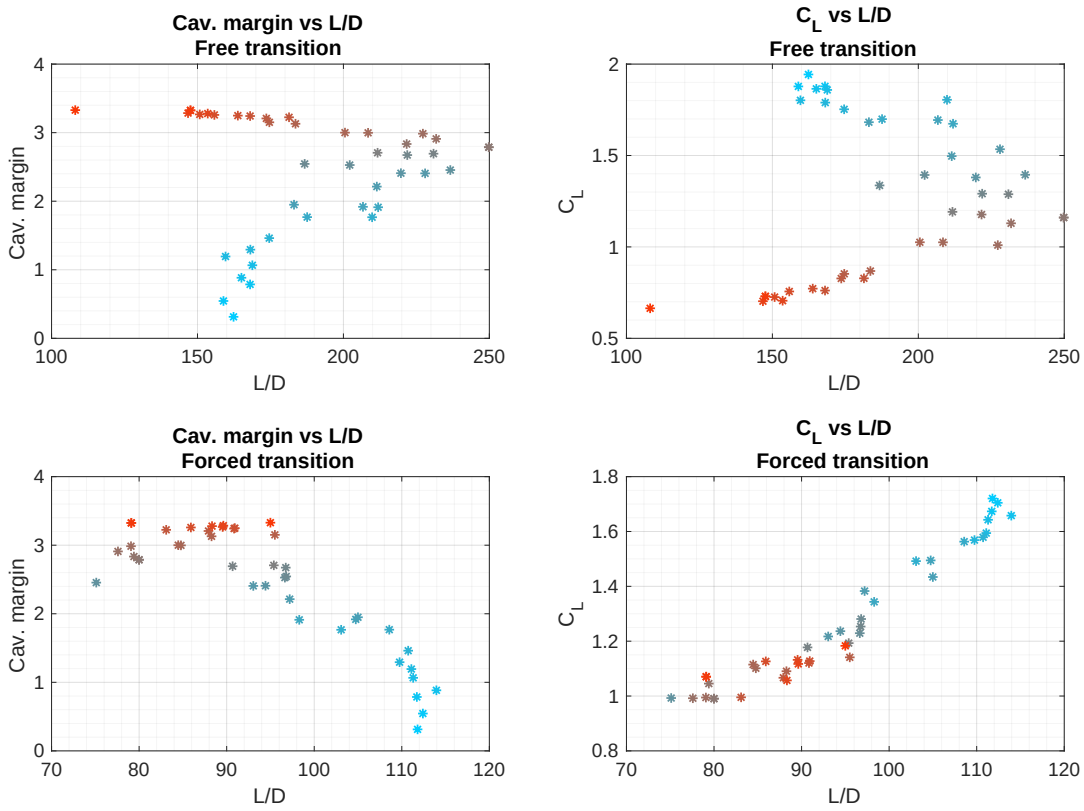

Figure 5.11: Thickness of 15% - Comparison of free and forced transition regimes with various distributions

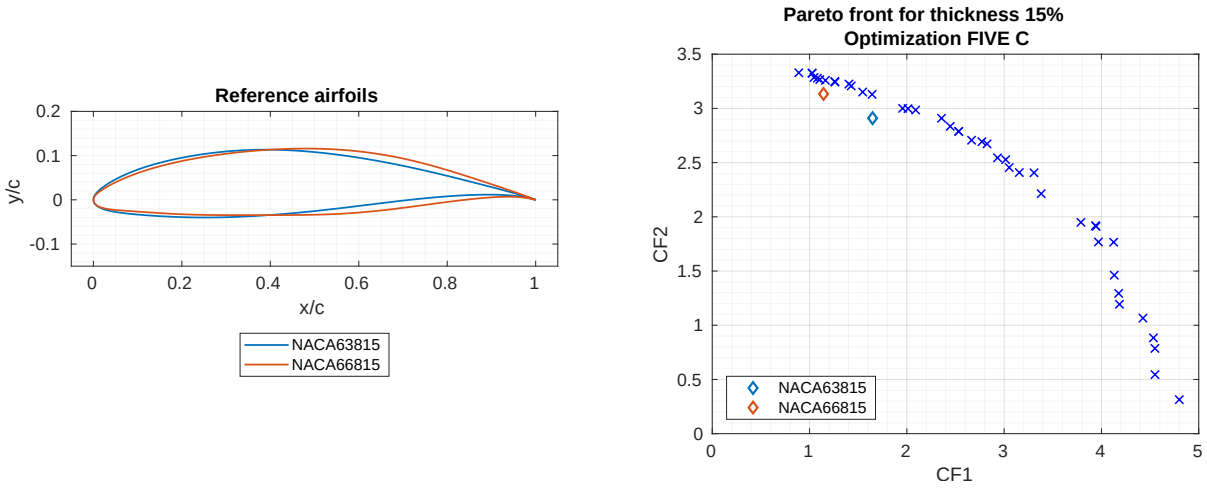

Figure 5.12: Thickness of 15% - Comparison with reference hydrofoils

5.5 Section $r/R \approx$ 100% , thickness t/c = 12%

At $r/R \approx$ 100% i.e., the last section present on the reference turbine blades, the maximum blade thickness is 12% of the chord. Optimization FIVE C renders the results presented in figures 5.13 and 5.14 for this section. The Reynolds number is $5.2 \cdot 10^6$.

At this section, for the present rotor and turbine design conditions (see table 3.2) the cavitation margin range of values is comprehensively short (1.1), this being the section that is most susceptible to cavitation, reaching the shortest depth when $\Psi = 0°$ and highest V_{eff} (see figure 3.10). Despite this

fact, it is still possible to obtain good values of cavitation margin (CF2 $\geq$ 1).

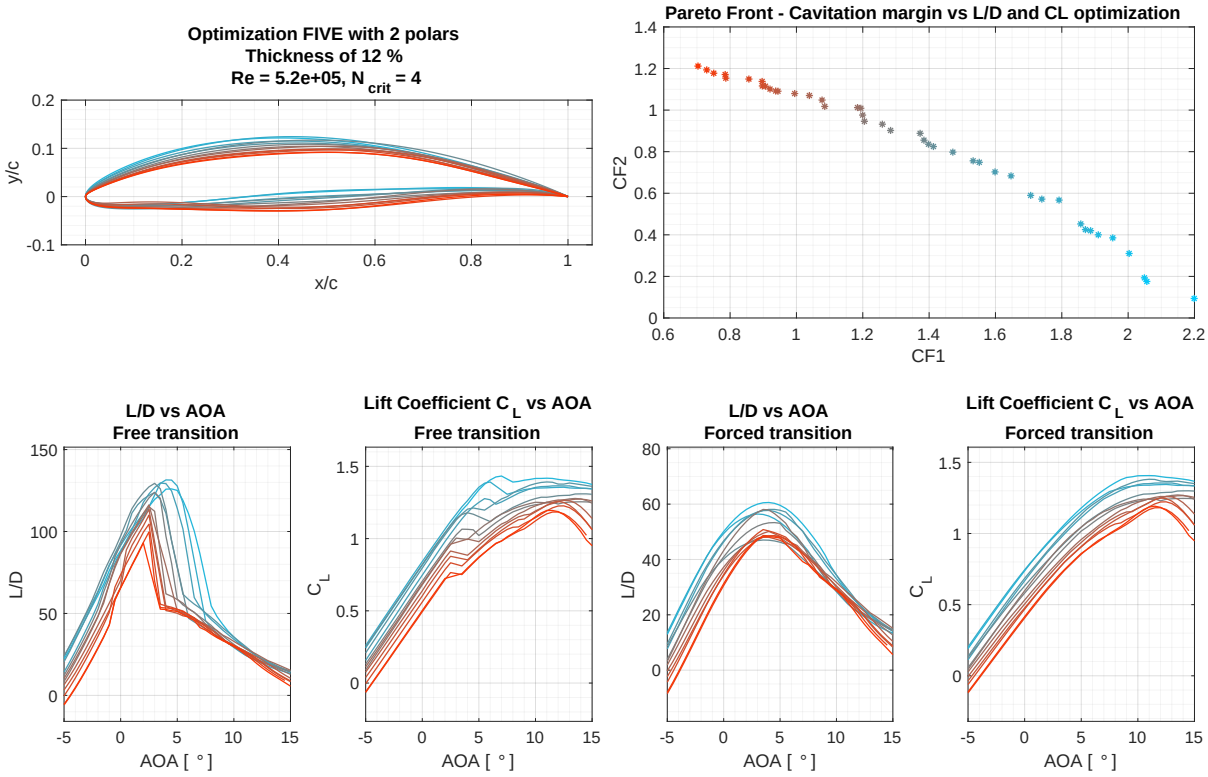

Figure 5.13: Foils, Pareto front and L/D obtained with CF1 FIVE C for hydrofoils of thickness t/c = 12%

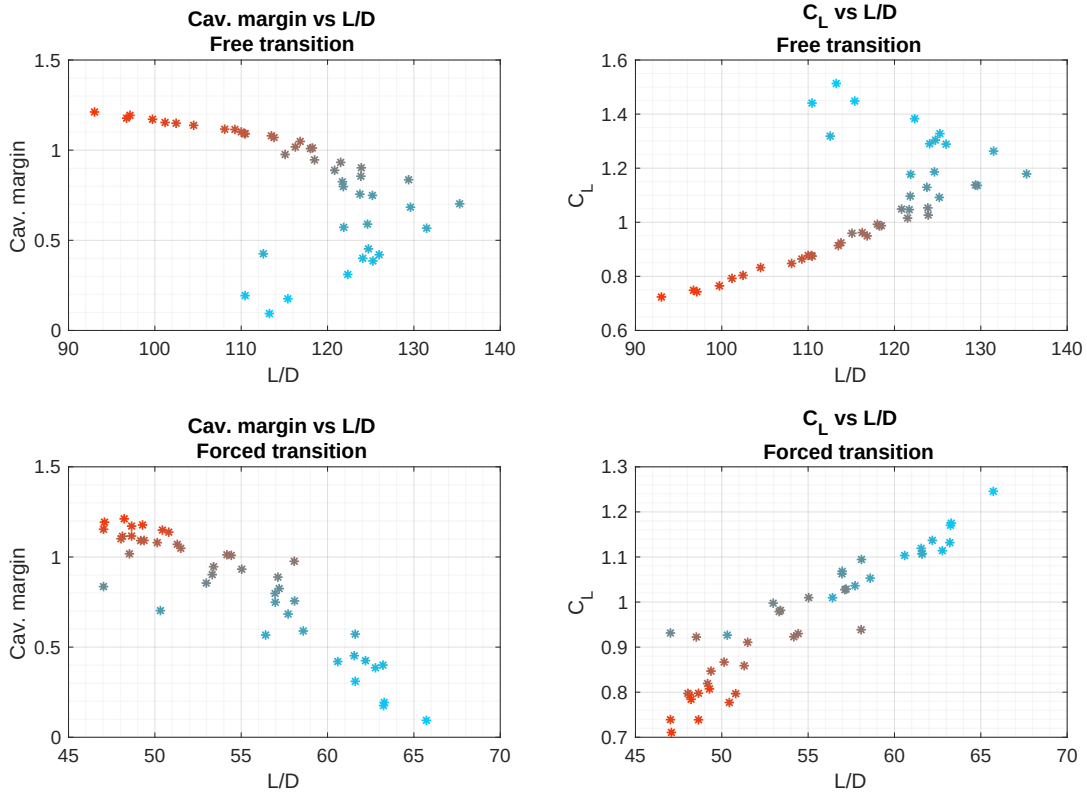

Figure 5.14: Thickness of 12%, optimization FIVE C - Comparison of free and forced transition regimes with various distributions

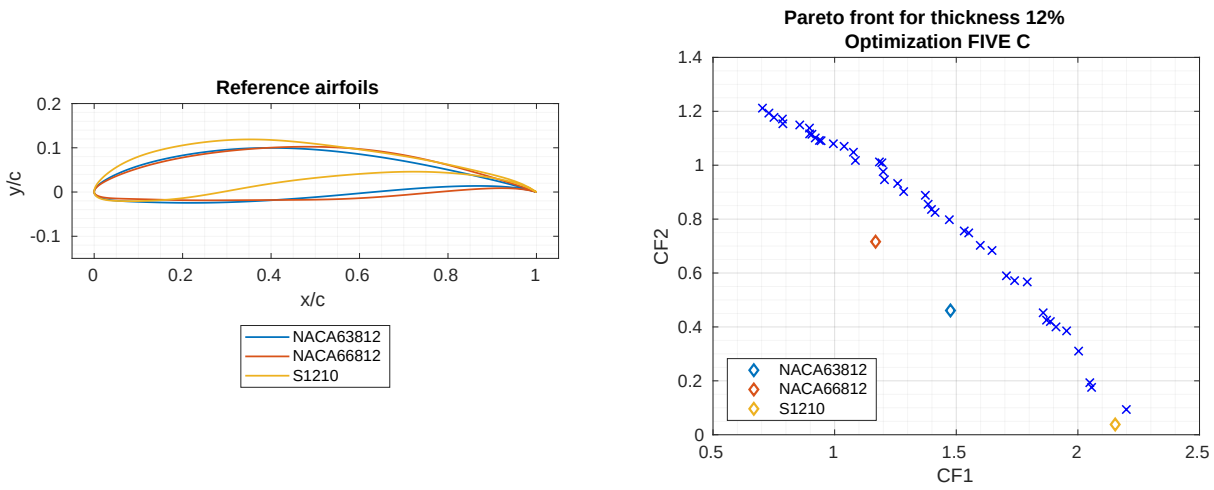

Figure 5.15: Thickness of 12% - Comparison with reference hydrofoils

As we can see in figure 5.13, there is not a great variety in hydrofoil geometry. This is due to the short cavitation margin range previously mentioned: larger spans of CF1 and CF2 would render a greater heterogeneity of hydrofoil geometries, as seen for previous sections.

Regarding the performance relative to the reference hydrofoils, it is possible to see in figure 5.15 that, again, several improved hydrofoils are obtained. For the same cavitation margin as NACA 63-812, the corresponding optimized hydrofoil shows an increase in 13.14% in maximum L/D and 23.06% in optimum C_L for the clean regime, and an improvement in optimum C_L of 9.95% for the rough regime, while also showing a decrease of 6.09% in maximum L/D in the rough regime.

Reference hydrofoil S1210 is outperformed both in CF1 and CF2 by only one hydrofoil, but both have very low cavitation margin. This optimized hydrofoil shows improvements of 7.51% and 6.89% in maximum L/D and optimum C_L, respectively, for the clean regime, and an increase of 2.11% in C_L for the rough regime; also, there is a decrease of 6.85% in maximum L/D for the rough regime.

Due to the short spans in values of CF1 and CF2, an effort was made to further increase these values, namely, obtain hydrofoils with better overall performance (higher CF1) for the same values of cavitation margin, and then increase both values, CF1 and CF2. These efforts are detailed in the subsequent sections.

5.5.1 Optimization SEVEN C for section $\mathrm{r/R} \approx$ 100% , thickness $\mathrm{t/c}$ = 12%

The cost function employed for this optimization follows the line of thought of formulation 4.10, of CF1 version FIVE C. The square factor is substituted by a cube, in order to further increase the value of CF1 to the detriment of CF2. The results for this optimization can be seen in figures 5.16 and 5.16.

$$\mathbf{C_{L\ new\ foil}^{adim}} = \left(\frac{\mathbf{C_{L\ new\ foil}^{weighted}} - \mathbf{C_L^{ref}}}{\mathbf{C_L^{ref}}} + \mathbf{1} \right)^{\mathbf{3}} \qquad \mathbf{L/D_{new\ foil}^{adim}} = \left(\frac{\mathbf{L/D_{new\ foil}^{weighted}} - \mathbf{L/D^{ref}}}{\mathbf{L/D^{ref}}} + \mathbf{1} \right)^{\mathbf{3}} \tag{5.1}$$

An additional condition is added: optimum C_L must be higher than 0.8, in order to promote higher L/D values.

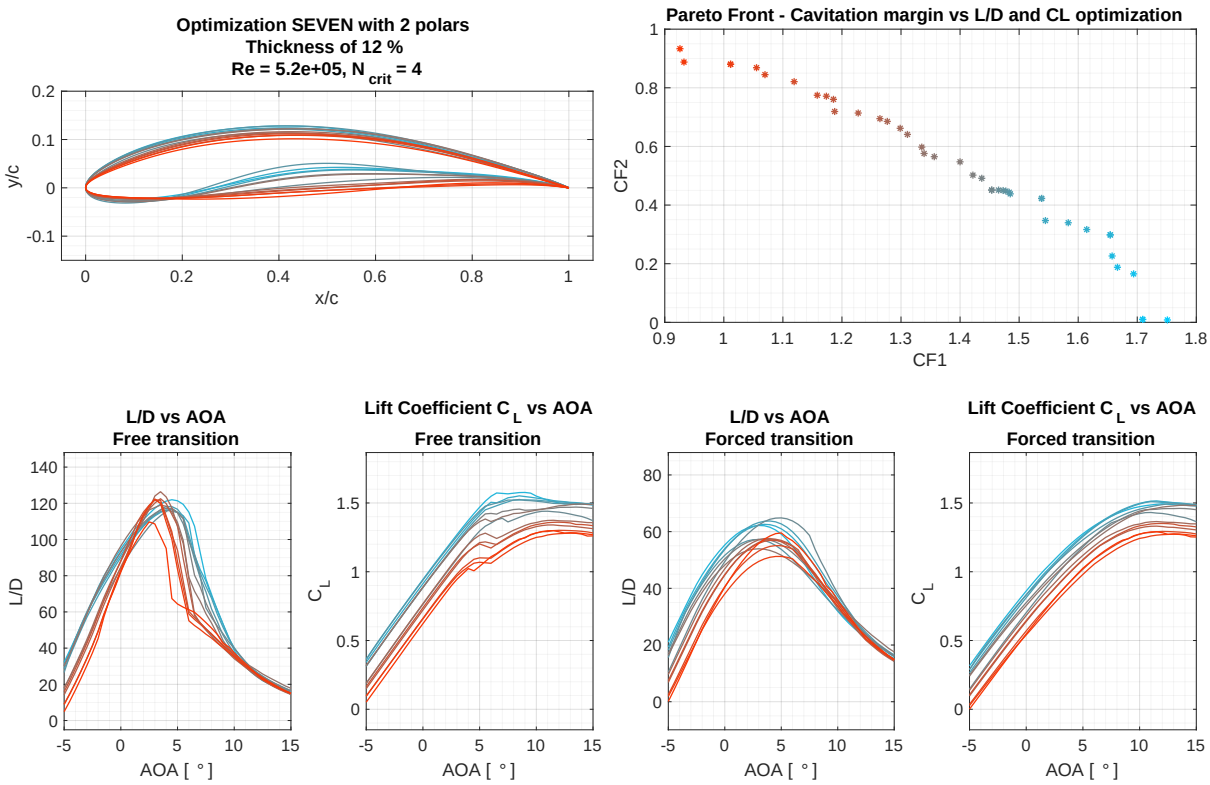

Figure 5.16: Foils, Pareto front and L/D obtained with CF1 SEVEN C for hydrofoils of thickness t/c = 12%

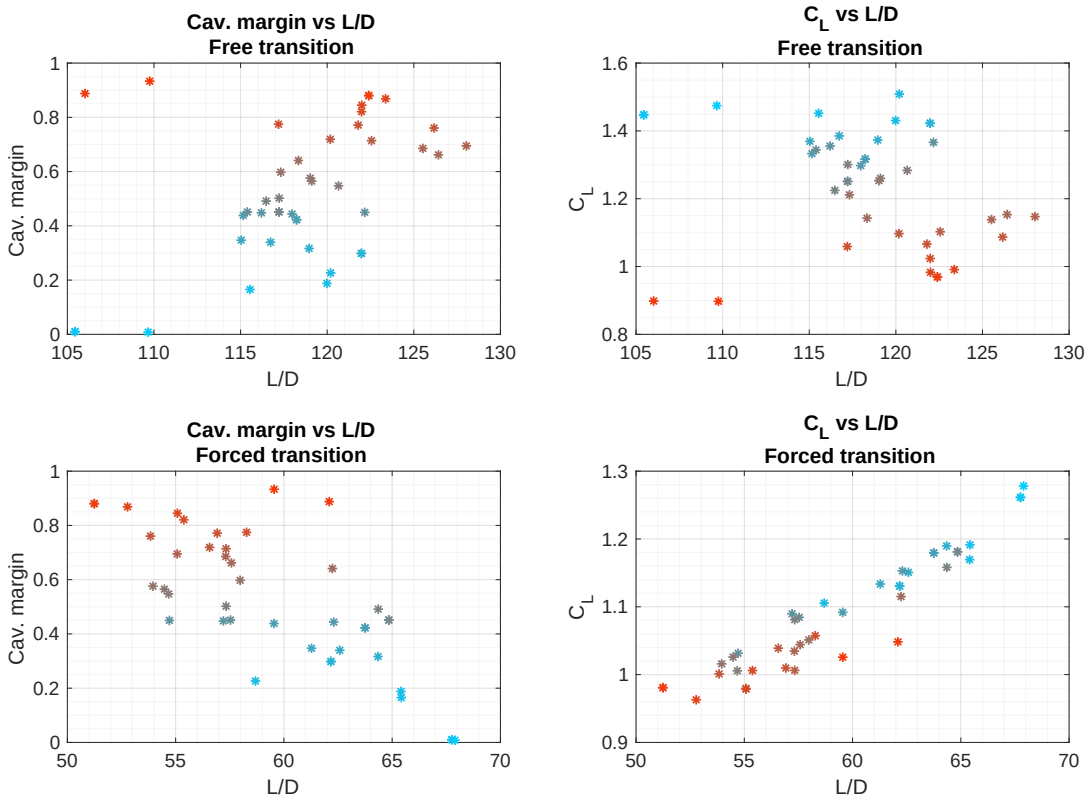

Figure 5.17: Thickness of 12%, optimization SEVEN C - Comparison of free and forced transition regimes with various distributions

Although there is no increase in the spans of CF1 and CF2, it is possible to notice that there is a much larger variety of hydrofoil geometries. Namely, the hydrofoils which display higher value of CF1 are much more cambered than the ones resulting from CF1 version FIVE C, and, again, there is a displacement of the maximum thickness chord-wise location to an earlier position.

5.5.2 Optimization EIGHT C for section $\mathrm{r/R} \approx$ 100% , thickness $\mathrm{t/c}$ = 12%

For optimization EIGHT C, CF1 was maintained as in formulation 5.1 and CF2 was changed in the following manner:

$$\mathbf{CF2} = \left(\left(\sigma_{\mathbf{min}}^{\mathbf{r/R}} - (-\mathbf{C}_{\mathbf{p_{min}}})_{\mathbf{max}}\right) + \mathbf{1}\right)^{\mathbf{3}} \tag{5.2}$$

The objective of formulation 5.2 is to grant the optimization routine extra sensibility when attributing and testing the values of CF2, allowing it, in theory, to further explore the design space and extend the range of CF1 and CF2. The condition that minimum optimum C_L be higher than 0.8 is maintained.

The results for this optimization can be seen in figures 5.18 and 5.19.

Yet again, there is a change in the position of the maximum thickness chord-wise location. Also, it is possible to notice that hydrofoils with larger cavitation margin display greater curvature than in optimization SEVEN C. Comparing the Pareto fronts between figures 5.16 and 5.18, there is also a slight increase in the range of values of CF1 and CF2.

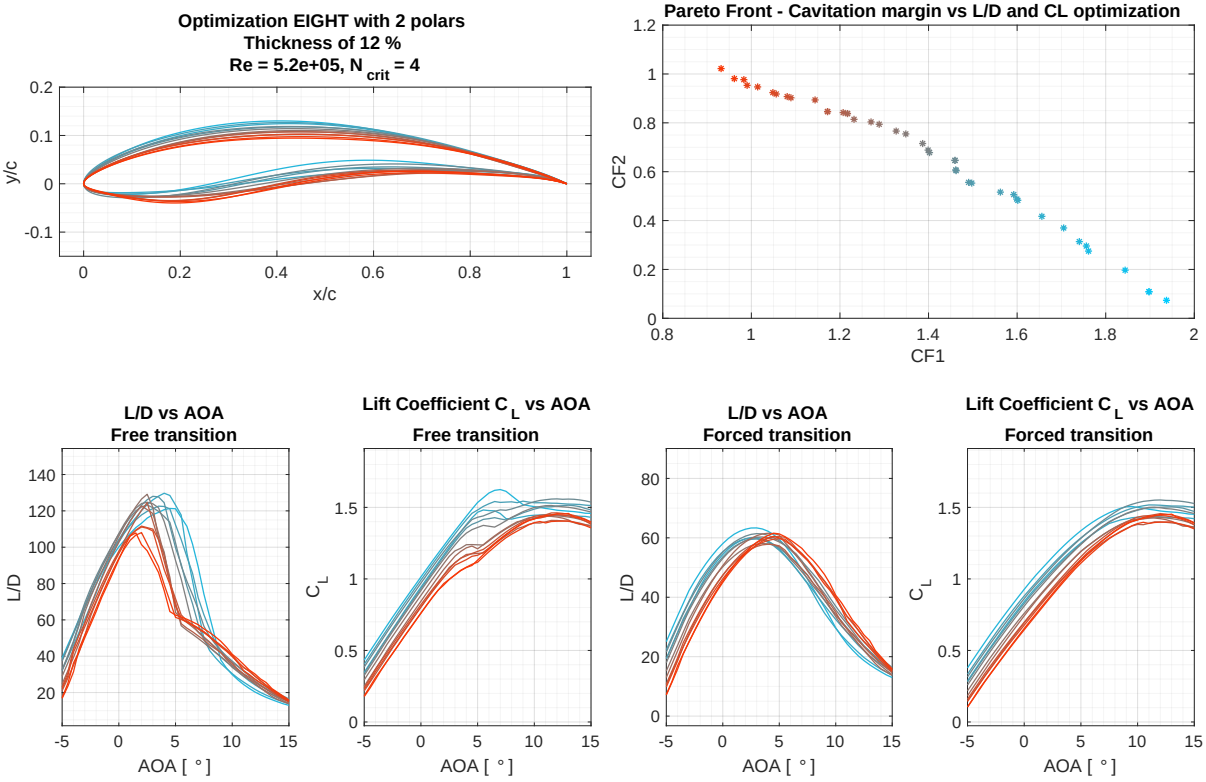

Figure 5.18: Foils, Pareto front and L/D obtained with CF1 EIGHT C for hydrofoils of thickness t/c = 12%

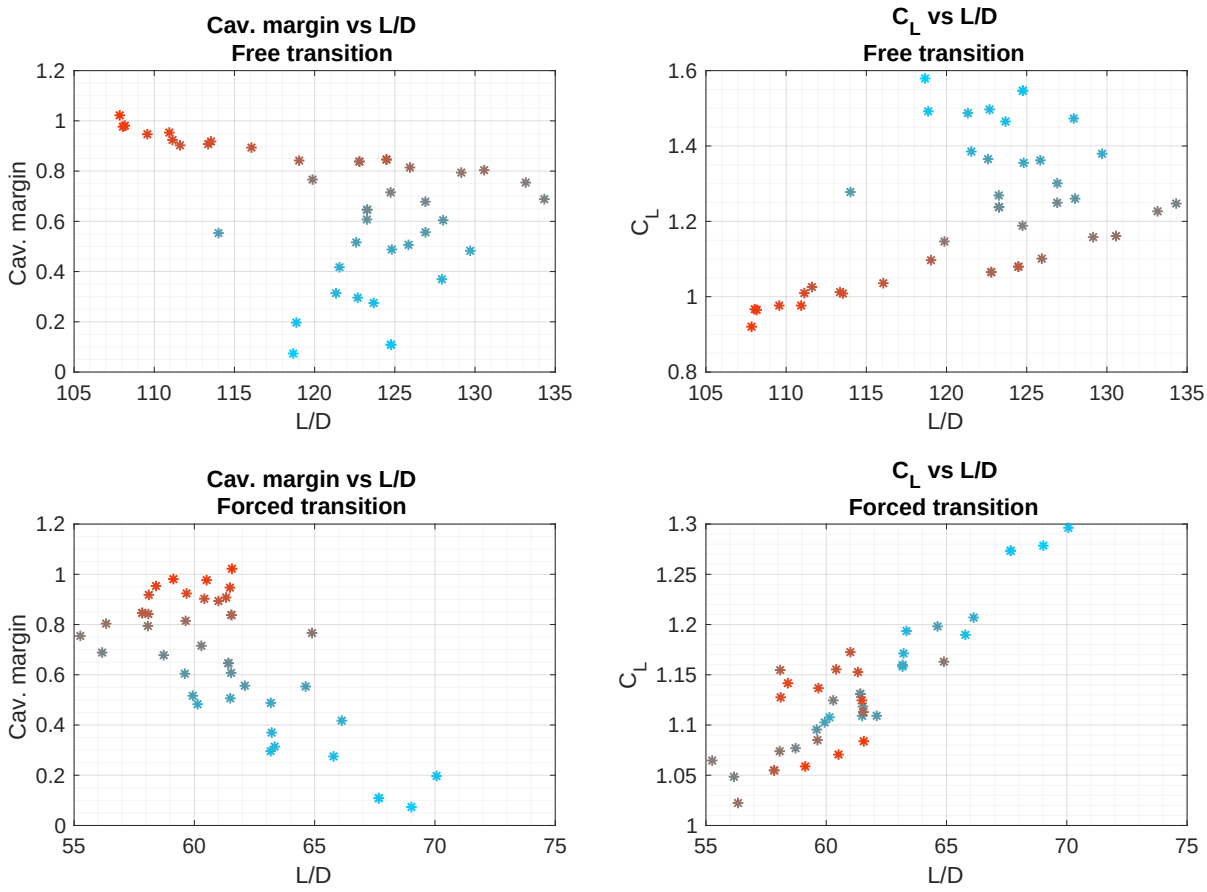

Figure 5.19: Thickness of 12%, optimization EIGHT C - Comparison of free and forced transition regimes with various distributions

A more detailed comparison is in order regarding figure 5.20. It is possible to see that the highest value of cavitation margin is lower for opts. SEVEN C and EIGHT C than for opt. FIVE C. Despite this, for optimizations SEVEN C and EIGHT C, the hydrofoils with higher cavitation margins reach higher level of maximum L/D, in both regimes. The most noticeable fact is that there seems to be an ”offset” along optimizations, as, for the same cavitation margin, values of L/D are progressively higher from opt. FIVE to EIGHT.

Despite these efforts, a significant increase in cavitation margin and performance was not possible. The section at $r/R \approx 100\%$ is the section most susceptible to cavitation, as mentioned earlier. Thus, the design space becomes comprehensively short, hindering the optimization routine's ability to increase the ranges of CF1 and CF2, as it becomes physically impossible to further increase the maximum L/D and optimum C_L without reaching greater suction peaks and, consequently, cavitation.

Although the ranges of CF1 and CF2 are shorter for optimization EIGHT C than for FIVE C, due to the higher values of L/D in both regimes as well as the shape of the resulting hydrofoils, optimization EIGHT C is chosen as the final optimization for the hydrofoils with maximum thickness of 12%. The

reason why geometry is important is due to blade design and is further explained in chapter 6.

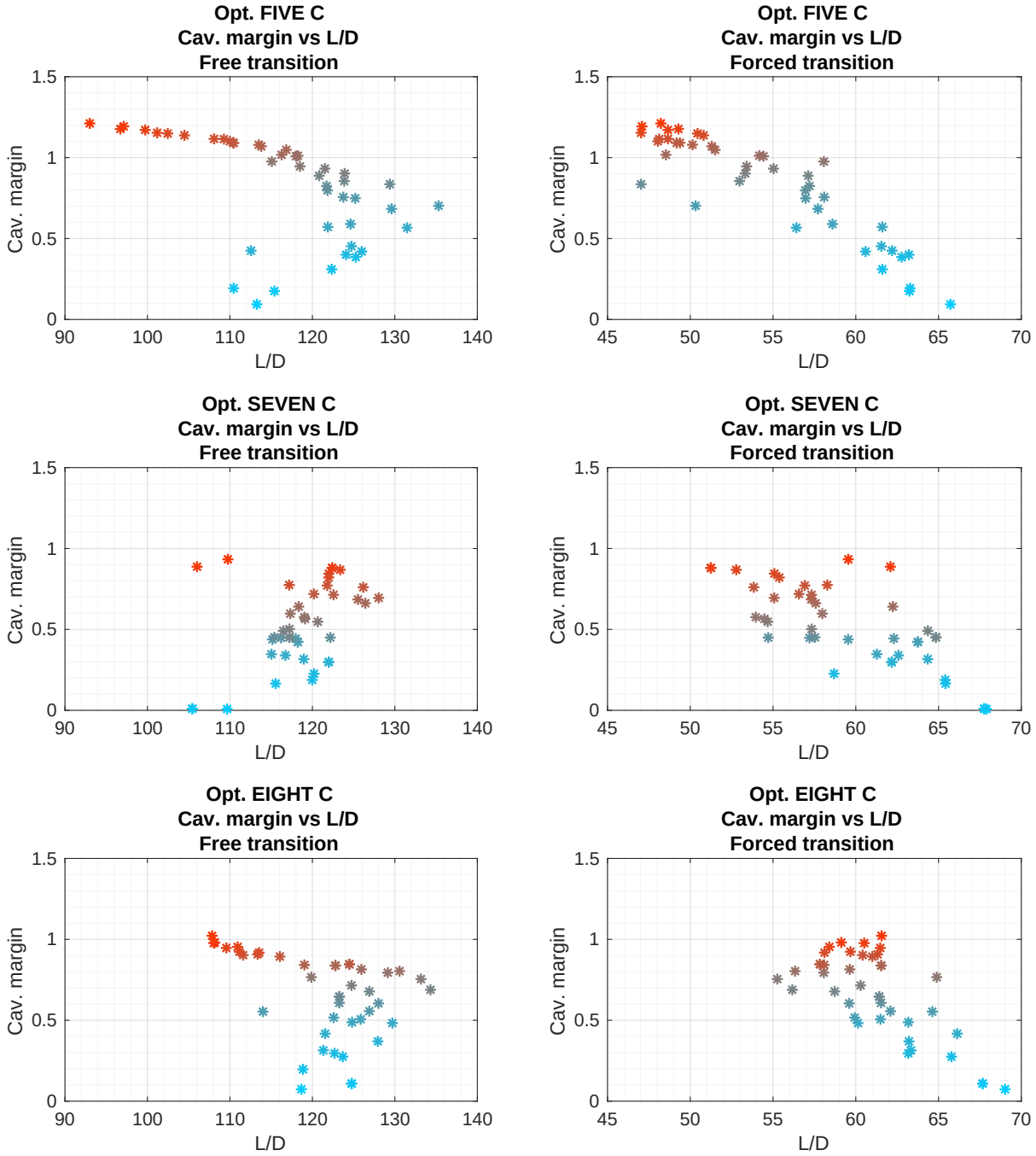

Figure 5.20: Thickness of 12% - Comparison of cavitation margin vs L/D performance for both regimes and all optimizations

Figure 5.21 presents the comparison between the optimized hydrofoils output by optimization EIGHT C and the reference hydrofoils considered, NACA 63-812, NACA 66-812 and S1210.

For the same cavitation margin as the reference hydrofoil NACA 63-812, the corresponding optimized hydrofoil displays improvements of 17.64% and 30.20% in maximum L/D and optimum C_L, respectively, for the clean regime; for the rough regime, there is an improvement of 11.40% in optimum C_L and a

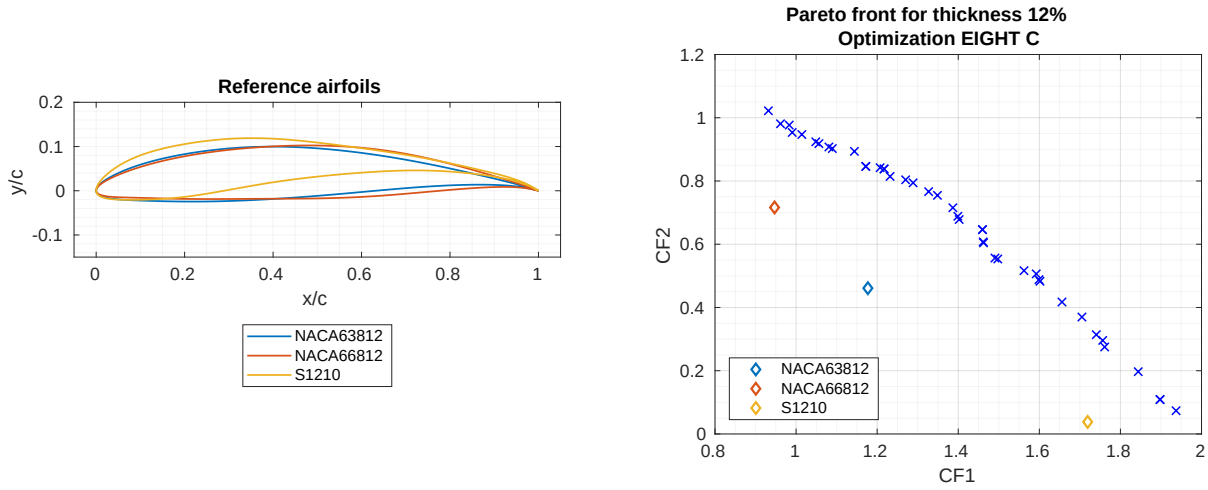

Figure 5.21: Thickness of 12%, optimization EIGHT C - Comparison with reference hydrofoils

reduction of 8.24% in maximum L/D.

For this optimization, the reference hydrofoil S1210 is outperformed by 6 hydrofoils, and all have greater cavitation margin. The first optimized hydrofoil (greater CF1 value) improves the performance of S1210 by 12.63% and 11.56% in maximum L/D and optimum C_L, respectively, in clean regime. In rough regime there is a decrease of 2.17% in L/D and an increase of 3.03% in optimum C_L.

Chapter 6

Selected hydrofoils, IST-MT1-XX

For each blade section and among the data presented in chapter 5, five hydrofoils are chosen, one for each section. The choice is mainly related with the design of a new turbine, exposed in chapter 7. Detailed data relative to each foil is presented in the following sections.

IST-MT1-XX is the name chosen for the hydrofoils, and stands for:

- IST - **I**nstituto **S**uperior **T**écnico, faculty in which this work is produced ;
- MT1 - **M**arine **T**urbine, generation of hydrofoils **1**, i.e., first hydrofoils produced by a work of this type ;
- XX - Two numbers denoting the maximum thickness of the hydrofoil. If maximum t/c is 18%, the foil is named IST-MT1-18.

The criteria of selection for the hydrofoils is as follows:

- Equal or similar optimum angle of attack between adjacent sections of the blade. The difference in optimum angle of attack should be small so the blade design is simpler ;
- High value of L/D, in order to obtain a greater energy conversion efficiency in turbine operation, translated in a higher value of power coefficient C_P. In this hydrofoil selection, emphasis is given to L/D in the clean regime ;
- Similarity of the hydrofoil geometry along the radius of the blade r, according to common practice [58]. This excludes geometries that deviate excessively from the remaining hydrofoils.

High cavitation margin is also required for each section, and thus this factor is also taken into account in the selection of each hydrofoil.

Other criteria, like choosing hydrofoils by highest value of optimum C_L in order to reduce blade chord size, are disregarded. This is considered more of an economical concern, and thus falls out of the scope of this study.

In the following sections, each chosen hydrofoil is presented along with its position in the Pareto front of the respective optimization and 4 plots, containing:

- Lift coefficient C_L vs drag coefficient C_D for free and forced transition ;

- Lift to drag L/D vs angle of attack AOA for free and forced transition ;
- Pressure coefficient distribution $-C_p$ vs chord-wise position x/c for both regimes and their respective optimum AOA and also for the rough regime at AOA$_{opt\,clean}$;
- Cavitation bucket, i.e., angle of attack AOA vs minimum pressure coefficient $-C_{p_{min}}$.

In this way, each hydrofoil geometry is fully detailed.

6.1 IST-MT1-24

Hydrofoil IST-MT1-24 is located at r/R = 20% of the blade. Hydrofoil geometry and related data are shown in figure 6.1. IST-MT1-24's peak performance of $L/D_{max\,free}$ = 163.74 occurs at AOA$_{opt\,free}$ = 5.50° for the free transition. $C_{L\,opt\,free}$ is 1.451. Optimum performance with forced transition occurs at AOA$_{opt\,forced}$ = 6° , yielding a $L/D_{max\,forced}$ of 85.78. $C_{L\,opt\,forced}$ is 1.372. The minimum pressure coefficient C_p at AOA$_{opt\,free}$ occurs at x/c = 25% and equals -2.2. If transition occurs at AOA$_{opt\,free}$, this hydrofoil yields L/D_{forced} = 85.66, and a $C_{L\,forced}$ = 1.333. High value of L/D is important as most start-up torque is generated near the root region of the blade [31].

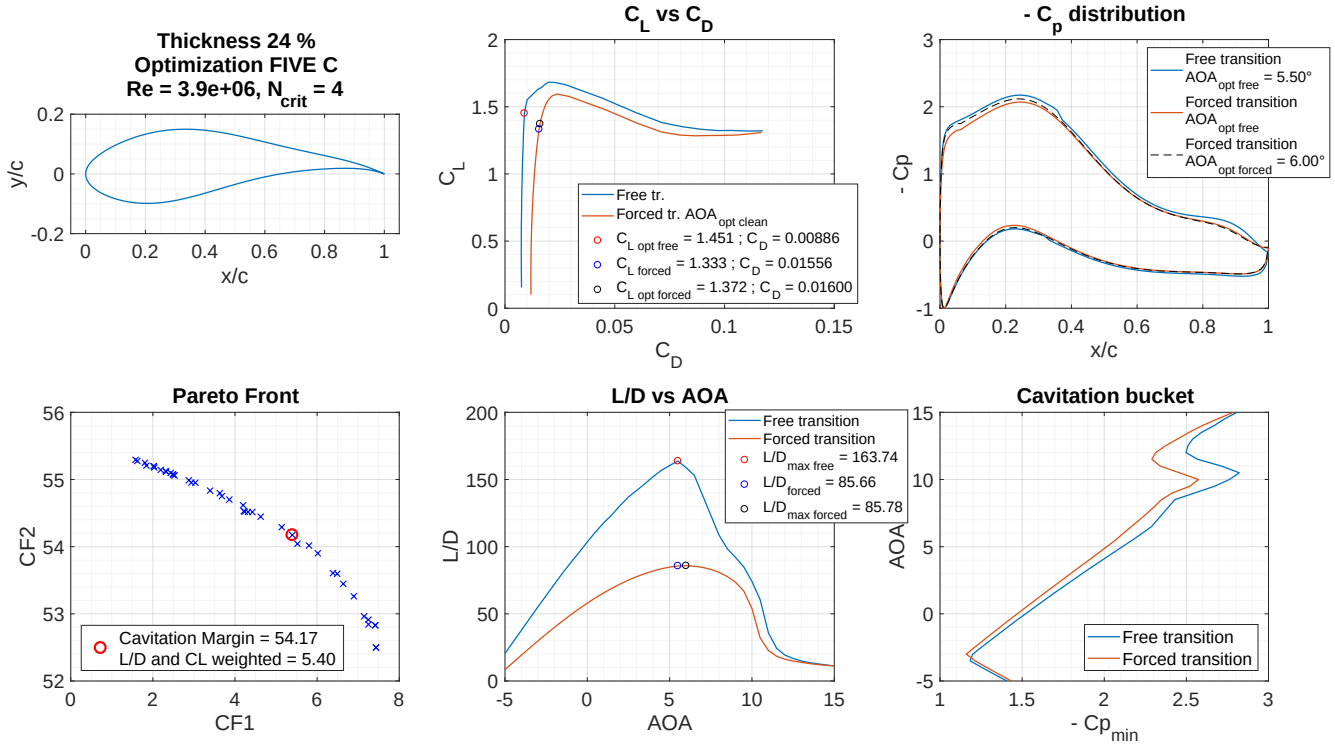

Figure 6.1: IST-MT1-24 - Geometry of the hydrofoil and related data

6.2 IST-MT1-21

Hydrofoil IST-MT1-21 is located at r/R = 30% of the blade. Hydrofoil geometry and related data are shown in figure 6.2. IST-MT1-21's $L/D_{max\,free}$ = 183.76 occurs at AOA$_{opt\,free}$ = 5.50° for the free

transition. $C_{L\,opt\,free}$ is 1.537. Optimum performance with forced transition occurs at AOA$_{opt\,forced}$ = 6° , yielding a $L/D_{max\,forced}$ of 95.39. $C_{L\,opt\,forced}$ is 1.425. The minimum pressure coefficient C_p at AOA$_{opt\,free}$ occurs at x/c = 27% and equals -2.1. If transition occurs at AOA$_{opt\,free}$, this hydrofoil yields L/D_{forced} = 95.31, and a $C_{L\,forced}$ = 1.466.

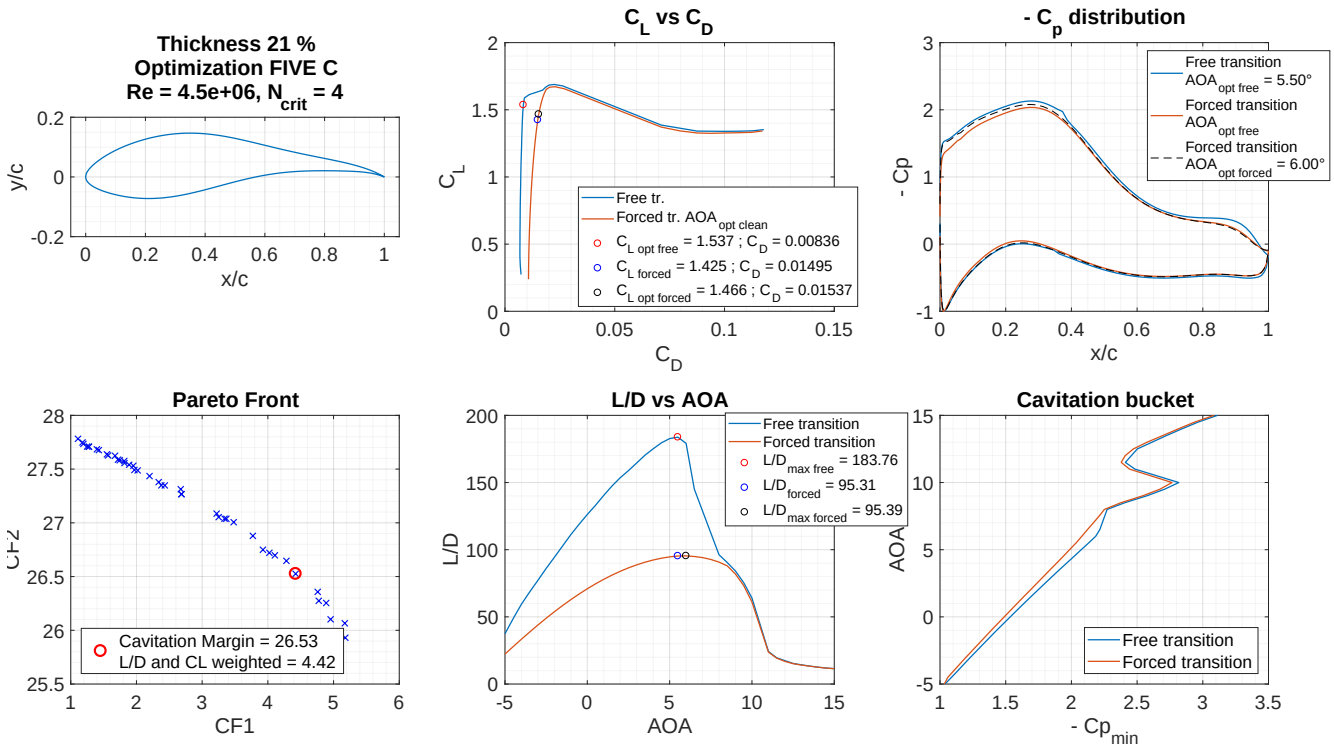

Figure 6.2: IST-MT1-21 - Geometry of the hydrofoil and related data

6.3 IST-MT1-18

Hydrofoil IST-MT1-18 is located at section r/R = 45% of the blade, almost half the blade span. Hydrofoil geometry and related data are shown in figure 6.3. IST-MT1-18's $L/D_{max\,free}$ = 190.55 occurs at AOA$_{opt\,free}$ = 4° for the free transition. $C_{L\,opt\,free}$ is 1.613. Optimum performance with forced transition occurs at AOA$_{opt\,forced}$ = 2.5° , yielding a $L/D_{max\,forced}$ of 95.61. $C_{L\,opt\,forced}$ is 1.332. The minimum pressure coefficient C_p at AOA$_{opt\,free}$ occurs at x/c = 27% and equals -2.05. If transition occurs at AOA$_{opt\,free}$, this hydrofoil yields L/D_{forced} = 93.83, and a $C_{L\,forced}$ = 1.452.

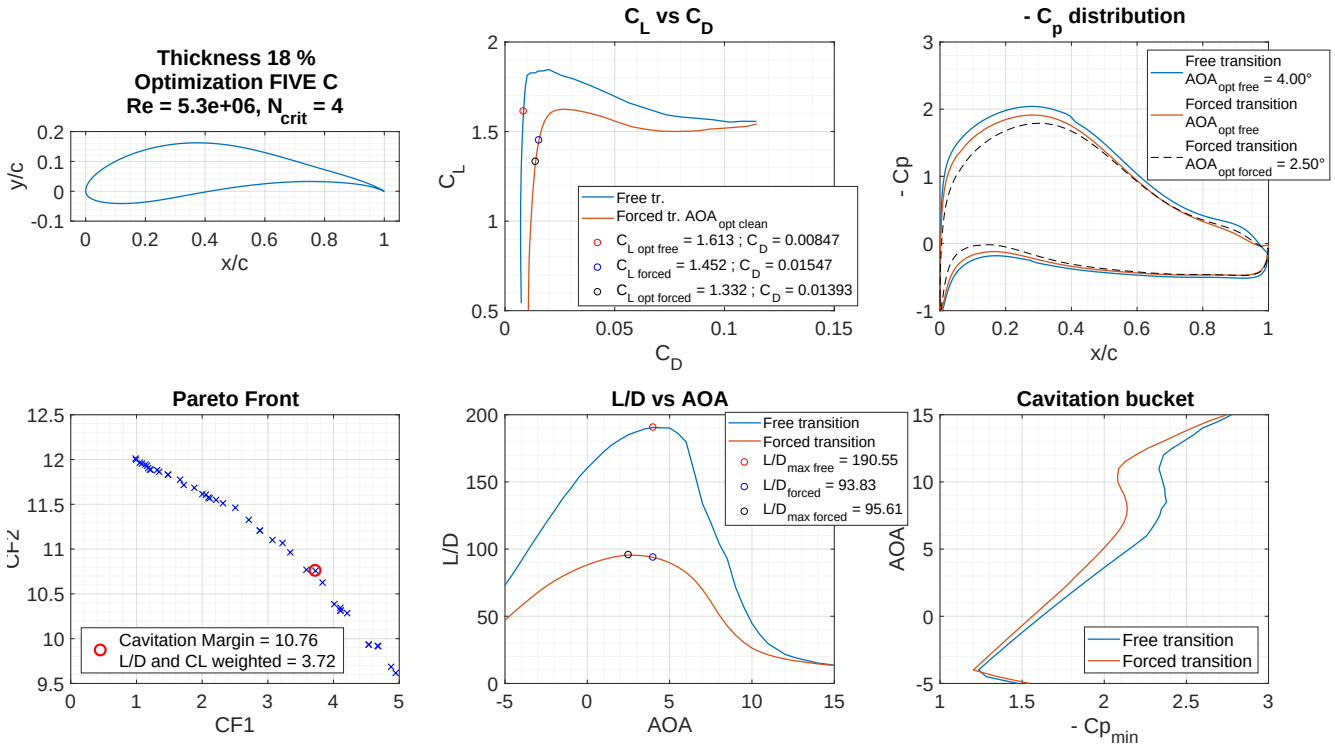

Figure 6.3: IST-MT1-18 - Geometry of the hydrofoil and related data

6.4 IST-MT1-15

Hydrofoil IST-MT1-15 is located at section r/R = 75%. Hydrofoil geometry and related data are shown in figure 6.4. At this section, a high value of L/D is of paramount importance, as most power extracting torque is generated at the outer half of the blade [31]. IST-MT1-15's $L/D_{max\,free}$ reaches 227.99, and occurs at AOA$_{opt\,free}$ = 3.5° for the free transition. $C_{L\,opt\,free}$ at this point is 1.534. Optimum performance with forced transition occurs at AOA$_{opt\,forced}$ = 2° , yielding a $L/D_{max\,forced}$ of 93.04. $C_{L\,opt\,forced}$ at this point is 1.217. The minimum pressure coefficient C_p at AOA$_{opt\,free}$ occurs at x/c = 40% and equals -1.7. If transition occurs at AOA$_{opt\,free}$, this hydrofoil yields L/D_{forced} = 90.49 and a $C_{L\,forced}$ = 1.336.

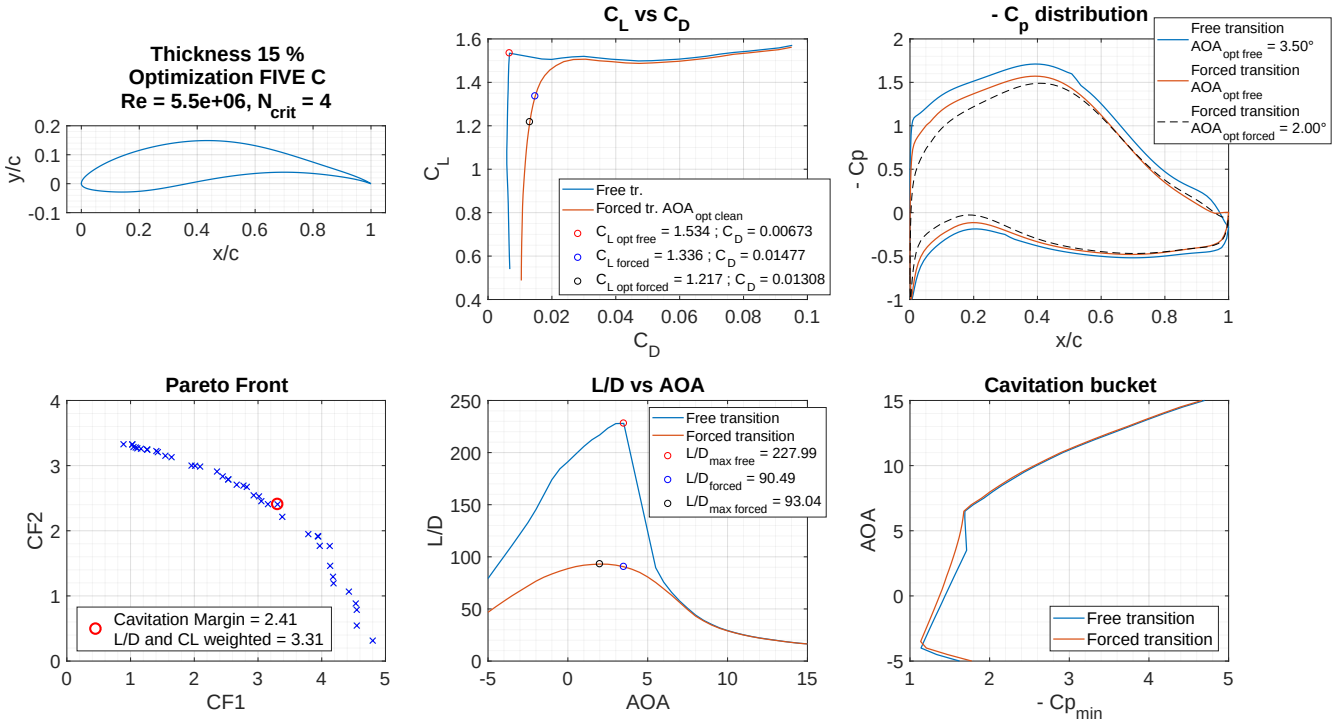

Figure 6.4: IST-MT1-15 - Geometry of the hydrofoil and related data

6.5 IST-MT1-12

Hydrofoil IST-MT1-12 is located at the tip of the blade, $r/R \approx 100\%$. Hydrofoil geometry and related data are shown in figure 6.5. IST-MT1-12's $L/D_{max\,free}$ equals 130.57 , and occurs at AOA$_{opt\,free}$ = 2.50° for the free transition. $C_{L\,opt\,free}$ at this point is 1.161. Optimum performance with forced transition occurs at AOA$_{opt\,forced}$ = 3° , yielding a $L/D_{max\,forced}$ of 56.33. $C_{L\,opt\,forced}$ at this point is 1.022. The minimum pressure coefficient C_p at AOA$_{opt\,free}$ occurs at x/c = 25% and equals -1.15. If transition occurs at AOA$_{opt\,free}$, this hydrofoil yields L/D_{forced} = 56.02 and a $C_{L\,forced}$ = 0.980.

As mentioned before, a high value of L/D is desirable, importantly on the outer half of the blade span. Due to the possibility of cavitation at this section, higher values of lift to drag were not possible to obtain. This hydrofoil is chosen for its acceptable cavitation margin (0.80) and performance, as well as a similar angle of attack with the adjacent section.

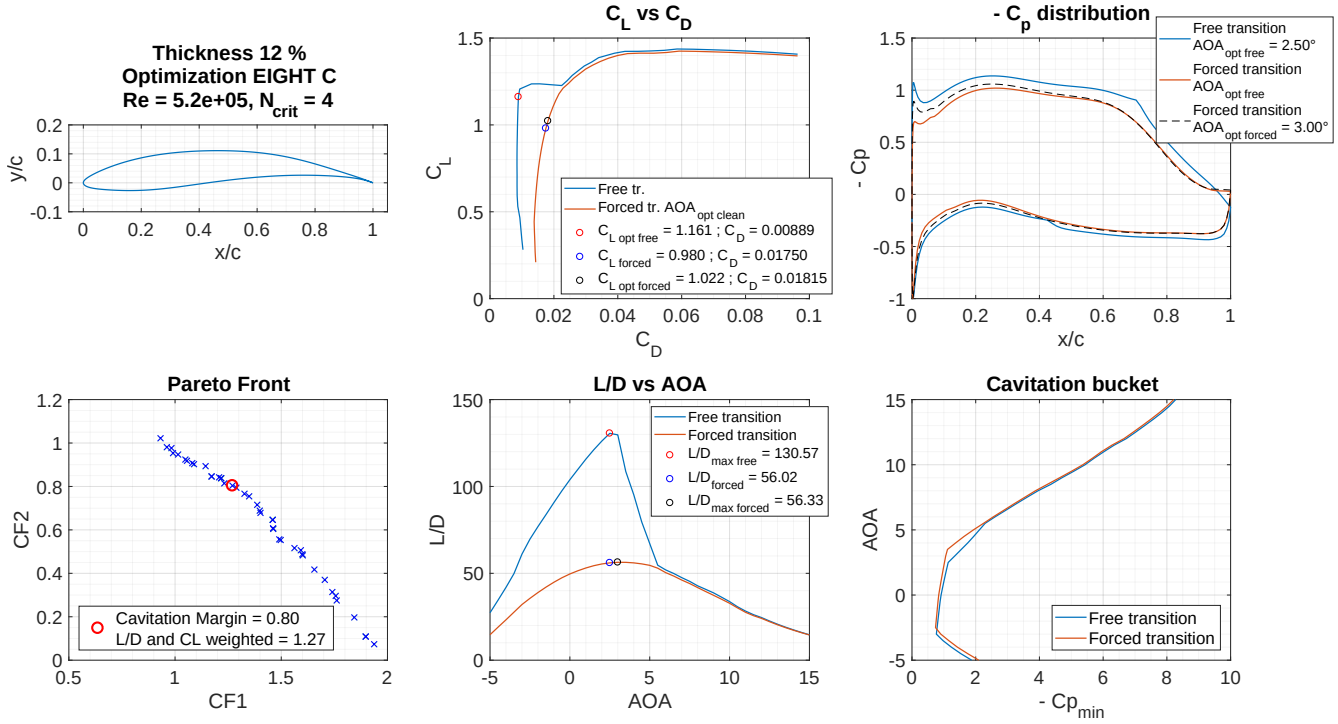

Figure 6.5: IST-MT1-12 - Geometry of the hydrofoil and related data

6.6 Redesigned turbine layout

Figure 6.6 displays the layout of the redesigned turbine blades along with the following data:

- Pressure distribution C_p along chord x/c for the AOA$_{opt\ clean}$;
- C_L vs AOA curves for both regimes (free and forced transition);
- L/D vs AOA curves for both regimes.

All data curves are calculated at the Reynolds number experienced by the foil at the respective section r/R of the reference turbine.

Table 6.1: Blade section information

Span r/R	Foil at section	Thickness t/c [%]	Optimum AOA AOA$_{opt\ clean}$ [°]	Optimum C_L $C_{L\ opt\ free}$	Maximum L/D $L/D_{max\ free}$
20	IST-MT1-24	24	5.5	1.451	163.74
30	IST-MT1-21	21	5.5	1.537	183.76
45	IST-MT1-18	18	4.0	1.613	190.55
75	IST-MT1-15	15	3.5	1.534	227.99
100	IST-MT1-12	12	2.5	1.161	130.57

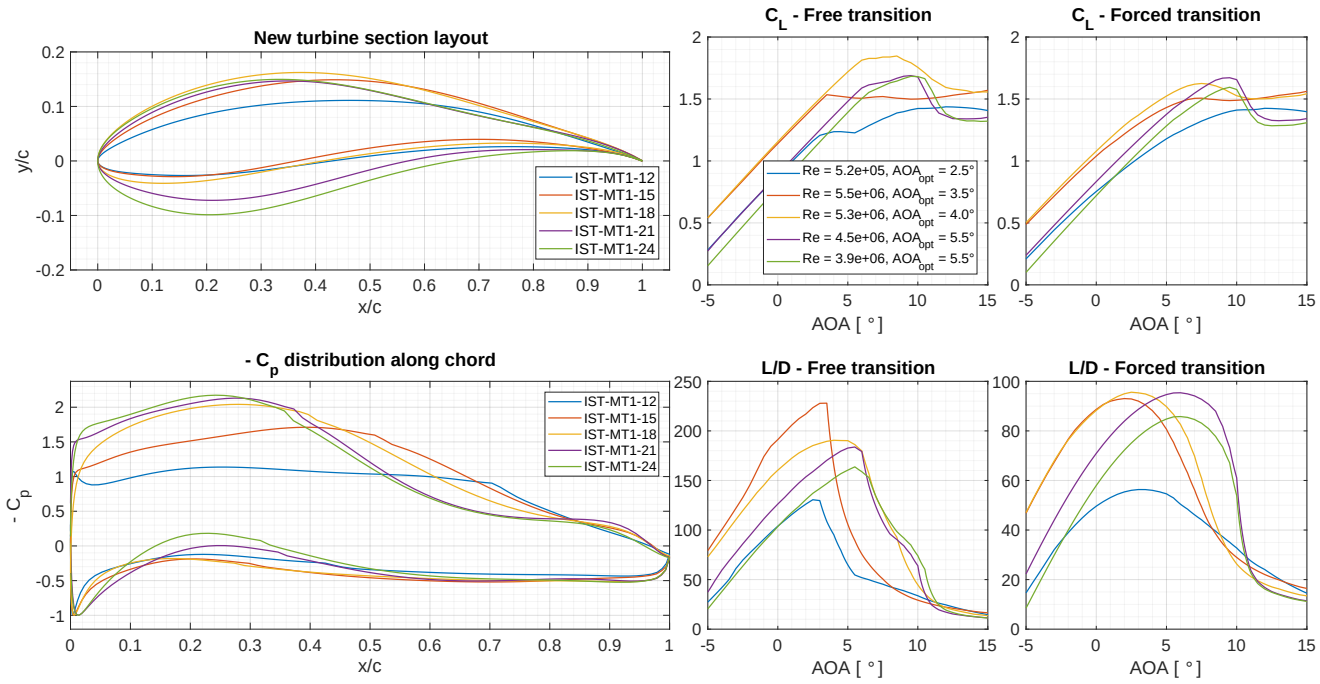

Figure 6.6: Chosen hydrofoils incorporating redesigned turbine blades

Chapter 7

Redesign of horizontal axis turbine

7.1 Redesigned turbine section data

The hydrofoils that compose the various sections of the blade are, as previously mentioned, the optimized hydrofoils presented in chapter 6. These were analysed in software XFOIL for Reynolds number of $1{\cdot}10^6$, $3{\cdot}10^6$ $5{\cdot}10^6$, $1{\cdot}10^7$ and $2{\cdot}10^7$. Figure 7.1 displays these results for hydrofoil IST-MT1-15.

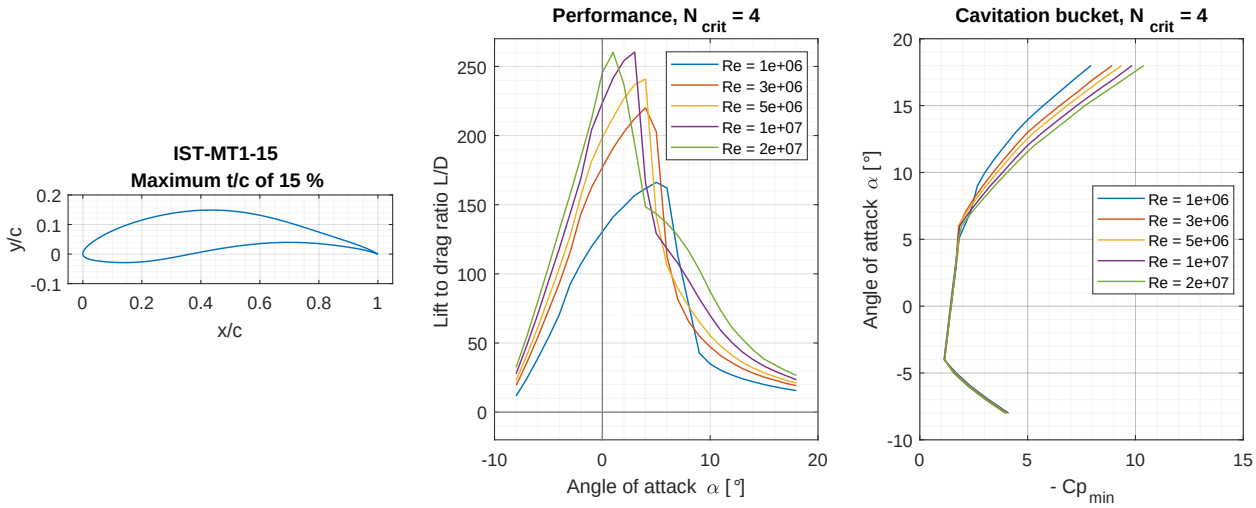

Figure 7.1: IST-MT-15 hydrofoil, performance and cavitation bucket - data obtained with XFOIL

Complete data on all IST-MT1-XX hydrofoils can be seen in appendix B.

7.2 Redesigned turbine characteristics and performance

As mentioned previously, a novel turbine rotor design is made by incorporating the optimized hydrofoils detailed in chapter 6 into the blades. This new design is carried out with the lifting line routine mentioned in chapter 3 and used for designing the reference turbine. The lifting line routine results for blade geometry, i.e. chord and twist, can be seen in figures 7.2a and 7.2b, respectively.

The redesigned turbine displays a power coefficient of 0.4857 at design conditions, TSR = 6 and U

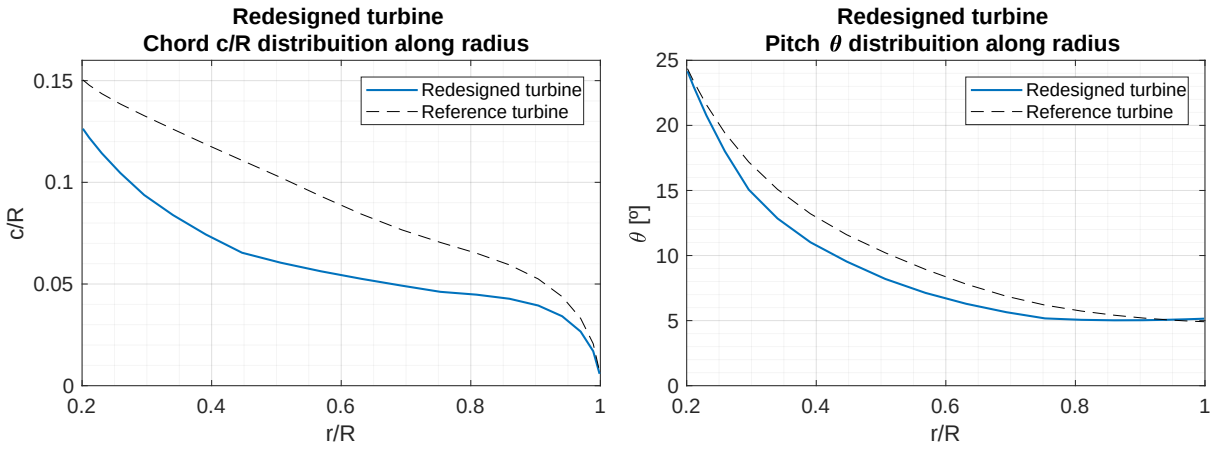

(a) Chord distribution

(b) Pitch distribution

Figure 7.2: Redesigned turbine blades' chord and pitch distribution

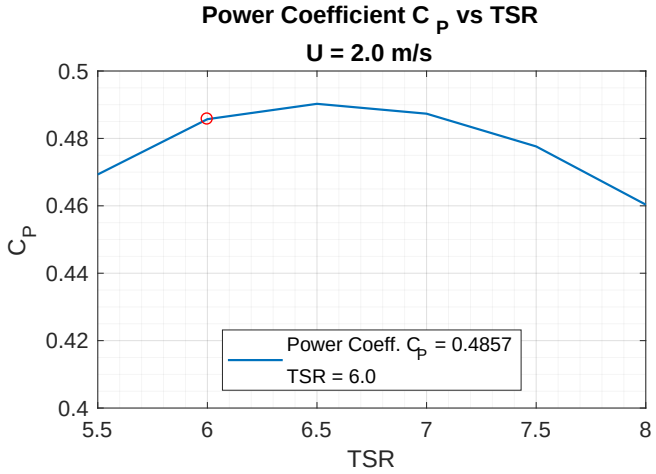

Figure 7.3: Power coefficient variation with TSR

= 2 m/s (see figure 7.3). At TSR = 6.5, C_P is 0.4903. Comparing with the reference turbine at design conditions, an increase of 0.33% is verified. At TSR of 6.5, an increase of 1.16% is achieved. The redesigned turbine also presents higher value of C_P for higher values of TSR. Table 7.1 presents the chord, thickness, pitch and Reynolds number radial distributions at the design conditions of the designed turbine along the blade span.

The same methodology used to design the reference turbine is used to design the new turbine in order to have the most direct means of comparison possible. This methodology consists on defining each hydrofoil at a specific radial section, leaving the routine to iterate values of Reynolds number, C_L, C_D and angle of attack between each of these radial positions. The author strongly believes that a higher value of power coefficient would be achieved if instead of defining the hydrofoils on discrete positions, these were defined in ranges (for example, from r/R = 75% to 90% the blade section would be IST-MT1-15). This would help the lifting line method calculations to be more accurate, as the methodology used for the reference turbine (definition on specific radial sections) penalizes the performance when calculations are made with the optimized hydrofoils due to the differences in angle of attack, L/D and C_L from section to section.

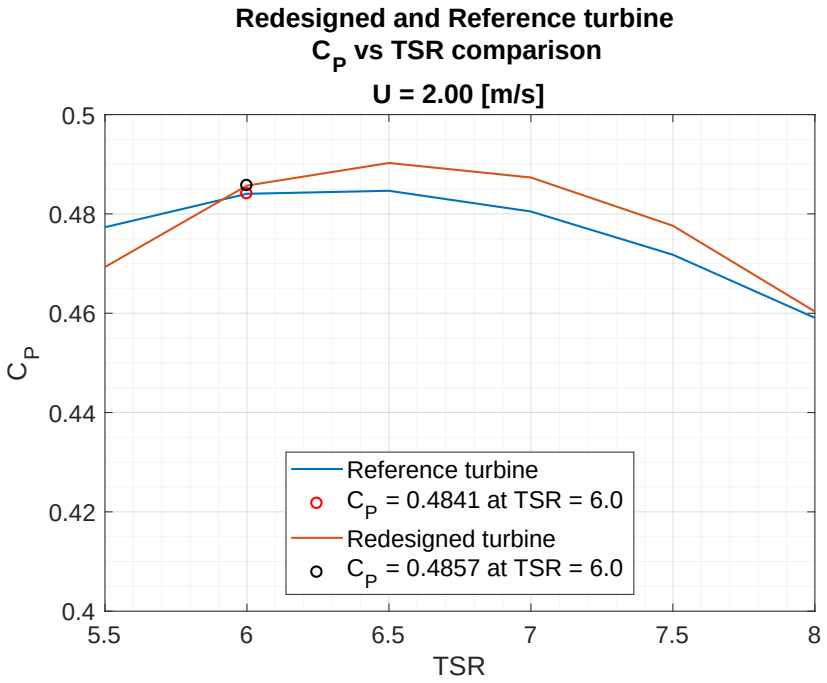

Figure 7.4: Redesigned and reference turbine C_P vs TSR comparison

Table 7.1: Redesigned turbine data

Span r/R [%]	Chord, c/R c/R [%]	Thickness t/c [%]	Pitch θ [$^\circ$]	Reynolds Re [-]	Chord reduction [%]
20	12.6	24.0	24.2	3.3e+06	16.0
25	12.2	22.5	22.9	3.3e+06	17.5
30	11.4	21.0	20.8	3.2e+06	20.4
31	10.5	20.7	18.0	3.2e+06	24.5
35	9.4	19.5	15.1	3.2e+06	29.4
40	8.4	18.7	12.8	3.2e+06	33.5
44	7.4	18.1	11.0	3.2e+06	37.4
45	6.5	18.0	9.5	3.1e+06	41.0
50	6.0	17.6	8.2	3.3e+06	40.9
55	5.6	17.1	7.1	3.4e+06	39.6
60	5.3	16.6	6.3	3.5e+06	37.7
65	4.9	16.1	5.6	3.6e+06	35.8
70	4.6	15.6	5.2	3.6e+06	34.5
74	4.5	15.1	5.1	3.7e+06	31.3
75	4.3	15.0	5.0	3.8e+06	28.0
80	3.9	14.6	5.0	3.7e+06	24.9
85	3.4	14.1	5.1	3.3e+06	22.0
90	2.7	13.6	5.1	2.7e+06	19.6
93	1.7	13.1	5.1	1.7e+06	17.8
100	0.6	12.0	5.2	6e+05	16.9

From figure 7.2a it is possible to notice that chord size is reduced. Although the main objective is performance improvement, namely, increase of C_P, a reduction in chord is advantageous in other perspectives, and thus cannot be disregarded. This reduction in chord size is displayed in table 7.1. The

chord size reduction is due to the higher value of C_L of the hydrofoils IST-MT1-XX. Such a reduction in chord naturally renders a lower Reynolds number at each radial section of the blade. These results suggest that, with the optimized hydrofoils, it would be possible to reduce the blade size and consequently its weight and cost and still obtain the same output of power, keeping the structural integrity of the blade in mind.

Span r/R [%]	Foil at section	Reynolds Re [-]
20	IST-MT1-24	3.3e+06
30	IST-MT1-21	3.1e+06
45	IST-MT1-18	3.1e+06
75	IST-MT1-15	3.8e+06
100	IST-MT1-12	6e+05

Table 7.2: Blade section information

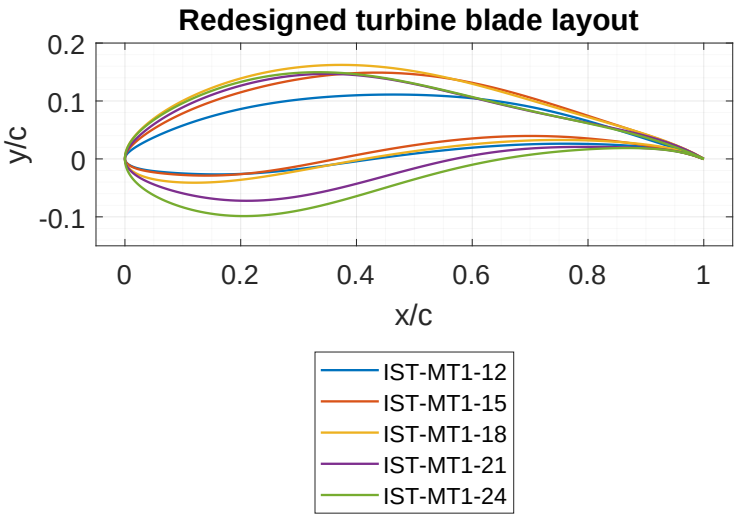

Figure 7.5: Blade section layout

Table 7.2 and figure 7.5 discriminate the layout of the blade IST-MT1-XX per radial section and operating Reynolds number.

All the data regarding the redesigned turbine is available in appendix B.

Chapter 8

Conclusions

In this final chapter, conclusions are drawn from the work developed. The main results are pointed out regarding:

- The reference turbine, discussed in chapter 3;
- The hydrofoil design cost function development and final results, namely foil geometry and performance, discussed in chapters 4 and 5, respectively;
- The new turbine, redesigned with blades composed by the new optimized hydrofoils IST-MT1-XX.

Finally, future work recommendations are made.

8.1 Reference turbine

$\mathbf{N_{crit}}$ factor influence on foil performance

The N_{crit} factor is the exponent in what is called the e^n method, which is implemented in XFOIL. The user-specified parameter N_{crit} is the logarithm of the amplification factor of the most-amplified frequency which triggers transition.

The N_{crit} factor is found to alter not only the performance for all the Reynolds numbers tested but also the optimum AOA at which peak performance occurs. Along with these changes, this factor also has a very noticeable effect on the chord-wise location of transition for all Reynolds numbers tested. Thus, the N_{crit} factor influence inclusion is of paramount importance for studies of this nature in order to successfully mimic the operating conditions and enhance the studies' proximity to real scenarios.

Reference turbine geometry and performance

The reference turbine is based on work published by Bahaj *et al.* [19], and is designed through a routine based on lifting line theory [39][20]. The new turbine design theoretically increases the power coefficient C_P relative to the Bahaj turbine by 6.1%, for the same design conditions.

All the information regarding the reference turbine is in tables 3.2 and 3.3 as well as in appendixes A.2 to A.4. Appendix A.1 contains detailed information regarding the hydrofoils that compose the reference turbine blades.

8.2 Hydrofoil design

Cost function evolution

Along this work the cost function evolved incrementally aiming to further and fully explore the design space.

CF2, despite its apparent simplicity, is successful in increasing the cavitation margin for all blade sections and respective thicknesses. This is possible to confirm by analysing hydrofoils from any optimization individually. As one advances from a hydrofoil with lower CF2 value to one with higher (as in figure 4.3), it is possible to observe that hydrofoils progressively achieve lower values of $C_{p_{min}}$, thus being less susceptible to cavitation. Cavitation margin values of up to 3 relative to the local cavitation number are obtained.

Regarding CF1, as the progression is made from version ONE C to FIVE C, the final version, hydrofoils with better overall (clean and rough regimes) are obtained, as is intended; hydrofoils with good performance for a range of angles of attack around the optimum angle of attack are also achieved. CF1 version FIVE C yields results which feature these characteristics. The output Pareto front also features good spread, fully exploring the available design space.

Additional optimizations for section $r/R \approx 100\%$ are carried out exceptionally, as for this section the need is felt to further increase performance and cavitation margin. The optimization routine, with cost function EIGHT C, outputs hydrofoils of maximum thickness of 12% with better performance than for version FIVE C, although not increasing cavitation margin.

The final results, discussed in chapter 5, all yield Pareto fronts with good spread. Overall, for all sections, the reference hydrofoils of series NACA 63-8XX and NACA 66-8XX are outperformed.

Hydrofoil geometry along Pareto fronts

Overall, the optimized hydrofoils' geometry follows the same tendencies for all sections, thicknesses and optimizations. As the Pareto front scores decrease in cavitation margin, i.e., CF2 value decreases and CF1 value increases, there is a displacement of the maximum thickness chord-wise location to a position closer to the leading edge along with an increase in camber. This is natural, as greater camber renders higher suction values for positive angles of attack. Optimized hydrofoils with higher cavitation margin also tend to display a sharper leading edge.

Optimized hydrofoils performance relative to reference hydrofoils

In terms of performance, the optimized hydrofoils, relative to the reference hydrofoils of the series NACA 63-8XX, at the same cavitation margin, display improvements in maximum L/D and optimum C_L of up to 66.10% and 23.06%, respectively, in the clean regime; in the rough regime, improvements in maximum L/D and optimum C_L reach values of 73.21% and 99.82%, respectively. Regarding the reference hydrofoils of series NACA 66-8XX, improvements reach larger values.

These results prove that, overall, the optimized hydrofoils have better performance not only with natural (free) transition, clean regime, but also with forced transition, rough regime. This fact demonstrates that the optimization setup along with the cost functions developed is successful in improving on the performance of the reference hydrofoils on all fronts, meaning that, if transition occurs, the optimized hydrofoils will still perform better than the reference.

8.3 Redesigned turbine with selected IST-MT1-XX foils

Criteria for selection of IST-MT1-XX hydrofoils

The criteria employed for hydrofoil selection consists on: hydrofoils of adjacent sections having equal or similar optimum angle of attack; high value of L/D, in order to obtain a greater energy conversion efficiency in turbine operation, i.e., higher C_P; similarity of the hydrofoil geometry along the radius of the blade r. This criteria results in the selection of hydrofoils IST-MT1-24, IST-MT1-21, IST-MT1-18, IST-MT1-15 and IST-MT1-12.

Redesigned turbine geometry and performance

The reference turbine is successfully redesigned to incorporate the hydrofoils IST-MT-XX in its blades, yielding a power coefficient of C_P of 0.4857 at the design conditions of TSR = 6 and U = 2 m/s. This change in C_P represents an increase of 0.33% relative to the performance of the reference turbine at design conditions. For the off design conditions of TSR = 6.5, the increase in C_P is of 1.16%.

Lifting line theory predicts a significant chord reduction between the reference and redesigned turbines, which suggests that it would be possible to have the same power output while operating a turbine with much smaller, lighter and thus cheaper blades. Although the main objective is performance improvement, namely, increase of C_P, a reduction in chord is advantageous, and thus cannot be disregarded and is a positive result.

The same methodology is used to design both reference turbine and the new turbine in order to have a direct comparison. If this methodology is disregarded and instead, the hydrofoils are defined along ranges of radial positions (for example, from r/R = 75% to 90% the blade section would be IST-MT1-15), the author strongly believes that a larger increase in C_P would be obtained.

8.4 Future Work

Regarding future work in the energy generation from marine currents field, more specifically through marine current turbines, there are several additional parameters and considerations that can be taken into account:

- **Quantification of the importance that should be given to each transition regime:** the amount of time that turbine blades operate with free or forced transition is unknown. In this work, equilibrium between clean and rough regimes is intended; however, there is uncertainty regarding which regime is more important;
- **Further optimization of operation with forced transition:** despite the previous point, if transition is to occur, the turbine performance is largely affected. Given the adverse environment in which these turbines operate and the likely possibility that the blades may become soiled in some manner, transition is likely to occur and thus a better performance with forced transition should be an aim of future studies;
- **Comprehensive analysis of fouling effects:** studying the influence of fouling and optimizing hydrofoils and blades to counter its adverse effects can, in the future, extend the range of operating conditions and prevent anomalous situations that could severely hinder the turbine operational performance;
- **Include turbulent perturbations influence**: fluctuations induced by in-flow turbulence on the effective section velocity and angle of attack should be accounted for. These additions would likely be an extension to optimization SIX C;
- **Include waves influence:** modelling the effects on flow speed and local pressure due to the presence of ocean waves can further prepare optimized hydrofoils for real operating conditions.

As a final note, looking at blade design and hydrofoil optimization from an economical perspective, one might consider focusing optimization efforts on specifically reducing blade chord dimension by maximizing optimum C_L, thus reducing blade weight and cost.

Bibliography

[1] U.S. Energy Information Administration. Annual Energy Outlook 2011. Technical Report April, 2011.

[2] The Executive Committee of Ocean Energy Systems. An overview of Ocean Energy activities in 2017 - Annual Report. Technical report, 2017.

[3] R. Pelc and R. M. Fujita. Renewable energy from the ocean. *Marine Policy*, 26(6):471–479, 2002. ISSN 0308597X. doi: 10.1016/S0308-597X(02)00045-3.

[4] Z. Zhou, M. Benbouzid, J.-F. Charpentier, F. Scuiller, and T. Tang. Developments in large marine current turbine technologies – A review. *Renewable and Sustainable Energy Reviews*, 71:852–858, may 2017. ISSN 13640321. doi: 10.1016/j.rser.2016.12.113. URL http://linkinghub.elsevier.com/retrieve/pii/S1364032116311698.

[5] K. W. Ng, W. H. Lam, and K. C. Ng. 2002-2012: 10 Years of Research Progress in Horizontal-Axis Marine Current Turbines. *Energies*, 6(3):1497–1526, 2013. ISSN 19961073. doi: 10.3390/en6031497.

[6] M. J. Khan, G. Bhuyan, M. T. Iqbal, and J. E. Quaicoe. Hydrokinetic energy conversion systems and assessment of horizontal and vertical axis turbines for river and tidal applications: A technology status review. *Applied Energy*, 86(10):1823–1835, 2009. ISSN 03062619. doi: 10.1016/j.apenergy.2009.02.017. URL http://dx.doi.org/10.1016/j.apenergy.2009.02.017.

[7] A. Roberts, B. Thomas, P. Sewell, Z. Khan, S. Balmain, and J. Gillman. Current tidal power technologies and their suitability for applications in coastal and marine areas. *Journal of Ocean Engineering and Marine Energy*, 2(2):227–245, 2016. ISSN 21986452. doi: 10.1007/s40722-016-0044-8.

[8] Z. Zhou, F. Scuiller, J. F. Charpentier, M. Benbouzid, and T. Tang. An up-to-date review of large marine tidal current turbine technologies. In *Proceedings - 2014 International Power Electronics and Application Conference and Exposition, IEEE PEAC 2014*, number November, pages 480–484, 2014. ISBN 9781479967674. doi: 10.1109/PEAC.2014.7037903.

[9] P. Fraenkel. Development and Testing of Marine Current Turbine's SeaGen 1.2MW Tidal Stream Turbine. *3rd International Conference on Ocean Energy*, pages 1–7, 2010.

[10] Marine Energy News, 2010. URL https://marineenergy.biz/{#}newsitem-15959.

[11] World-leading tidal energy system achieves 5GWh milestone, 2012. URL http://www.siemens.co.uk/en/news{_}press/index/news{_}archive/seagen-achieves-5gw-tidal-power-generation-milestone.htm.

[12] Voith turbine lands at Cherbourg - Wave and Tidal - Renewable Energy News, 2013. URL http://renews.biz/39962/voith-turbine-lands-at-cherbourg/.

[13] Sabella Preparing for D10 Tidal Turbine Deployment, 2015. URL https://www.offshorewind.biz/2015/06/19/sabella-preparing-for-d10-tidal-turbine-deployment/.

[14] Alstom Shows Tidal Stream Power Generation - Subsea World News, 2013. URL https://subseaworldnews.com/2013/04/18/alstom-shows-tidal-stream-power-generation-video/.

[15] L. Chen and W. H. Lam. A review of survivability and remedial actions of tidal current turbines. *Renewable and Sustainable Energy Reviews*, 43:891–900, 2014. ISSN 13640321. doi: 10.1016/j.rser.2014.11.071. URL http://dx.doi.org/10.1016/j.rser.2014.11.071.

[16] L. Chen and W. H. Lam. Methods for predicting seabed scour around marine current turbine. *Renewable and Sustainable Energy Reviews*, 29:683–692, 2014. ISSN 13640321. doi: 10.1016/j.rser.2013.08.105. URL http://dx.doi.org/10.1016/j.rser.2013.08.105.

[17] R. Noruzi, M. Vahidzadeh, and A. Riasi. Design, analysis and predicting hydrokinetic performance of a horizontal marine current axial turbine by consideration of turbine installation depth. *Ocean Engineering*, 108:789–798, 2015. ISSN 00298018. doi: 10.1016/j.oceaneng.2015.08.056. URL http://dx.doi.org/10.1016/j.oceaneng.2015.08.056.

[18] L. Chernin and D. V. Val. Probabilistic prediction of cavitation on rotor blades of tidal stream turbines. *Renewable Energy*, 113:688–696, 2017. ISSN 18790682. doi: 10.1016/j.renene.2017.06.037. URL http://dx.doi.org/10.1016/j.renene.2017.06.037.

[19] A. S. Bahaj, A. F. Molland, J. R. Chaplin, and W. M. J. Batten. Power and thrust measurements of marine current turbines under various hydrodynamic flow conditions in a cavitation tunnel and a towing tank. *Renewable Energy*, 32(3):407–426, 2007. ISSN 09601481. doi: 10.1016/j.renene.2006.01.012.

[20] J. Machado, J. Baltazar, and J. Falcão de Campos. Hydrodynamic Design and Analysis of Horizontal Axis Marine Current Turbines With Lifting Line and Panel Methods. In *OMAE*, page 13, 2011.

[21] J. N. Goundar and M. R. Ahmed. Design of a horizontal axis tidal current turbine. *Applied Energy*, 111:161–174, 2013. ISSN 03062619. doi: 10.1016/j.apenergy.2013.04.064. URL http://dx.doi.org/10.1016/j.apenergy.2013.04.064.

[22] G. de Oliveira. *Wind Turbine Airfoils with Boundary Layer Suction - A Novel Design Approach*. MSc thesis, Delft University of Technology, Delft, the Netherlands, 2011.

[23] H. Ouyang, L. Weber, and A. J. Odgaard. Design optimization of a two-dimensional hydrofoil by applying a genetic algorithm. *Engineering Optimization*, 38(5):529–540, 2006. ISSN 0305215X. doi: 10.1080/03052150600574317.

[24] M. R. Head. Entrainment in the Turbulent Boundary Layer. Technical report, London, 1958.

[25] J. N. Goundar, M. R. Ahmed, and Y. H. Lee. Numerical and experimental studies on hydrofoils for marine current turbines. *Renewable Energy*, 42:173–179, 2011. ISSN 09601481. doi: 10.1016/j.renene.2011.07.048.

[26] W. M. Batten, A. S. Bahaj, A. F. Molland, and J. R. Chaplin. Hydrodynamics of marine current turbines. *Renewable Energy*, 31(2):249–256, 2006. ISSN 09601481. doi: 10.1016/j.renene.2005.08.020.

[27] A. S. Bahaj, W. M. Batten, and G. McCann. Experimental verifications of numerical predictions for the hydrodynamic performance of horizontal axis marine current turbines. *Renewable Energy*, 32 (15):2479–2490, 2007. ISSN 09601481. doi: 10.1016/j.renene.2007.10.001.

[28] X. Q. Luo, G. J. Zhu, and J. J. Feng. Multi-point design optimization of hydrofoil for marine current turbine. *Journal of Hydrodynamics*, 26(5):807–817, 2014. ISSN 10016058. doi: 10.1016/S1001-6058(14)60089-5. URL http://dx.doi.org/10.1016/S1001-6058(14)60089-5.

[29] K. V. Kostas, A. I. Ginnis, C. G. Politis, and P. D. Kaklis. Shape-optimization of 2D hydrofoils using an Isogeometric BEM solver. *CAD Computer Aided Design*, 82:79–87, 2017. ISSN 00104485. doi: 10.1016/j.cad.2016.07.002. URL http://dx.doi.org/10.1016/j.cad.2016.07.002.

[30] M. Sacher, M. Durand, É. Berrini, F. Hauville, R. Duvigneau, O. Le Maître, and J. A. Astolfi. Flexible hydrofoil optimization for the 35th America's Cup with constrained EGO method. *Ocean Engineering*, 157(September 2017):62–72, 2018. ISSN 00298018. doi: 10.1016/j.oceaneng.2018.03.047.

[31] B. Wu, X. Zhang, J. Chen, M. Xu, S. Li, and G. Li. Design of high-efficient and universally applicable blades of tidal stream turbine. *Energy*, 60:187–194, 2013. ISSN 03605442. doi: 10.1016/j.energy.2013.07.061. URL http://dx.doi.org/10.1016/j.energy.2013.07.061.

[32] W. M. J. Batten, A. S. Bahaj, A. F. Molland, and J. R. Chaplin. The prediction of the hydrodynamic performance of marine current turbines. *Renewable Energy*, 33(5):1085–1096, 2008. ISSN 09601481. doi: 10.1016/j.renene.2007.05.043.

[33] W. M. Batten, A. S. Bahaj, A. F. Molland, and J. R. Chaplin. Experimentally validated numerical method for the hydrodynamic design of horizontal axis tidal turbines. *Ocean Engineering*, 34(7):1013–1020, 2007. ISSN 00298018. doi: 10.1016/j.oceaneng.2006.04.008.

[34] P. A. S. F. D. Silva, L. D. Shinomiya, T. F. D. Oliveira, J. R. P. Vaz, A. L. A. Mesquita, and A. C. P. B. Junior. Design of Hydrokinetic Turbine Blades Considering Cavitation. *Energy Procedia*, 75:277–282, 2015. ISSN 18766102. doi: 10.1016/j.egypro.2015.07.343. URL http://dx.doi.org/10.1016/j.egypro.2015.07.343.

[35] N. Garg, G. K. Kenway, J. R. Martins, and Y. L. Young. High-fidelity multipoint hydrostructural optimization of a 3-D hydrofoil. *Journal of Fluids and Structures*, 71(2017):15–39, 2017. ISSN 10958622. doi: 10.1016/j.jfluidstructs.2017.02.001. URL http://dx.doi.org/10.1016/j.jfluidstructs.2017.02.001.

[36] M. Drela. XFOIL: An Analysis and Design System for Low Reynolds Number Aerodynamics. volume 54, 1989. ISBN 978-3-540-51884-6. doi: 10.1007/978-3-642-84010-4. URL http://link.springer.com/10.1007/978-3-642-84010-4.

[37] M. Drela. Implicit Implementation of the Full eˆn Transition Criterion. (June), 2003.

[38] M. Drela and H. Youngren. XFOIL - Subsonic airfoil development system, 2013. URL http://web.mit.edu/drela/Public/web/xfoil/.

[39] J. Falcão de Campos. Hydrodynamic Power Optimization of a Horizontal Axis Marine Current Turbine with Lifting Line Theory. In *ISOPE*, pages 307–313. ISOPE, 2007. ISBN 9781880653685.

[40] A. Betz. Schraubenpropeller mit geringstem Energieverlust. *Göttinger Nachrichten*, (1919): 2018, 1919. URL http://scholar.google.com/scholar?hl=en{&}btnG=Search{&}q=intitle:Schraubenpropeller+mit+geringstem+Energieverlust{#}1.

[41] S. Goldstein. On the Vortex Theory of Screw Propellers. *Proceedings of the Royal Society A: Mathematical, Physical and Engineering Sciences*, 123(792):440–465, 1929. ISSN 1364-5021. doi: 10.1098/rspa.1929.0078. URL http://rspa.royalsocietypublishing.org/cgi/doi/10.1098/rspa.1929.0078.

[42] H. W. Lerbs. Moderately Loaded Propellers with a Finite Number of Blades and an Arbitrary Distribution of Circulation. *Transactions of the Society of Naval Architects and Marine Engineer*, 60 (1952):73–123, 1952.

[43] W. B. Morgan and J. W. Wrench. Some computational aspects of propeller design. *Methods in Computational Physics*, 4:301–331, 1965.

[44] J. E. Kerwin, W. B. Coney, and C. Hsin. Optimum Circulation Distributions for Single and Multicomponent Propulsors. In *American Towing Tank Conference, 21st*, Washington DC, USA, 1986.

[45] J. Baltazar and J. Falcão de Campos. Hydrodynamic Analysis of a Horizontal Axis Marine Current Turbine With a Boundary Element Method. *Journal of Offshore Mechanics and Arctic Engineering*, 133(4):041304, 2011. ISSN 08927219. doi: 10.1115/1.4003387. URL http://offshoremechanics.asmedigitalcollection.asme.org/article.aspx?articleid=1457593.

[46] R. Balbino Dos Santos Pereira, G. D. Oliveira, W. A. Timmer, and E. Quaeghebeur. Probabilistic Design of Airfoils for Horizontal Axis Wind Turbines. page 10, 2018.

[47] W. D. Grant. THE CONTINENTAL-SHELF BOTTOM BOUNDARY LAYER. pages 265–305, 1986.

[48] A. D. Heathershaw and D. N. Langhorne. Observations of Near-bed Velocity Profiles and Seabed Roughness in Tidal Currents Flowing over Sandy Gravels. pages 459–482, 1988.

[49] X. Ke, M. B. Collins, and S. E. Poulos. Coastal ISummer Velocity Structure and Sea Bed Roughness. 10(3):702–715, 2014.

[50] B. M. Kulfan. A Universal Parametric Geometry Representation Method-"CST". In *45th AIAA Aerospace Sciences Meeting and Exhibit*, pages 1–36, 2007.

[51] R. Balbino Dos Santos Pereira. *Active Stall Control of Horizontal Axis Wind Turbines - A dedicated study with emphasis on DBD plasma actuators*. PhD thesis, Delft University of Technology, 2017.

[52] R. Balbino dos Santos Pereira, W. Timmer, G. de Oliveira, and G. van Bussel. A simple atmospheric boundary layer model applied to large eddy simulations of wind turbine wakes. *Wind Energy*, 17 (April 2013):657–669, 2014. ISSN 1099-1824. doi: 10.1002/we. URL `http://onlinelibrary.wiley.com/doi/10.1002/we.1608/full`.

[53] A. F. Molland, A. S. Bahaj, J. R. Chaplin, and W. M. Batten. Measurements and predictions of forces, pressures and cavitation on 2-D sections suitable for marine current turbines. *Proceedings of the Institution of Mechanical Engineers Part M: Journal of Engineering for the Maritime Environment*, 218(2):127–138, 2004. ISSN 14750902. doi: 10.1243/1475090041651412.

[54] G. De Oliveira, R. Pereira, N. Timmer, and R. Van Rooij. Improved airfoil polar predictions with data-driven boundary-layer closure relations. *Journal of Physics: Conference Series*, 1037(2), 2018. ISSN 17426596. doi: 10.1088/1742-6596/1037/2/022009.

[55] R. Abadia. *Estudo de Perfis*. MSc thesis, Instituto Superior Técnico, 2007.

[56] R. P. J. O. M. van Rooij and W. A. Timmer. Roughness Sensitivity Considerations for Thick Rotor Blade Airfoils. *ASME 2003 Wind Energy Symposium*, 125(November):22–31, 2003. ISSN 01996231. doi: 10.1115/WIND2003-350. URL `http://proceedings.asmedigitalcollection.asme.org/proceeding.aspx?articleid=1598545`.

[57] P. Liu and B. Veitch. Design and optimization for strength and integrity of tidal turbine rotor blades. *Energy*, 46(1):393–404, 2012. ISSN 03605442. doi: 10.1016/j.energy.2012.08.011. URL `http://dx.doi.org/10.1016/j.energy.2012.08.011`.

[58] W. A. Timmer and R. P. J. O. M. van Rooij. Summary of the Delft University Wind Turbine Dedicated Airfoils. *Journal of Solar Energy Engineering*, 125(4):488, 2003. ISSN 01996231. doi: 10.1115/1.1626129. URL `http://solarenergyengineering.asmedigitalcollection.asme.org/article.aspx?articleid=1456892`.

Appendix A

Reference Turbine

A.1 NACA 63-8XX XFOIL data

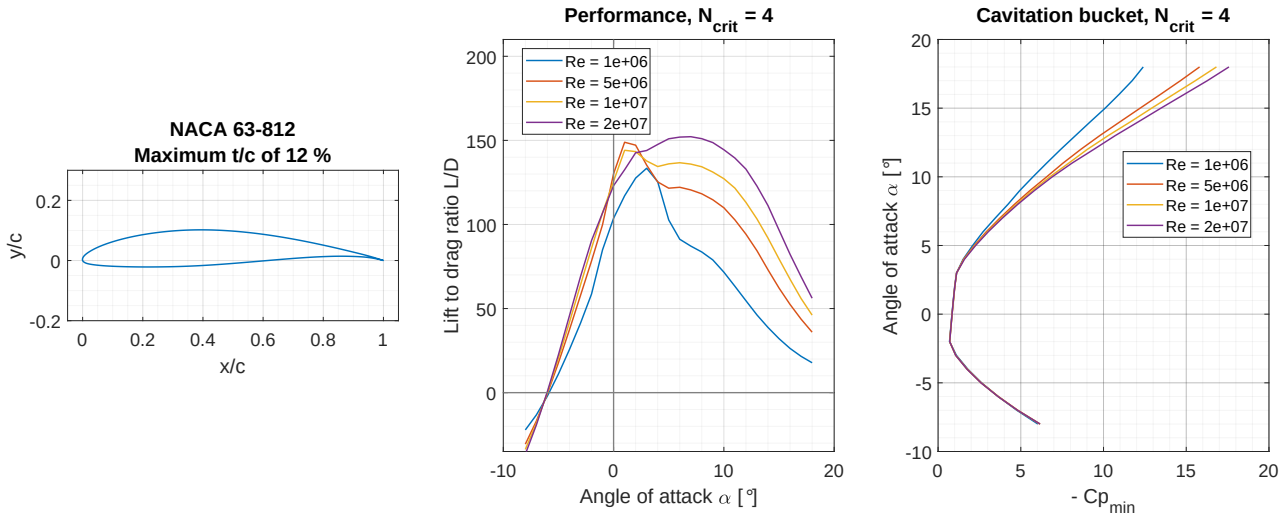

(a) NACA 63-812 foil, performance and cavitation bucket

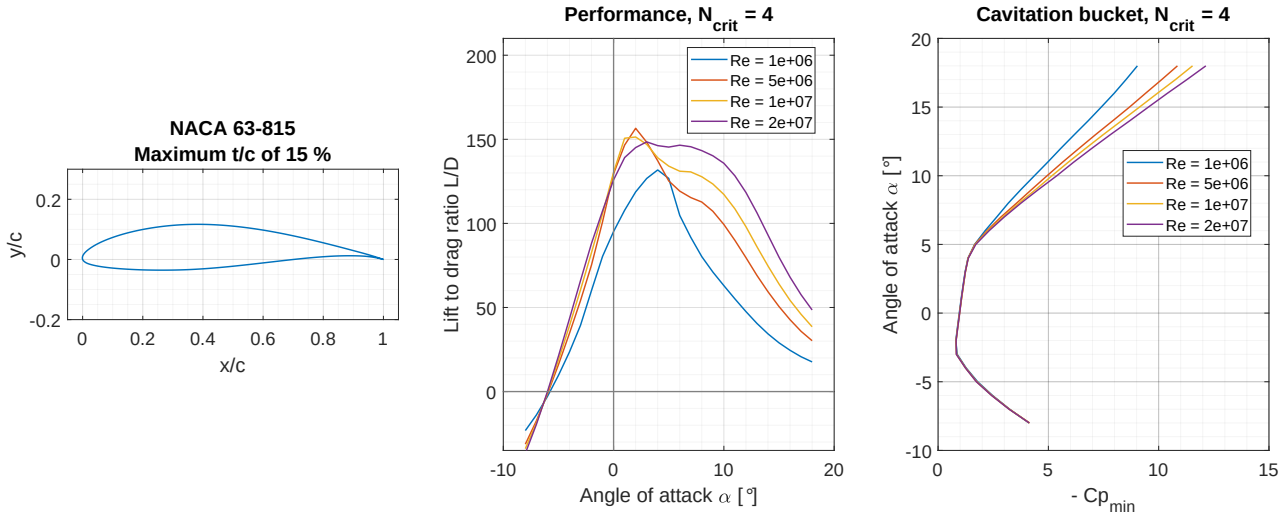

(b) NACA 63-815 foil, performance and cavitation bucket

Figure A.1: Sections composing the blades of reference turbine (data retrieved from software XFOIL)

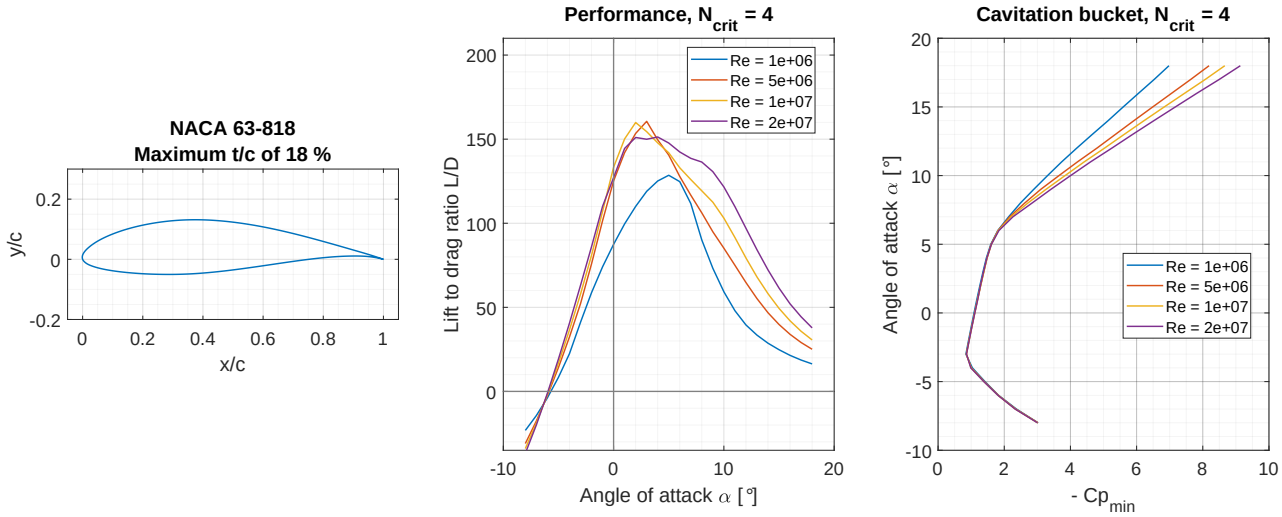

(a) NACA 63-818 foil, performance and cavitation bucket

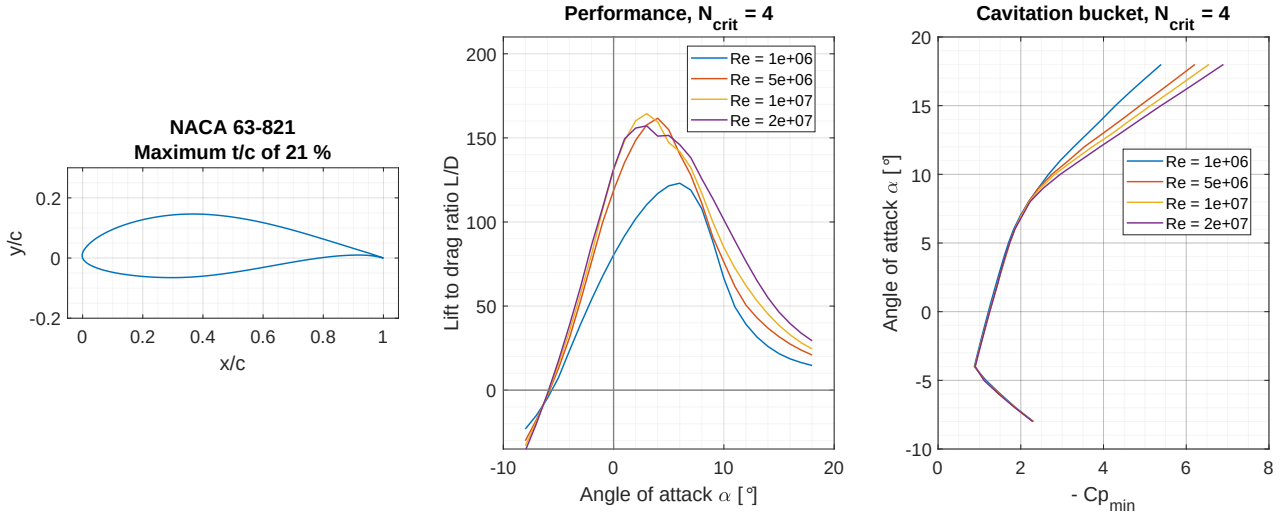

(b) NACA 63-821 foil, performance and cavitation bucket

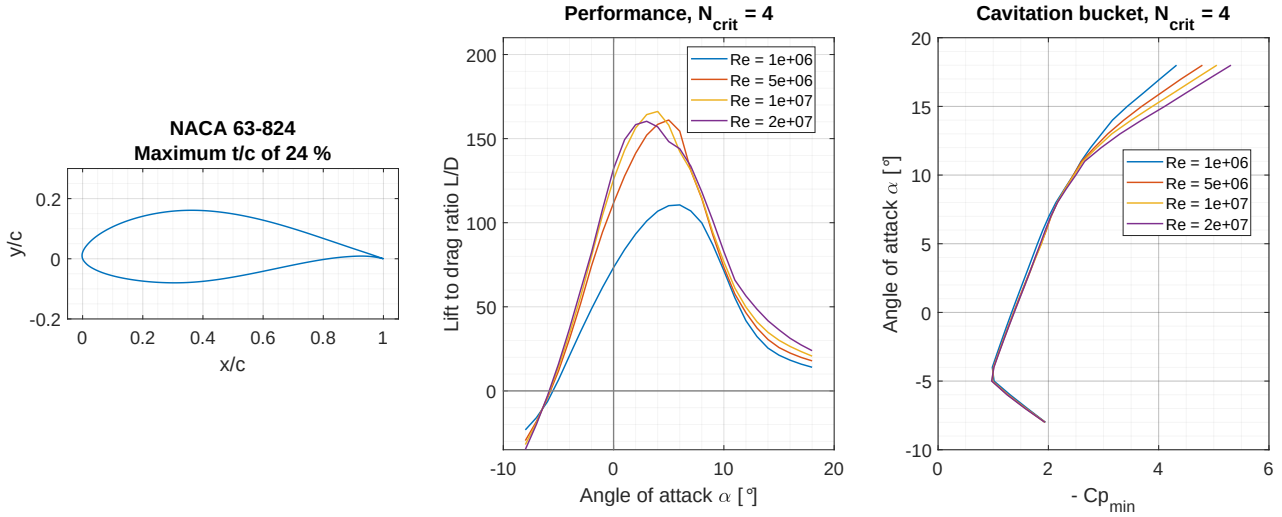

(c) NACA 63-824 foil, performance and cavitation bucket

Figure A.2: Sections composing the blades of reference turbine (data retrieved from software XFOIL)

A.2 Reference turbine geometry

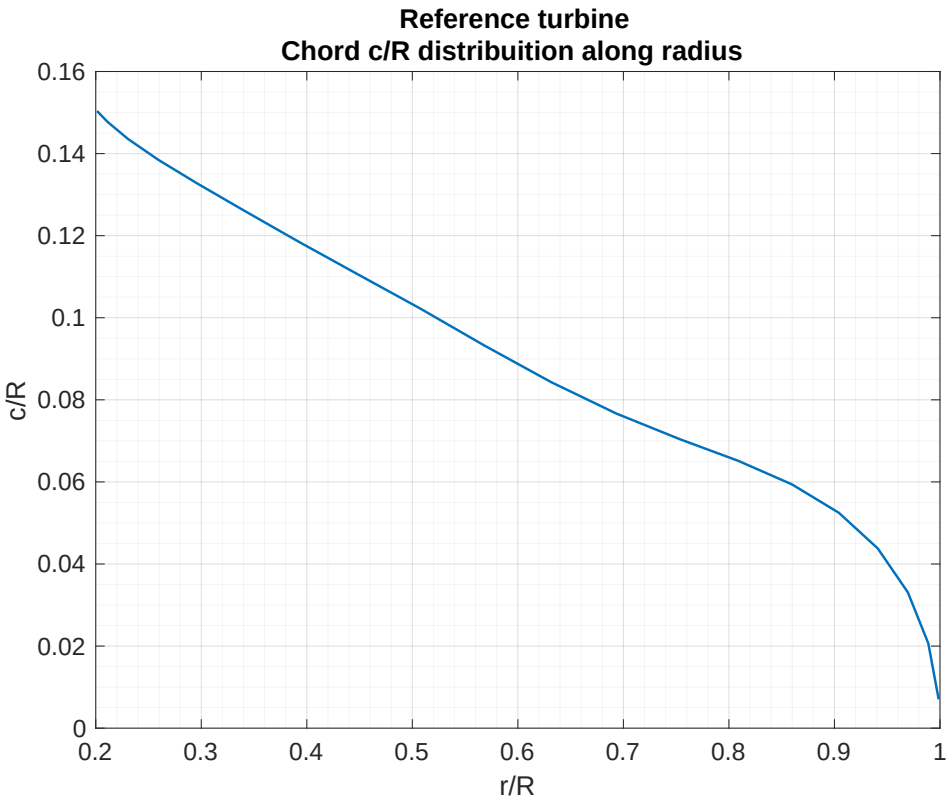

Figure A.3: Reference turbine blades chord distribution

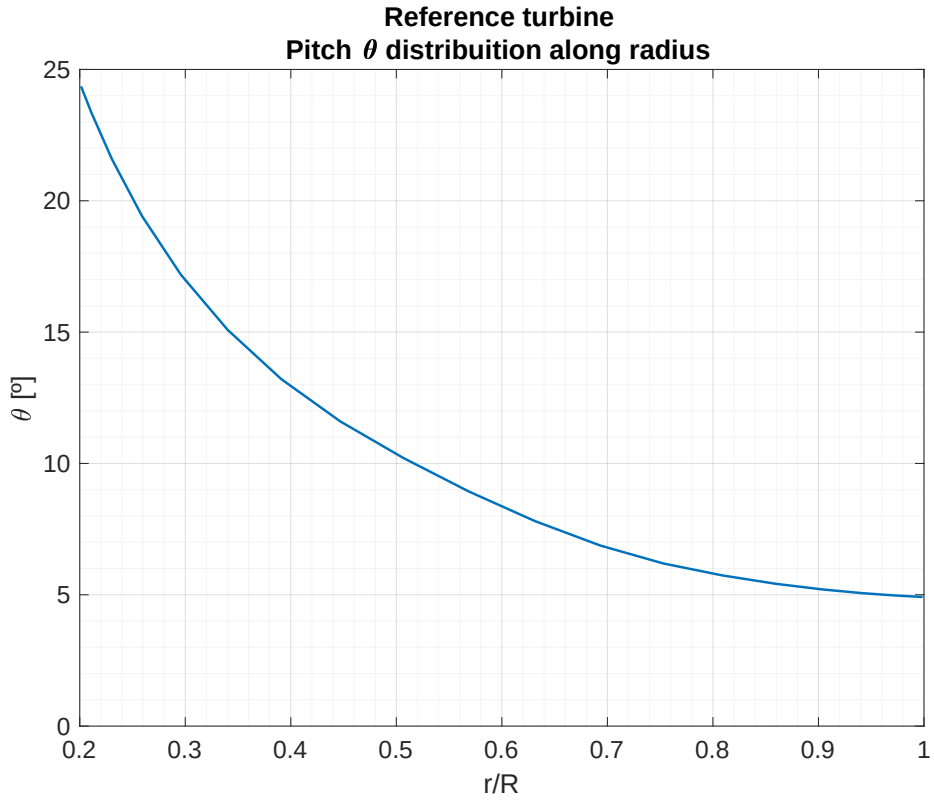

Figure A.4: Reference turbine blades pitch distribution

A.3 Reference turbine operation characteristics

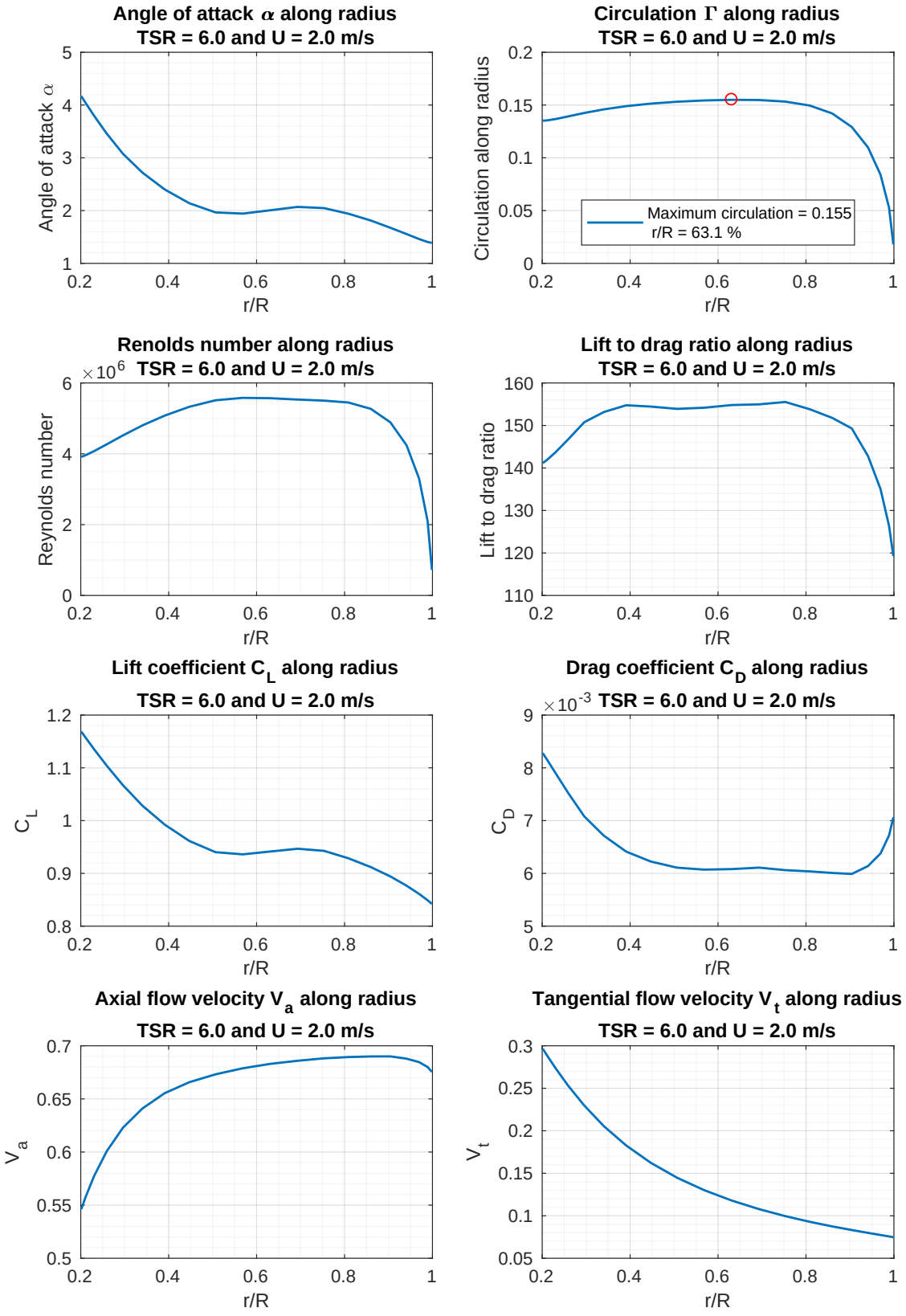

Figure A.5: Reference turbine characteristics at TSR = 6 and U = 2 m/s

A.4 Reference turbine performance

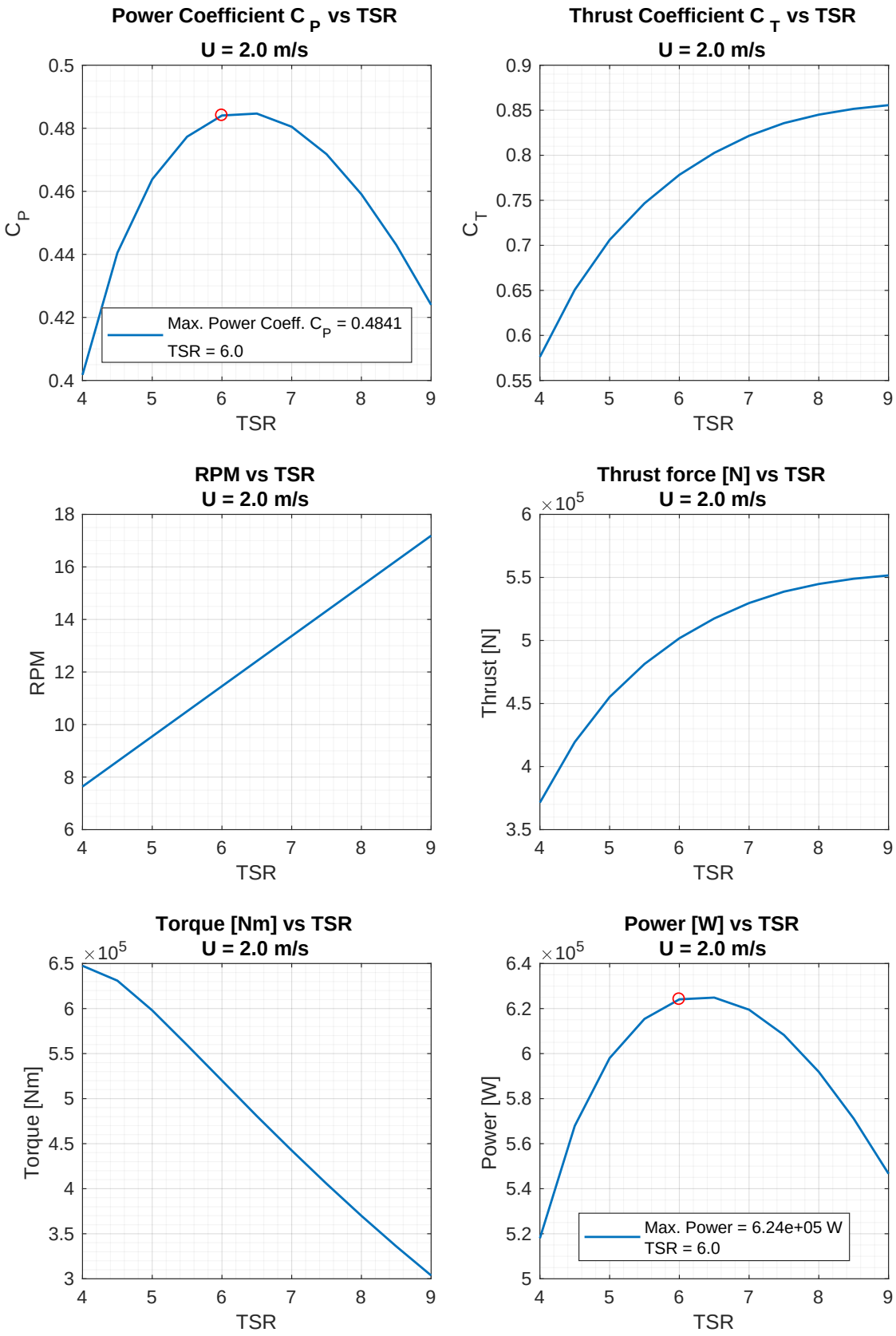

Figure A.6: Reference turbine performance data at U = 2 m/s

Appendix B

Redesigned turbine

B.1 Optimized hydrofoils IST-MT1-XX XFOIL data

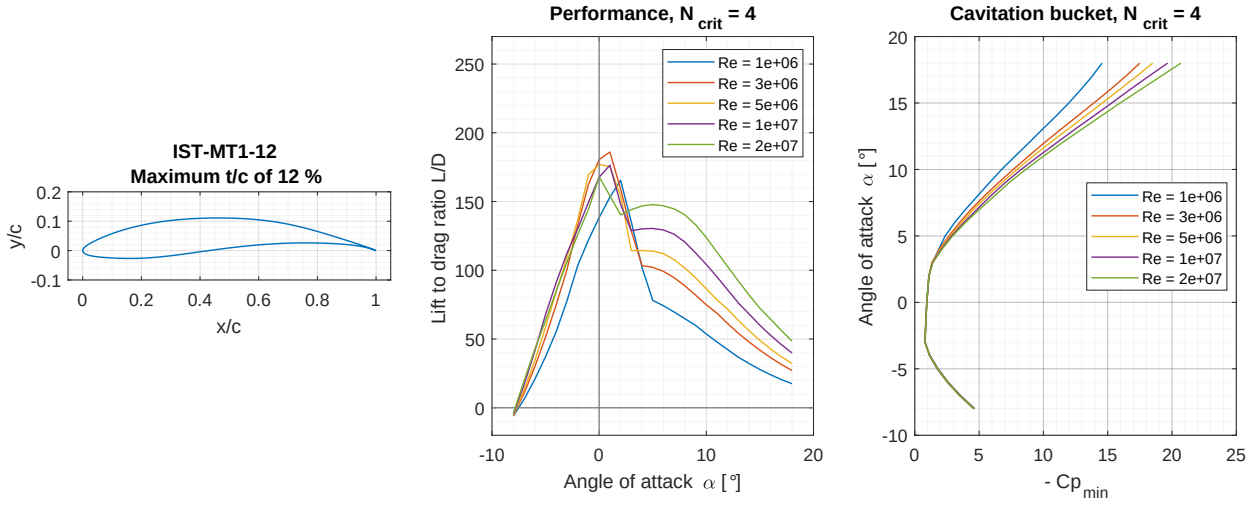

(a) IST-MT-12 hydrofoil, performance and cavitation bucket

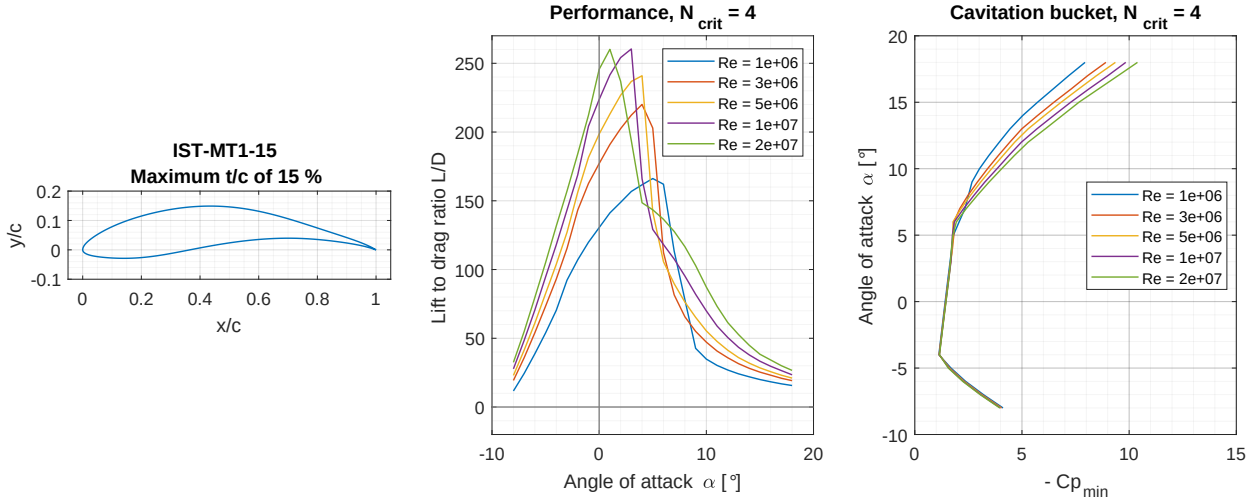

(b) IST-MT-15 hydrofoil, performance and cavitation bucket

Figure B.1: Sections composing the blades of the redesigned turbine
(data retrieved from software XFOIL)

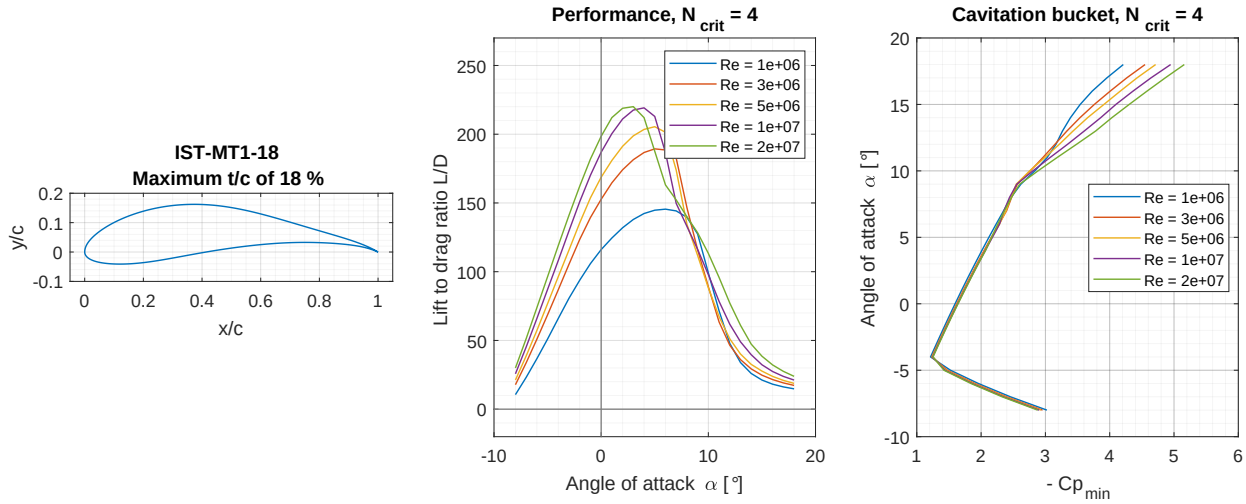

(a) IST-MT-18 hydrofoil, performance and cavitation bucket

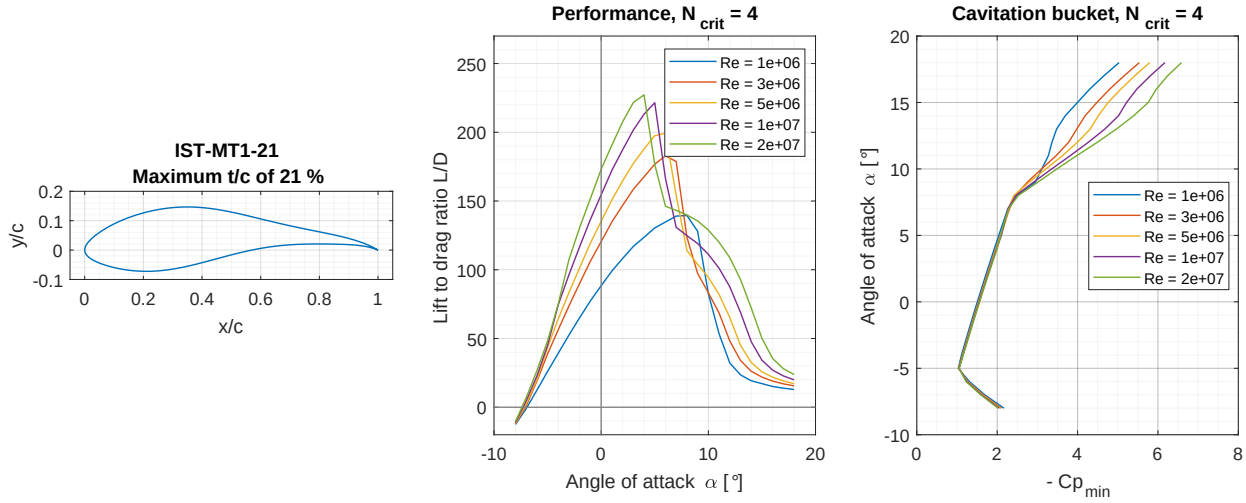

(b) IST-MT-21 hydrofoil, performance and cavitation bucket

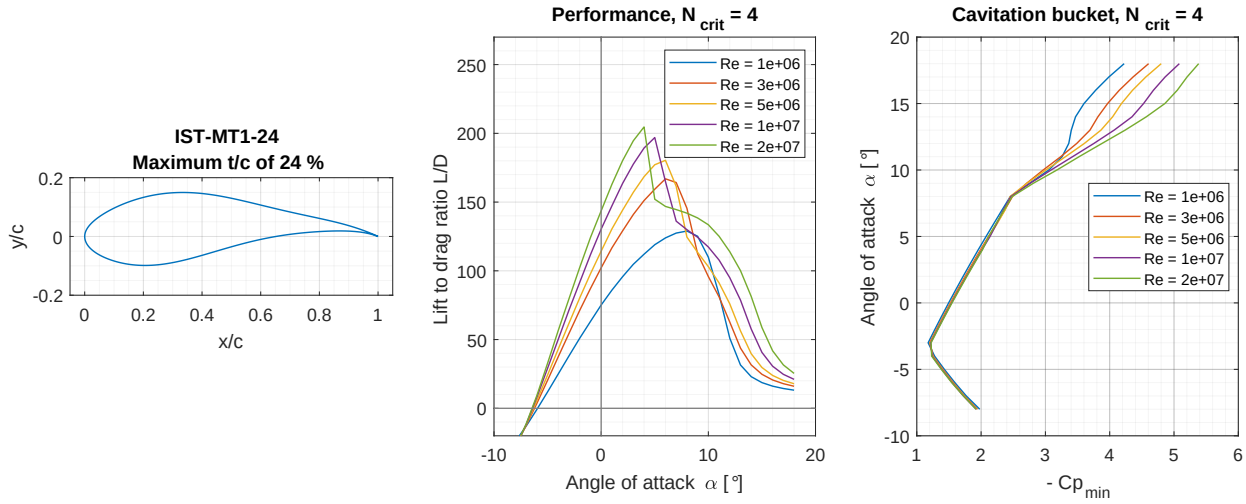

(c) IST-MT-24 hydrofoil, performance and cavitation bucket

Figure B.2: Sections composing the blades of the redesigned turbine
(data retrieved from software XFOIL)

B.2 Bernstein coefficients of hydrofoils IST-MT1-XX

Table B.1: Berstein coefficients for hydrofoil IST-MT1-12

IST-MT1-12								
Upper	0.137	0.2645	0.2411	0.3546	0.1878	0.5669	0.2423	0.4151
Lower	0.1264	0.009127	0.2339	-0.222	0.1747	-0.3136	0.03398	-0.408
Trailing Edge	0.0001							

Table B.2: Berstein coefficients for hydrofoil IST-MT1-15

IST-MT1-15								
Upper	0.2003	0.3581	0.2799	0.505	0.357	0.5721	0.2148	0.5782
Lower	0.1341	0.02235	0.2565	-0.3236	0.1911	-0.4328	-0.0297	-0.3938
Trailing Edge	0.0003							

Table B.3: Berstein coefficients for hydrofoil IST-MT1-18

IST-MT1-18								
Upper	0.2956	0.4033	0.3932	0.4846	0.4341	0.4126	0.2763	0.5803
Lower	0.1981	0.07704	0.1975	-0.241	0.201	-0.386	0.0298	-0.4849
Trailing Edge	0.0003							

Table B.4: Berstein coefficients for hydrofoil IST-MT1-21

IST-MT1-21								
Upper	0.2324	0.4115	0.2729	0.6241	0.186	0.349	0.2376	0.5819
Lower	0.211	0.1847	0.308	0.03406	0.07502	-0.3043	0.1288	-0.4376
Trailing Edge	0.0002							

Table B.5: Berstein coefficients for hydrofoil IST-MT1-24

IST-MT1-24								
Upper	0.2925	0.3653	0.4172	0.4329	0.3683	0.2065	0.3682	0.4476
Lower	0.3005	0.2752	0.3639	0.08388	0.08296	-0.1379	0.04412	-0.4089
Trailing Edge	0.0003							

B.3 Redesigned turbine geometry

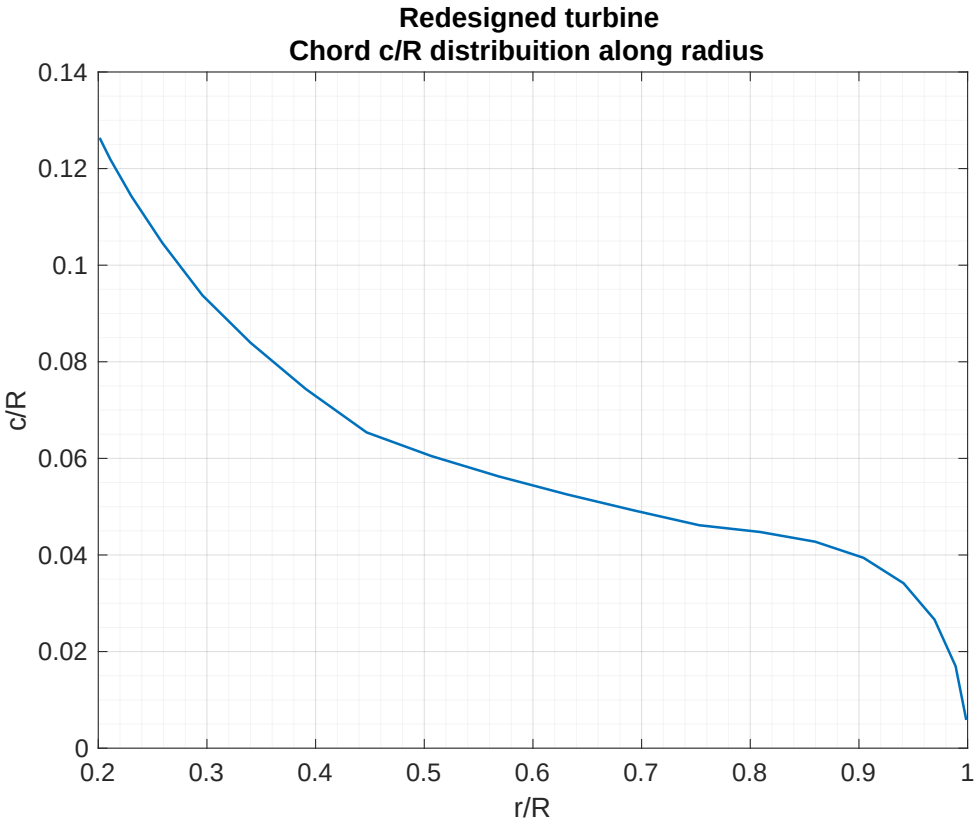

Figure B.3: Redesigned turbine blades chord distribution

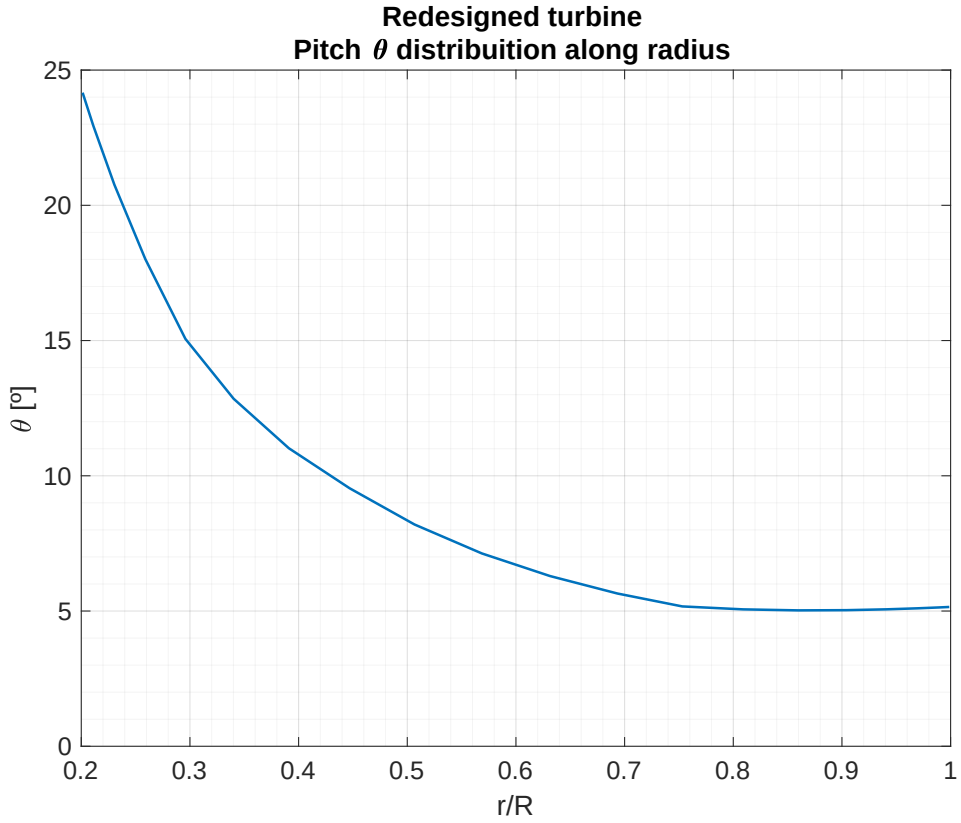

Figure B.4: Redesigned turbine blades pitch distribution

B.4 Redesigned turbine operation characteristics

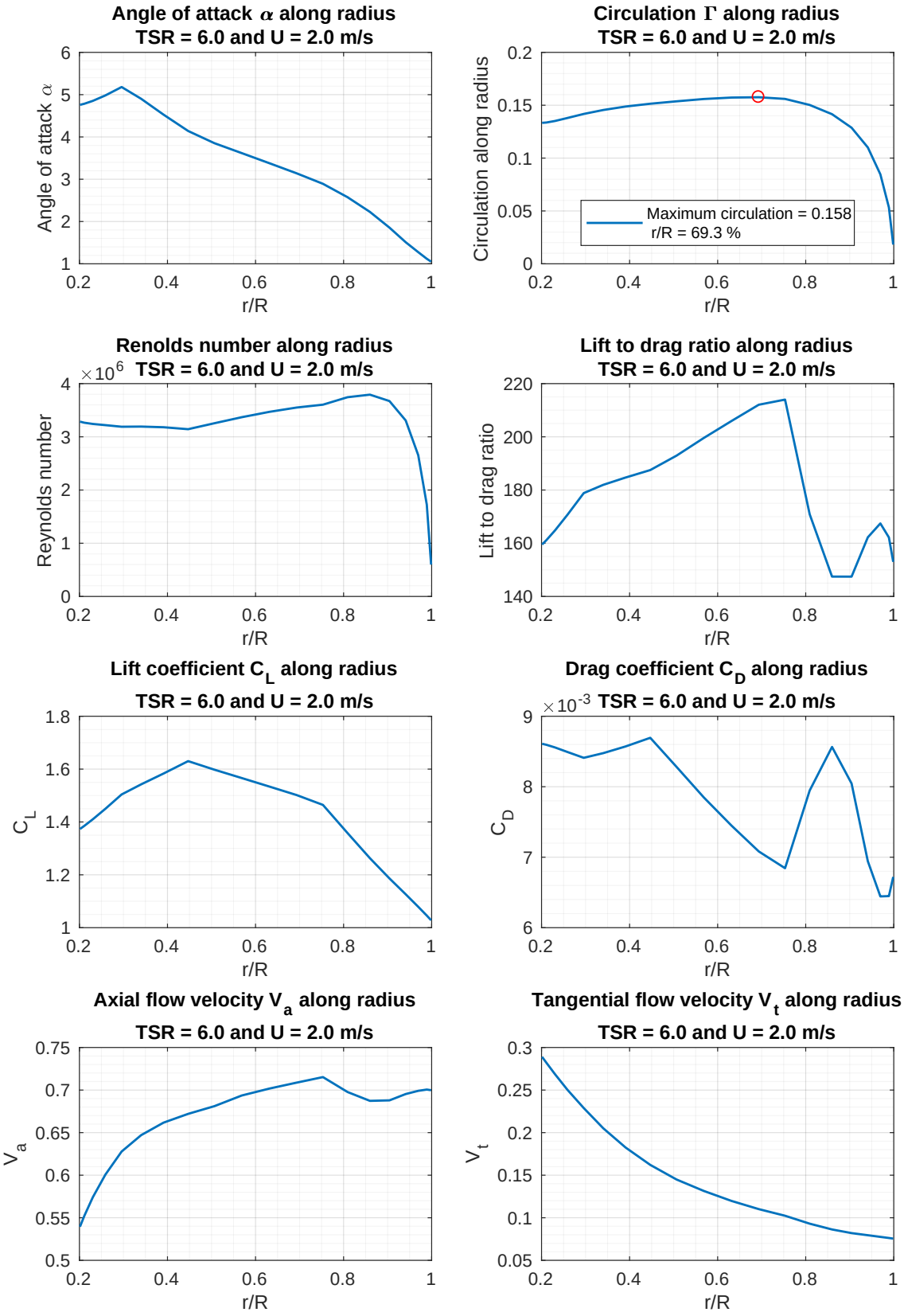

Figure B.5: Redesigned turbine characteristics at TSR = 6 and U = 2 m/s

B.5 Redesigned turbine performance

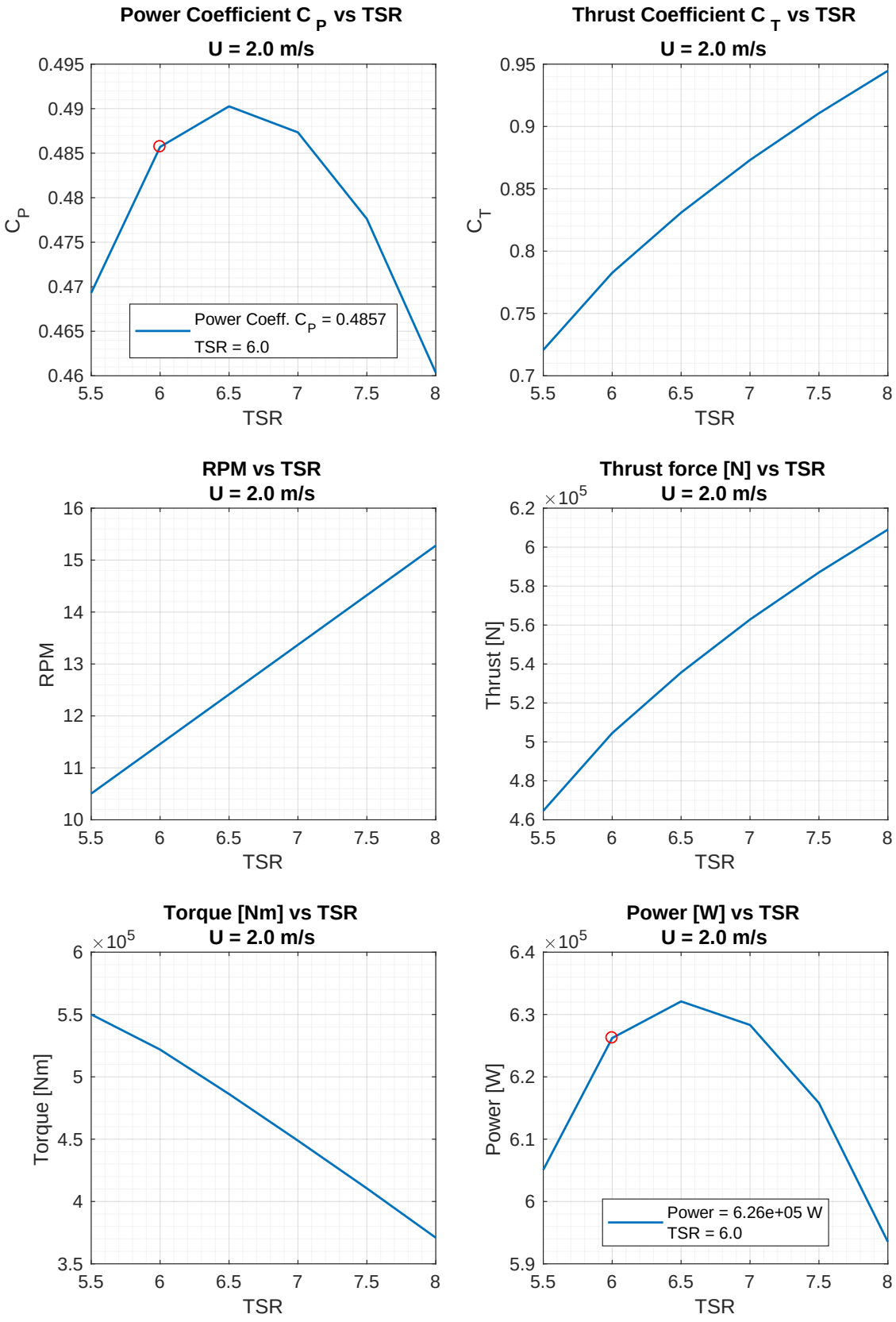

Figure B.6: Redesigned turbine performance data at U = 2 m/s